Electrostatic Modulation of Biological Systems: From Cells to Molecules

by

Yuan Wang

A Dissertation Presented in Partial Fulfillment
of the Requirements for the Degree
Doctor of Philosophy

Approved January 2021 by the
Graduate Supervisory Committee:

Quan Qing, Chair
Stuart Lindsay
Shaopeng Wang
Robert Ros

ARIZONA STATE UNIVERSITY

May 2021

ABSTRACT

My research focuses on studying the interaction between spatiotemporally encoded electric field (EF) and living cells and biomolecules. In this thesis, I report two projects that I have been working on to address these questions.

My first project studies the EF modulation of the extracellular-signal-regulated kinase (ERK) pathway. I demonstrated modulation of ERK activities using alternative current (AC) EFs in a new frequency range applied through high-k dielectric passivated microelectrodes with single-cell resolution without electrochemical process induced by the EF stimulation. Further experiments pinpointed a mechanism of phosphorylation site of epidermal growth factor (EGF) receptor to activate the EGFR-ERK pathway that is independent of EGF. AC EFs provide a new strategy to precisely control the dynamics of ERK activation, which may serve as a powerful platform for control of cell behaviors with implications in wide range of biomedical applications.

In the second project, I used solid-state nanopore system as the base platform for single molecule experiments, and developed a scalable bottom-up process to construct planar nanopore devices with self-aligned transverse tunneling junctions, all embedded on a nanofluidic chip, based on feedback-controlled reversible electrochemical deposition in a confined nanoscale space. I demonstrated the first simultaneous detection of translocating DNA molecules from both the ionic channel and the tunneling junction with very high yield. Meanwhile, the signal amplitudes from the tunneling junction are unexpectedly high, indicating that these signals are probably dominated by transient currents associated with the fast motion of charged molecules between the transverse

electrodes. This new platform provides the flexibility and reproducibility required to study quantum-tunneling-based DNA detection and sequencing.

In summary, I have developed two platforms that engineer heterogenous EF at different length scales to modulate live cells and single biomolecules. My results suggest that the charges and dipoles of biomolecules can be electrostatically manipulated to regulate physiological responses and to push detection resolution to single molecule level. Nevertheless, there are still many interesting questions remain, such as the molecular mechanism of EF-protein interaction and tunneling signal extraction. These will be the topics for future investigations.

ACKNOWLEDGEMENTS

I would like to thank my advisor, Dr. Quan Qing, for his support during my graduate period. His resources, guidance, and advice have been helpful and necessary for me to complete my projects. I have learned much from his insight into related research topics and his way of learning new skills when solving unexpected issues. Moreover, I would like to thank Dr. Stuart Lindsay and Dr. Shaopeng Wang for their insightful advice and comments on the nanopore and related projects. I would also like to thank Dr. Robert Ros for his support and teachings in biological physics courses.

My thanks also go to my colleagues for their help and collaborations during my graduate period: Mike Darrow, Ching-wei Tsao, Houpu Li, Minxi Hu, and Sanjana Mukherjee from Dr. Qing's group, and Weisi Song, Bintian Zhang, and Joshua Sadar from Dr. Lindsay's group. Special thanks to Dr. Min Zhao, Dr. Liang Guo, and Dr. John Albeck from the University of California, Davis, and Dr. Zhou Li from the Nanjing University of Aeronautics and Astronautics.

In addition, I would like to thank my family for their understanding and support for my graduate period far away from my homeland.

Finally, I gratefully acknowledge the funding support from the National Institutes of Health and the Air Force Office of Scientific Research.

TABLE OF CONTENTS

Page

LIST OF TABLES

Table Page

LIST OF FIGURES

Figure Page

Figure Page

Figure Page

CHAPTER 1. INTRODUCTION

1.1. Discovery of Endogenous Electric Field

Since Luigi Galvani discovered the animal electricity via his famous experiment involving electric stimulation on a frog leg preparation in 1780, electric fields (EFs) have been known to play an important role in biological systems [1]. A frog leg preparation will contract when the cut end of a sciatic nerve is in contact with the frog leg muscle. Following intuitive research [1-3] discovered that endogenous EFs generated in cells can trigger the contraction of muscles in a dead body. Apart from triggering muscle contractions, these endogenous EFs in living biological systems demonstrate further functions related to cellular communication and interactions with neighboring cells and extracellular environments. For example, an action potential [4] occurs when a neuron sends information to other neurons through its axon, and an injury potential [5] occurs when a wound is created on the skin, acting as a guidance cue for cell migration in the subsequent wound healing process. With the development of characterization and measurement techniques, researchers have revealed the fundamental mechanism at a molecular level. The cell membrane is a semipermeable membrane consisting of a lipid bilayer and various membrane proteins. It is now understood that membrane proteins, such as ion channels, pumps, and transporters, will maintain an ion segregation inside and outside the cellular membrane, thereby creating a membrane potential. Changes in the intracellular or extracellular environment would trigger activities of membrane proteins, resulting in endogenous EF signals and eventually leading to single cell or tissue level responses. Thus, whether it is possible to mimic endogenous EF signals and modulate

biological systems according to human need has been an attractive area of investigation in recent decades (Figure 1.1.1).

Biological molecules having their specific conformational structures involving charge distribution and dipoles. Thus, I am interested in the following two aspects of EF modulation. First, modulation of cellular signaling pathways with external EF stimulations. Second, high-resolution detection of biological molecules with engineered EF profiles.

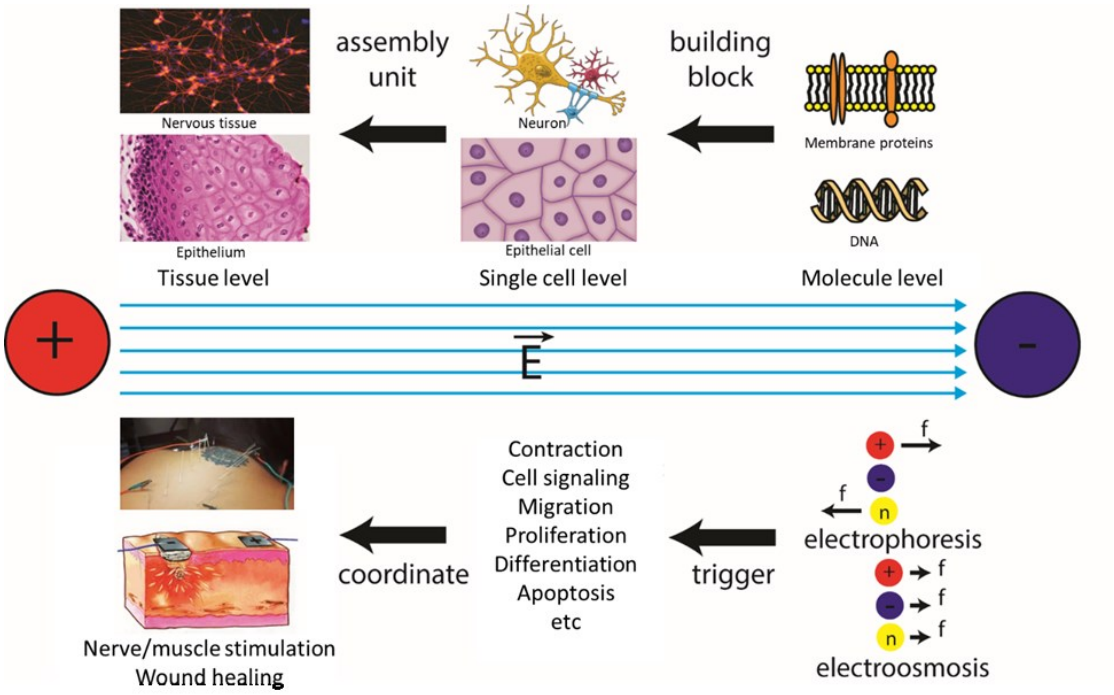

Figure 1.1.1. A schematic of electric field (EF) stimulation applied at different levels of biological systems and their responses. The human body is a complicated system made up of basic biomolecules. Single cells consist of DNA, proteins, and other biomolecules. Cells assembling under certain arrangements form different functioning tissues and organs, which would eventually build up the organ systems and human body. An external EF would affect these different levels of biological systems, as illustrated in the bottom panel. At a molecular level, charged and neutral molecules in cells will be driven under external EFs

and liquid motion induced by external EFs; these two processes are called electrophoresis and electro-osmosis, respectively. The shift or deform of biomolecules under external EFs would trigger cellular activities (such as migration, proliferation, differentiation, and apoptosis). As long as a sufficient number of cells respond to external EFs, the cellular activities will coordinate and exhibit tissue-level phenomena. Nerve or muscle stimulation and tissue regeneration under external EFs are well-studied clinical applications, whereas the fundamental mechanism of how biological molecules in cells interact with external EFs is not clear yet.

1.2. Modulation of Cellular Responses via External EFs

Apart from investigations into endogenous EFs and their biological functions, the way in which exogenous EFs can interact with biological systems at different levels has also been extensively studied. Immediately after the discovery of endogenous EFs, premature attempts were made to treat diseases or disabilities using exogenous EFs. For example, Alessandro Volta, the inventor of the electric battery and a rival of Galvani, tried to treat deafness therapeutically via batteries although no solid scientific evidence of such electric therapy existed. The static electricity generator was also considered to be a medical treatment device. People believed that it would be helpful in treating insomnia, migraines, and baldness by generating a negative electric charge bath and that it was also beneficial for kidney disease if the machine reversed the charge polarity [1]. Those early medical applications of EFs reveals the chaotic situation of electric modulations on living systems due to the lack of solid investigations into the underlying mechanism.

Based on research in past decades, the mechanism of endogenous EFs and their effects on living systems has been revealed. As mentioned earlier, membrane proteins embedded in the cell membrane are biomolecules that respond to environmental chemical, mechanical and electrical signals. In general, there are five types of membrane

proteins: transport proteins, enzymes, receptors, recognition proteins, and joining proteins. Among them, ion channels are pore-forming transport proteins that control ion flows across the cell membrane depending on environmental signals, such as voltage, ligand, lipid and second messengers, and these proteins are important for maintaining membrane potential, creating endogenous EFs in biological systems. Meanwhile, the changes of ion flows in cells would trigger downstream signaling pathways and lead to cellular responses. Therefore, it is possible to modulate cells by controlling the membrane proteins via external EFs.

Overall two distinct categories of cells exist: electrogenic cells, in which voltage-sensitive ion channels govern the response at a time scale from microseconds to seconds, and non-electrogenic cells, in which few of those channels are expressed. It is known that exogenous EFs with different frequencies would yield distinct results at much longer time scales. The Goldman-Hodgkin-Katz voltage equation has been successfully used to explain the response from electrogenic cells as the voltage-sensitive ion channels are triggered by external EFs. For non-electrogenic cells, many biophysical and biochemical processes related to external EFs—from molecular to cellular scales—would have to participate in causing cellular and tissue responses. Based on such initial understandings of interactions between EFs and cells, regenerations of the nervous system, muscles, and the skin with direct current (DC) EF stimulations [5-9] have been reported in the past decades, highlighting the possibility of therapeutic electric treatments. It has also been demonstrated that EF application on a cellular level can lead to significant modulations in migration, proliferation, differentiation and apoptosis [10]. Commercial products and their clinical trials using exogenous EFs to enhance tissue regeneration and drug delivery

have recently successfully demonstrated their promising potential in medical treatments and physical therapies [11-14]. However, other than the well-modeled electroporation process, where the membrane integrity is broken under strong exogenous EFs, the fundamental mechanism of interactions between cells and external EFs is not yet clear. Diversified and sometimes contradictory results have been reported, partly due to the complexity in terms of how EFs can couple with cellular signaling pathways. To date, the EF impact on cell signaling pathways is commonly believed to originate from the stimulation of chemical signals in the environment because of heat, electrochemical, and/or ion flux changes associated with the application of external EFs.

To explain the external EF modulation on non-electrogenic cells, membrane proteins becomes the critical link for interactions between external EFs and cells. Numerous moving charges and dipoles are involved in protein conformation changes and biochemical reactions inside a cell. In principle, external EFs can strongly perturb the energy profiles during these processes, potentially resulting in modulations of the dynamics in the cell signaling network. The spatial distribution of external EFs is highly heterogeneous across the cell in a wide range of frequencies, with the highest potential gradient typically found at the cell membrane, which means that the energy from external EFs can be effectively and specifically concentrated in the membrane region, where many critical signaling pathways take place. To date, the question of whether external EFs can be electrostatically tuned to change the dynamics of cell membrane proteins and regulate downstream signaling pathways for physiological consequences, without exogenous chemical signals, remains an interesting but unexplored one. However, the common challenge in existing studies is that the spatial and temporal resolution of

external EF applications are not precisely controlled, because of the way in which external EFs are applied and the methods used to determine the cellular signaling pathway responses. This makes differentiating the actual direct impact of external EFs from its secondary later cellular responses difficult. Therefore, new designs of EF application system and monitoring methods are necessary to track a more accurate time course of the cell response locally in a short response time. In addition, careful protocols and controls must be developed to distinguish and/or exclude chemical interferences induced by the EF from electrostatic interactions.

1.3. Manipulation and Detection of Biomolecules with an Engineered EF Profile

Apart from the cellular modulation via external EFs, electromagnetic fields with engineered geometric distributions have been used to manipulate molecules and atoms recently [15-17]. Since Ashkin *et al.* introduced the idea that the forces of radiation pressure generated in focused laser beams can affect movement of small transparent micron-sized neutral particles, this trapping and manipulation technique is applied on various particles, including atoms, biological molecules, dielectric particle, organelles, and even cells without damage [18]. Similar techniques like electric tweezers [15], magnetic tweezers [19], and acoustic tweezers [20] are invented following the same paradigm. Recent development of digital microfluidics [21] combines controlled electric field and microfluidic system, providing new insights for biochemical analysis and clinical diagnosis without complicate instruments. Based on these understandings, we would like to probe this further and develop a device that can reach an ultimate resolution for molecule manipulation and detection. In this regard, nanopore device for DNA sequencing seems to be a good platform for our investigation.

Known as the critical molecule for biological information storage, deoxyribonucleic acid (DNA) consists of two polynucleotide chains that coil around each other, forming a double helix structure. The sequence of this helix will instruct the protein expression during the development, functioning, growth, and reproduction of cells. Mistakes or damages that occur on the DNA or during DNA replication would malfunction or even impair all living organisms. In this regard, knowing the DNA sequence is an important and interesting topic in biological and medical research. So far, two generations of DNA sequencing techniques exist that are based on a "sequence-by-synthesis" scheme. Sanger's first-generation DNA sequencing technique [22] combined "chain termination" and electrophoresis, providing a slow but accurate DNA sequencing result, and Ronaghi' second-generation DNA sequencing technique [23] based on the real-time signal collection of pyrophosphate allows for a mass parallelization of sequencing reactions, thereby increasing the amount of one sample tested in a single run. As mentioned earlier, both techniques [24-27] are accurate but slow in preparation, and they are not able to achieve single-molecule-level sequencing.

As the newest generation of DNA sequencing technique, nanopore analysis mimics the molecule transportation through protein channels between the intracellular and extracellular environment and distinguishes the molecule structure via the modulation of ionic current (current between *cis*- and *trans*- chambers; Figure 1.3.1). It is similar to the Coulter principle [28] and can be used for molecule detections other than DNA [29]. Recent studies on the detection mechanism based on ionic current reveal that the detection resolution is limited by the nanopore size. To pursuit single-base level detection of DNA sequence, tunneling current-based detection has been an attractive

candidate. Specifically, by embedding a transverse electrode pair close to the nanopore, the tunneling conductance change between these electrodes can be recorded to decode the base pair sequence directly. In this regard, the integration of an ultra-small transverse electrode with a geometry and position matching the existing nanopore is the main challenge.

However, the conventional structure of a solid-state nanopore is simply a nanometer-sized hole drilled into a thin film that separates two chambers filled with electrolyte solutions. These fabrication techniques usually require an electron beam system in a vacuum environment, and their yields are not quite satisfying. Moreover, the capture rate and translocation rate of the nanopore largely depend on the random walks of DNA molecules due to a simple and small nanopore on a large and flat membrane surface.

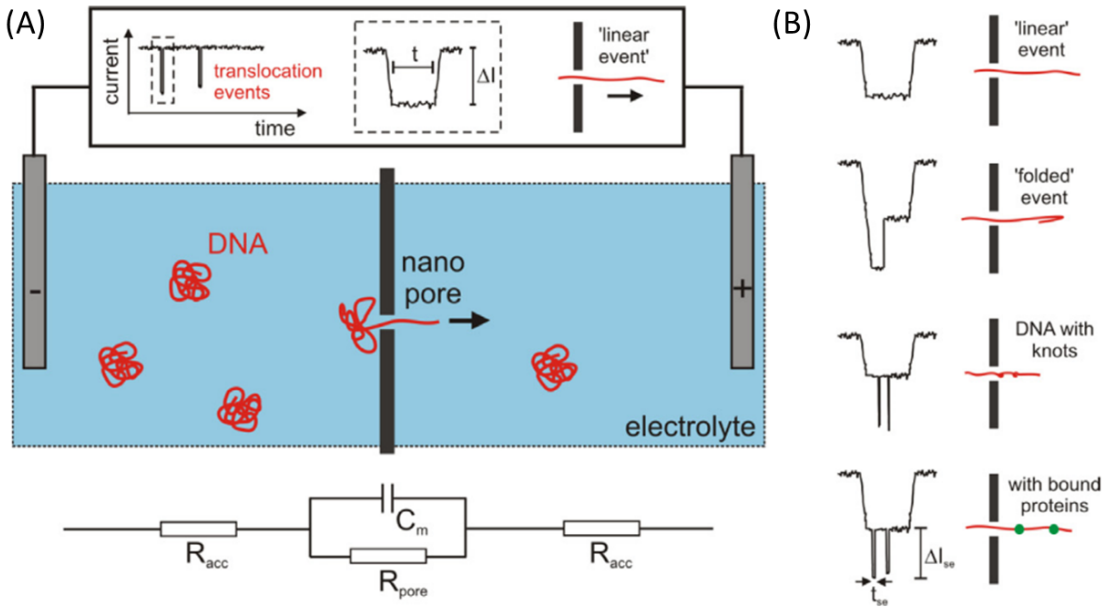

Figure 1.3.1. Nanopore DNA sequencing principle via ionic current. (A) A basic nanopore DNA sequencing setup with an insulating membrane, with a nanopore (black) separating

two reservoirs filled with electrolytes. A potential is applied through the nanopore via electrodes, and DNA molecules (red) are driven through the pore channel. Top: illustration of the ionic current readout of the DNA translocation event. (B) Examples of different translocation signal shapes and the possible DNA structures according to each type of signal. From [30].

To improve this, engineering the distribution of EF at the nanopore entrance may be a solution. The heterogeneous distribution of EFs applied in a medium is known to depend heavily on the characteristics of the wave form, the electric properties of the medium, and channel geometry. Conventional nanopores have a rather uncontrolled distribution of EFs due to their structure, thus increasing the difficulties of ultimate resolution and accuracy for a single-molecule-level detection. In this regard, manipulation of molecules' motions and interactions via a designed EF profile becomes an interesting challenge in the field of nanopore devices. However, conventional fabrication strategies are not suitable for integrating extra structures for direct control and sensing capacities on both biological and solid-state nanopores. This necessitates completely new thinking regarding device fabrication and nanopore preparation to achieve a highly localized and accurate EF modulation at the single-molecule level.

1.4. Summary

In this dissertation, I will report my graduate works based on the EF modulation on cells and molecules, especially DNA molecules. Specifically, in Chapter 2, I will focus on cellular signaling pathway modulation with external EFs. I begin with a brief history of endogenous EFs and applications of exogenous EFs. Then, existing hypotheses of EF-cell coupling and the major signaling pathways involved in cellular responses to external EFs will be introduced. I will discuss existing experiment setups for EF stimulation, as well as previous studies, including theoretical calculations of membrane

protein modulation with alternating current (AC) EFs. Next, I will introduce our microelectrode chip design and platform setup to address the limitations in previous studies, and focus on experiment results on extracellular signal-regulated kinase (ERK) activation modulation with high spatial and temporal resolutions. We have used inhibitor tests to pinpoint the possible coupling mechanisms between the ERK signaling pathway and AC EF stimulation. Finally, I will summarize the open questions and technique challenges, along with prospects for future investigations.

In Chapter 3, I will focus on biomolecule control and sensation with an engineered electric potential profile. The history of nanopore sensing techniques, mainstream nanopore analysis mechanisms and device structure paradigms, and the state-of-the-art solid-state nanopore structures for sequencing will be introduced. Then, I will report our new strategy for constructing the planar-gated nanopore device design in the context of previous approaches which had only limited success. I will explain the fabrication workflow design and the electrochemical deposition process for the final nanopore/tunneling junction preparation. Next, I will present the characterization results of fully assembled devices, together with the first demonstration of simultaneous correlated detection of DNA translocation from both the ionic and the tunneling current channels with high yield. I will also discuss the possible enrichment and translocation control based on statistic data. Finally, I will summarize and discuss the experiment results and the possible future developments and challenges of this planar device platform. In the end, Chapter 4 is an overall conclusion of my graduate projects and the lessons learnt during my graduate period.

CHAPTER 2. SIGNALING PATHWAY MODULATION WITH EF STIMULATIONS

2.1. Introduction

Cells respond to the environment when certain proteins embedded in the membrane sense the extracellular and intracellular stimulations, such as chemical, mechanical and electric signals. These proteins are called integral membrane proteins, and they are embedded within the lipid bilayer plasma membrane. Their functions include transporting ions and molecules across the cell membrane, recognizing neighboring cell types and signaling with the extracellular environment [31]. These proteins normally consist of several parts and obtain net charges and dipoles. It is thus theoretically possible to couple these proteins with electromagnetic fields, create changes in their charge distribution and structure conformation and eventually modulate their behaviors and downstream cellular responses.

In past decades, applications of EFs to cells have been investigated and exhibit interesting and promising results for wound healing, embryonic development, cell migration, proliferation and differentiation, cancer treatment and drug delivery [1, 10, 32-37]. For example, the wound healing process would be accelerated when an EF targeting the wound is applied to the surrounding tissue [38]. However, most studies have long focused on DC EFs for a long time and the applications of AC EF have only recently come into the spotlight. Among these applications, some researchers [39] have demonstrated electroporation and electrofusion by applying an AC EF with a high offset and a short duration to increase the permeability of the cell membrane, thereby allowing for translocations of chemicals, drugs, or DNAs and the fusion of cells, and other studies

[40] have demonstrated that low-amplitude, intermediate-frequency AC EFs have an inhibitory effect on cancer cells. Meanwhile, there are attempts [41, 42] showing the possibility of modulations on cell membrane and signaling pathways. This possibility has made the AC EF stimulation attractive because it may provide a non-invasive and subtle method of cellular response modulation.

In this chapter, I first provide a brief history of endogenous EFs and exogenous EF applications, the existing mainstream hypotheses of interaction mechanisms between EFs and cells, and the signaling pathways involved in these interactions. Then, I introduce the theoretical simulations and early experiments regarding AC EF modulations of cells. Last, I present the cell modulation experiments involving precise ERK activation via external AC EFs through passivated microelectrodes, suggesting that membrane proteins would directly respond to external EFs without any chemical or Faradaic processes.

2.2. History Background of Endogenous and Exogenous EFs in Biological Systems

2.2.1. Endogenous EFs in Biological Systems

Since the mid-1700s, it has been known that electricity can be used to control animal tissue [1]. Early researchers have demonstrated that a frog leg preparation will contract when an electrical discharge from a Leyden jar is applied directly to the nerve or when the cut end of the sciatic nerve touches the leg muscle. This indicates that electricity will stimulate muscle contraction, and the injured tissue seems to display a different electric potential compared to intact muscle. Based on these observations, Carlo Matteucci further investigated this in 1831 by measuring the potential between the cut end of nerves and muscles using a galvanometer, which is named after Galvani [1]. He

then used this injury potential of damaged frog muscle to prove the existence of action potentials in nerves and muscle. After stimulating muscle contraction in an injured muscle with a cut nerve, he successfully activated muscle contraction on a second frog muscle preparation by bringing it into contact with the injured muscle activated via the cut nerve. This demonstrated the potential–later named the action potential–of the uninjured muscle fibers to stimulate the action potentials of intact nerves and muscles in the second preparation. Based on these experiments, a well-known model, namely, the resting potential-action potential model, was established [4, 43, 44]. Before a cell fires, it rests in a polarized state, with a negative membrane resting potential maintained by ion pumps and channels on the cell membrane. When an internal or external stimulus raises the membrane potential to a value above the threshold, it triggers the opening of the voltage-gated sodium channel and the pumping of sodium ion outside, resulting in an increase of the membrane potential and consequently the positive feedback loop of depolarization. Then, potassium channels on the cell membrane with a slower response open and pump potassium outside, and the cell is then polarized and restores the resting state at last.

Another type of endogenous EF is called the injury potential, which was discovered by Emil Du-Bois Reymond in 1843 [1]. He noticed that a current was flowing out from an epidermal wound on his finger and successfully measured this current, which was 1 μA in magnitude. With the development of measurement tools and techniques, further details have been revealed about the formation of such injury potential [45]. When the skin is intact, polarized epithelia transport cations such as Na^+ into the basal side and bring anion such as Cl^- to the apical side and maintain a trans-epithelial potential

difference (TEPD) between the two sides of epithelia. Once a wound is created on the skin, the insulating epithelial layer is disconnected, creating a short loop between the basal and apical sides. The TEPD at the wound will drop and become relatively negative compared to that at the unwounded area. Thus, an EF is established, and the current is driven from the unwounded area to the wound. Further research has demonstrated that this endogenous EF acts as a guidance cue for the wound healing process. Several related cellular behaviors are modulated by this endogenous EF including the directional migration, proliferation and division axis position of epithelial cells, the proportion of nerve sprouting at the wound area, and the directional growth of nerve towards the wound edge [46, 47]. Apart from the skin, other types of wounds will generate this potential. For example, Borgens *et al.* measured the injury current near regenerating newt limbs [48] and the cut ends of Mauthner and Muller axons in embryonic lamprey spinal cord [49].

2.2.2. Exogenous EF Applications on Biological Systems

When endogenous electricity was discovered, using exogenous EF to treat diseases or disabilities became an attractive idea in physiological and pathological research. Despite early attempts based on premature understanding and superstition, recent research has revealed the possibility of modulations or treatments on different biological systems via exogenous EF applications [1, 10, 32-37]. In fact, exogenous EFs could influence biological systems at different levels because of the charges and dipoles in cells. Thus, when an EF stimulation is applied to tissues or cells, the ion channels and receptors on the cell membrane monitoring the cellular and surrounding environment will respond to this stimulation via chemical, mechanical or electric signals, and these

responses will pass to downstream signaling pathways and drive the cells to hyperpolarize or depolarize, migrate, proliferate, and differentiate (Figure 2.2.1). These reactions of individual cells will eventually accumulate and trigger tissue-level responses. Based on this initial understanding of the interactions between cells and exogenous EFs, exogenous EF stimulations have been used and have yielded promising results during wound healing, neuromuscular function restoration, and psychiatric and neurological disorder treatment [6, 50-52]. For example, Borgens *et al.* applied an EF stimulation to enhance the spinal cord regeneration in lampreys [53].

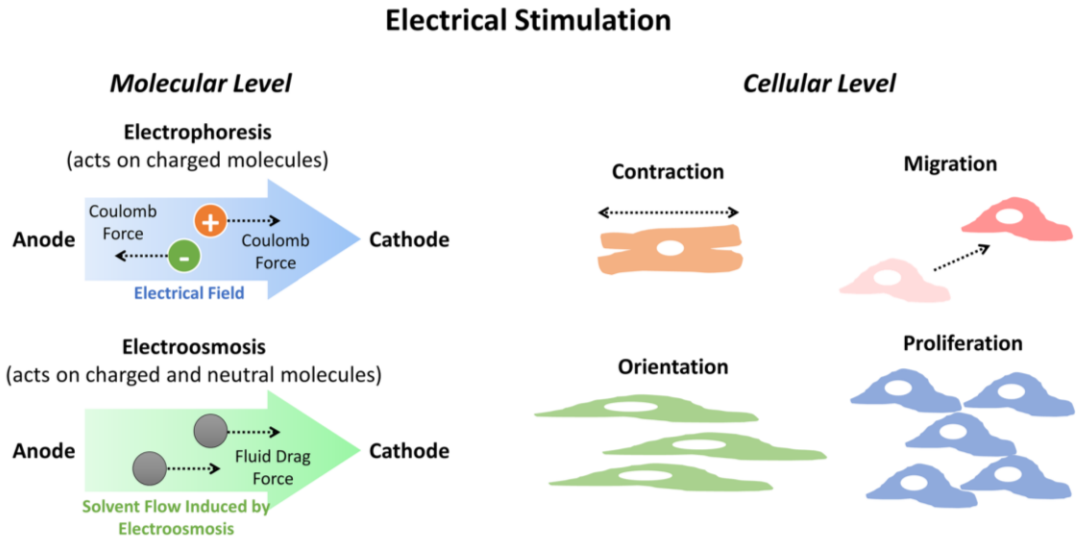

Figure 2.2.1. Different effects under electric field (EF) stimulation at molecular and cellular levels. At the molecular level, electric stimulation will affect both charged and neutral molecules. The Coulomb force induced by EFs will drive charged molecules towards opposite polarities. At the same time, liquid in biological systems will be driven from anode to cathode, dragging both charged and neutral molecules towards the cathode. At the cellular level, cells exhibit different responses under EFs. The right-hand panel illustrates some typical reactions, including contraction, migration, orientation, and proliferation. Such cellular responses can be observed after EF stimulation in a short amount of time. From [10].

2.2.3. Commercial Applications of Exogenous EF Stimulations

The clinical applications of exogenous EF stimulations have been reported in the past few decades. Although several promising applications have been mentioned in the previous section, successful commercial applications focus on two major fields: EF stimulation assisted wound healing and iontophoretic drug delivery.

Since the very beginning of the discovery of injury potential, using EF stimulation to enhance wound healing has been an obvious application. Many researchers have reported their clinical trials using EF stimulation for wound healing, and the results demonstrate the acceleration of wound healing and an increase in cutaneous perfusion in human studies [11]. As a result, medical device companies have already developed commercial wound dressing devices integrating EF stimulation. For example, Biofisica released its bio-electric wound dressing, POSiFECT®RD [12]. The POSiFECT®RD device consists of an anode, which is a soft metal ring set into a hydrogel in the dress, and a small paddle cathode. When this device is used, its cathode sits on the wound bed, and the anode is placed on the outside of the wound bed, applying an electric current to the wound bed. Procellera® is another commercial EF stimulation product developed by Vomaris Innovations [13]. It is a redox-active silver/zinc bioelectric dressing (BED) that generates EFs without an external power supply.

Iontophoretic ocular drug delivery is another application of EF stimulation. Iontophoresis is a transmembrane drug delivery method using an EF gradient on tissue. Compared to conventional methods, iontophoretic ocular drug delivery exhibits a higher efficiency because the force generated by the EF gradient continuously pushes the drug molecules into the eye tissue along the field direction. Furthermore, EyeGate Pharma

developed its drug delivery system, named EyeGate II, to deliver a therapeutic concentration of drugs into ocular tissues [14]. This system is designed based on trans-scleral iontophoresis; the working electrode is placed at the pars plana on the sclera, and the counter electrode is placed on the ear. Drug molecules will then penetrate the sclera and choroid and finally reach the retina or the vitreous under the influence of an EF. This route is used to treat posterior segment diseases, such as macular degeneration.

2.3. Mainstream Hypotheses of Interaction Mechanism between Cells and Exogenous EFs

Although applications of exogenous EF stimulation have demonstrated promising results in wound healing, tissue regeneration and other physiological scenarios, the fundamental mechanism of how exogenous stimulations interact with cells is still unknown. Unlike chemical or mechanical stimulation, researchers cannot currently determine the reaction site and the interactions that trigger cellular responses under EF stimulations. Based on experiment results of exogenous EF stimulation on cells, which mainly focus on cell direction migration under DC EF stimulations (or electrotaxis), five major hypotheses are proposed to explain the mechanism of cellular responses under exogenous EF stimulation, as presented in Figure 2.3.1.

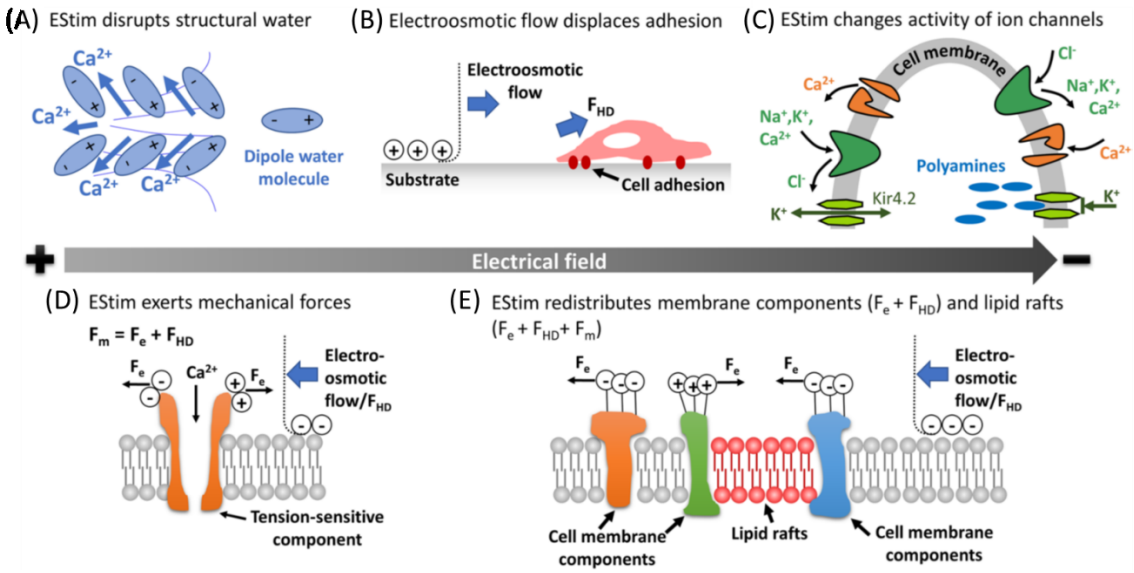

Figure 2.3.1. Hypotheses of the physical mechanism of cellular responses under electric (EF) stimulations. (A) Structural water disruption under EF stimulation causes a calcium wave, the entry of Na^+ ions, and the escape of K^+ ions. (B) Hydrodynamic drag force (F_{HD}) generated by the electroosmotic flow at the charge migration surface will displace the cell adhesion. (C) Polarization and opening of voltage-gated channels under an EF will cause an asymmetric flow of K^+ ions, leading to various cellular responses. (D) The electrostatic and electroosmotic force (F_e) induced by EFs generates mechanical forces (F_m) on tension-sensitive membrane components. These forces drag the cell components, trigger the downstream signaling pathway, and finally cause the cellular responses. (E) Redistribution of membrane components and lipid rafts under force induced by EF stimulation. From [10].

In 2001, Pollack *et al.* proposed a gel model of cells and explained the phase transitions and molecular motion via this model with three examples: the secretory system, the muscle contraction system, and the biological streaming system [54]. When EF stimulation is applied to cells, the ordered arrangement of dipolar water, such as structured water, in the gel-like cell will be disrupted. This change will transform the gel structure into a solution-like structure, releasing a large number of trapped calcium ions to form a calcium wave. At the same time, the disruption of the extracellular structural water allows for a rapid influx of sodium (Na^+) ions into and an efflux of potassium (K^+)

ion from cells. This ion flux during the EF stimulation is a method of controlling the cell size and regulating the cell membrane potential.

In 2009, Huang *et al.* proposed that the electroosmotic fluid flow reorients cells through hydrodynamic drag force (HDF) [55]. They discovered that Ca^{2+} gradients and transients are present in zebrafish keratocytes and are important for internal polarity and migration speed. However, these Ca^{2+} gradients do not affect electrotaxis when testing in a Ca^{2+}-free condition. They thus suggested that cells sense the water flow adjacent to their membrane immediately via HDF, leading to a directional response of the cells. The electroosmotic forces would also affect cell proliferation, differentiation, and embryogenesis [56, 57].

In 2011, Gao *et al.* discovered that a cell will hyperpolarize its anodal side and depolarize its cathodal side when an EF is applied [58]. This polarization will modulate the cell membrane potential and then change the activity of voltage-gated channels for Na^+, K^+, and Ca^{2+}. Therefore, an asymmetric ion flow occurs when ion channels open, thus creating an electromotive force called an electrostatic force. At the same time, intracellular polyamines accumulate toward the cathode side under the influence of an EF, increasing the inward-rectifying property of KCNJ15/Kir4.2—a potassium inwardly rectifying channel—which will block the influx of K^+ ions [59]. Meanwhile, the anode side of the cell will display a decreased inward-rectifying property, thereby creating an asymmetric K^+ ion flow. This asymmetric ion flow and the opening of voltage-gated ion channels will lead to cellular responses to external EF stimulations.

In 2014, Humphrey *et al.* proposed that cells constantly monitor the surrounding environment and respond to it in order to promote homeostasis, including maintaining the

mechanical properties of the extracellular matrix (ECM) [60]. The electrostatic and electroosmotic forces induced by EF stimulation will create mechanical forces on the tension-sensitive components of the cell membrane, including focal adhesion and cadherin adhesion. These components will thus be dragged. Moreover, the mechanical signal will pass through the signaling pathway and change the gene expression, causing changes in cell proliferation, mobility, organogenesis, and development.

In 2007, Finkelstein *et al.* proposed that the redistribution of membrane components determines the direction of electrotaxis instead of the EF-induced polarization of charged cell-surface protein [61]. The electrostatic force and HDF induced by the external EF will redistribute the charged components on the lipid bilayer membrane, creating a polarity along the EF direction. In addition, the lipid rafts will sense and respond to the EF as mobile complexes that polarize and coalesce, and they will eventually activate the intracellular signaling pathway to orient cell migration [62]. This redistribution further polarizes the cell membrane components, including integrin and caveolin, thereby promoting the raft structural stabilization and eventually leading to a directional cellular mobility.

2.4. Signaling Pathways Involved in Cellular Responses under Exogenous EF Stimulations

The first step of how and where EF stimulations interact with cells is not yet clear, the follow-up cellular responses and related cellular signaling pathways can be determined due to the macroscale cellular response and molecular sensing techniques. According to recent studies, two major signaling pathways have proven to be related to cellular responses under exogenous EF stimulations.

The signaling pathway of phosphoinositide 3-kinases (PI3Ks) has been demonstrated as an important component during cellular responses, including electrotaxis, proliferation, and differentiation in different cell types. In 2011, Meng *et al.* reported that EF stimulations on neural progenitor cells (NPCs) will induce both the redistribution of phosphatidylinositol (3,4,5)-trisphosphate (PIP3), which is the downstream effector of PI3K, and the colocalization of actin at the leading edge, which induces asymmetric localizations of signaling molecules and actin cytoskeleton [63]. The NPCs migrate toward the cathode, and the phosphorylation of PIP3 and Akt increases during electrotaxis. Meanwhile, the electrotaxis response reduces when pharmacological inhibition or genetic disruption of PI3K is applied. Sato et al. reported that the migration direction of Dictyostelium cells can be reversed by genetic modification of both guanylyl cyclases (GCases) and the cyclic guanosine monophosphate (cGMP)-binding protein C (GbpC) in combination with the inhibition of PI3K [64]. This finding indicates that PI3K-dependent signaling pathways mediate the EF signal in an actin-dependent manner because the PI3K activity is regulated through a Ras/PI3K/F-actin feedback circuit, whose components may be affected by EF stimulations. Phosphatidylinositol-3,4,5-trisphosphatase (PTEN) is a phosphatase that dephosphorylates PIP3 to phosphatidylinositol (3,4)-bisphosphate (PIP2), resulting in the inhibition of the signal transduction from PI3K to downstream effectors. Zhao et al. reported that PI3K and PTEN regulate the electrotaxis in a coordinated manner during would healing [65]. In this study, the genetic disruption of PI3K decreases EF-induced signaling and reduces the directed migration of healing epithelium in electrical signal responses, while PTEN gene deletion enhances PI3K pathway activation and electrotactic response.

Mitogen-activated protein kinases (MAP kinases or MAPKs) are also important players during cellular response to external EF stimulations. Recent research has found that three major families of MAPKs, namely, ERK, c-JUN N-terminal kinase (JNK), and p38, are involved in that cellular response. In 2012, Li *et al.* reported that EF stimulation induces directional migration toward the cathode of the following HT-1080 fibrosarcoma cells: U87, C6, and U251 glioma cells [66, 67]. The generation of hydrogen peroxide and superoxide is stimulated under the application of EFs, promoting the phosphorylation of ERKs, which leads to MAPK/ERK activation and directional migration. Unlike ERK, the JNK and p38 families' behaviors under EF stimulation are not yet clear. Sheikh et al. demonstrated that a high-frequency EF does not activate MAPK/JNK and MAPK/p38 pathways, while ERK phosphorylation was enhanced in the same experiment with murine microvascular endothelial cells [68]. However, other reports suggest that p38 is activated in neutrophils and keratinocytes under EFs [65]. These results indicate that the MAPK families may not share the same threshold activation condition of EFs, such as frequency and amplitude, in different types of cells. Further investigation is required to fully understand the role of MAPK signaling pathways during EF stimulation.

2.5. Discussion of Common Experiment Setup and Limitations

The abovementioned hypotheses offer possible explanations for how a cell senses exogenous EF stimulation with some components on the cell membrane. However, these arguments are mostly based on the EF-induced changes of structure water, osmotic forces, electrogenic protein behavior, force-sensitive protein reaction, and redistribution of membrane structure. In regard to the impact of such EFs on the membrane-bound components, although some theoretical cell models are reported, quantitative models or

experimental evaluations on specific membrane proteins or biomolecules do not exist. In typical DC EF stimulation tests, the forces exerted on charge components on the membrane or the potential difference across the entire length of the cell is small based on that field strength, and the corresponding energy consumption is almost negligible compared to the thermal energy. Therefore, the observed cellular response in these experiments is less likely to be a direct influence of EF stimulation, but a secondary effect triggered by the EF-induced changes of ions, charges, and dipoles.

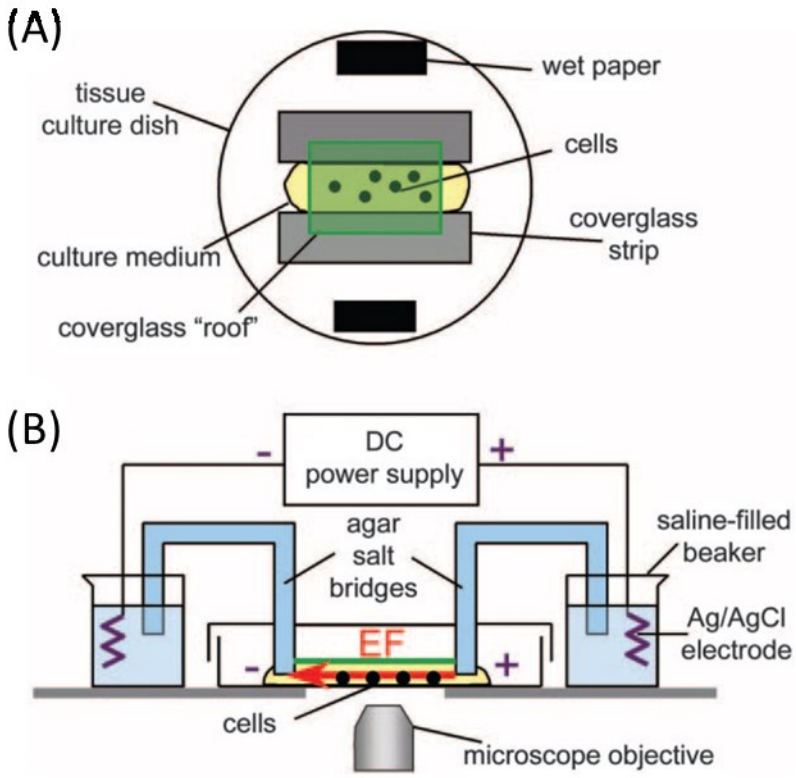

Figure 2.5.1. Schematics of a typical experiment setup of exogenous electric field (EF) stimulation. (A) the top view of the culture chamber. The thin culture chamber is made in a standard 4-inch tissue culture dish. Two coverslips of #1 thickness are fixed on the bottom of the dish. The distance between these two parallel coverslips is approximately 1 cm. Cells are plated into the resulting trough and another coverslip is placed over the top with silicone grease, spanning the entire trough. Strips of paper saturated with water are placed in the

dish to maintain the humidity inside the dish. (B) the side view of the experiment setup mounted on a microscope. Electrical contact is made to the chamber by inserting glass tubes filled with a salt solution gelled with 1% agar through holes in the lid of the chamber. One end of each tube rests in a pool of culture medium continuous with the medium in which the cells are growing; the other end of each tube is placed in a beaker of saline. Ag/AgCl electrodes in each beaker are attached to a direct current (DC) power supply. Fine adjustments to the EF strength are made via a variable resistor in series with the power supply. The field strength is determined periodically by measuring the voltage drop across the length of the central trough [1].

Considering a typical experiment setup of exogenous EF stimulation, as illustrated in Figure 2.5.1, the physiological EF is simulated by applying an exogenous EF via salt bridge references through a thin culture chamber. The stimulation experiment setup is usually mounted on an optical microscope in a controlled environment, and the total stimulation would last for hours. After the stimulation, electrophoresis related molecule sensing techniques are used to determine the critical molecules involved in the cellular response process. All these setups contribute to two problems. First, the exogenous EF application on cells is usually accompanied by net ionic current flows and/or Faradaic processes. For example, redox reactions at the electrode/medium interface will cause appreciable changes in pH and reactive oxygen species (ROS) levels, which would impact the possible direct interaction between cells and exogenous EFs. Second, the exogenous EF is applied globally and the results are typically evaluated from an ensemble of cells after hours of simulation. According to these problems, the stimulation result only records the averaged *ex situ* responses from a large population of cells, which could mix the response events that occur at different time periods and locations during the long stimulation. For example, distinguishing the first cell responses to exogenous EF from the averaged result is difficult. Meanwhile, cells that respond to

EF early would interact with adjacent cells and surrounding environments via chemical signals or cell-cell signaling. This complicates the result and makes it impossible to determine the true response of cells under a pure influence of exogenous EFs.

2.6. Theoretical and Experimental Works on Cellular Modulation via AC EF Stimulation

To avoid the issues mentioned in conventional experiments focusing on DC EF stimulation, exogenous AC EF stimulation on cells may bring about a new aspect regarding the interaction mechanism between cells and EFs. In the past decades, research into AC EF stimulations on cells has revealed the possibility that an exogenous AC EF at certain frequency may couple directly with membrane associated biological molecules [69, 70]. In this section, I introduce the simulation model of cells under AC EF stimulation and related experiment results showing the direct modulation of biological molecules associated with the cell membrane.

2.6.1. Theoretical Simulation of Cells under AC EF Stimulation

The simulation of cells under AC EF stimulation is an attractive topic, and various models have been discussed since Fricke's model concerning the steady-state transmembrane voltage for a cell of the general ellipsoidal shape with negligible membrane conductance and a highly polarizable cytoplasm in 1953 [71]. The following sections describe some models for AC EF stimulations on cells and their possible influences on membrane potentials. Note that the following models use complex numbers for convenient calculation of EF, and the real part of the answers is the EF we needed.

2.6.1.1. Membrane Potential under AC EF Stimulation

Schwan's model, which mainly focuses on the frequency and time dependence of biological material properties [72, 73], represents a solid foundation for the simulation of

AC EF stimulation on single cells. In this model, a single cell is considered as a sphere with a core and a shell structure. The shell, the core, and the space outside the sphere represent the cell membrane, the cytoplasm and the medium respectively. The complete model also includes following assumptions: (1) the thickness of the cell membrane (h) is much smaller than the cell radius (R); (2) the effect of the high frequency Maxwell-Wagner relaxation is neglected; (3) the membrane is perfectly insulating; (4) the conductivity of the electrolyte is uniform; and (5) the potential is a solution of the Laplace equation. The potential induced by an external EF across the membrane of a spherical cell in suspension is thus usually given by the following equation:

$$\Delta U = \frac{1.5ERcos\theta}{1 + i\omega RC_m(\rho_i + \rho_a/2)} \quad (1)$$

where E is the value of the external field strength in the electrolyte, R is the radius of the cell, θ is the polar angle with respect to the direction of the field, ω is the angular frequency of the field, $C_m = \epsilon_m/h$ is the capacitance of the membrane per unit area, ϵ_m is the absolute permittivity of the membrane, h is the thickness of the membrane, ρ_i is the resistivity of the interior of the cell, and ρ_a is the resistivity of the electrolyte. The membrane potential is thus independent of frequency until ω is comparable to the reciprocal of the time constant:

$$\tau = RC_m(\rho_i + \rho_a/2) \quad (2)$$

Consider a typical physiological condition, $C_m = 10^{-2}$ F/m^2, and the values of ρ_i and ρ_a are approximately 1 Ω·m. This means when the frequency of an AC EF ranges between the upper KHz and the lower MHz, the potential across the cell membrane is related to the frequency applied for typical cell sizes (1~100 μm). To calculate the

membrane potential, the effects due to the diffusion are neglected. Meanwhile, the cell is considered to have a finite membrane conductance per unit area G_m, and to be surrounded by a surface compartment characterized by a surface admittance per unit area Y_s. Here, G_m is related to radial currents flowing through the membrane, and Y_s is related to the tangential current flowing around the cell. In these regards, the membrane potential can be calculated by solving Laplace's equation in the four media of the model consisting of the cell cytoplasm, the membrane, the conducting shell and the unbounded external medium, as illustrated in Figure 2.6.1. For the membrane, the complex conductivity is

$$K_m = G_m h + i\omega C_m h \tag{3}$$

For the conducting shell, the conductivity is

$$K_s = Y_s/d \tag{4}$$

Furthermore, the potentials in the four different regions have the following general form:

$$U_j = U_j(r) = -A_j r cos\theta + B_j R^3 \frac{cos\theta}{r^2} \tag{5}$$

where j is the labeling for different regions.

The membrane potential is thus given by the following form:

$$\Delta U = U_m(R-h) - U_m(R) = \left[A_m x \times B_m \frac{3\gamma - x}{1-3\gamma}\right] R cos\theta \tag{6}$$

where

$$\begin{gathered} x = h/R \\ 1 - 3\gamma = (1 - h/R)^3 \\ A_m = \frac{K_a K_s (K_i + 2K_m)(1+3\delta)E}{Den2} \end{gathered} \tag{7}$$

$$B_m = \frac{K_a K_s (K_i - K_m)(1 - 3\gamma)(1 + 3\delta)E}{Den2}$$

$$Den2 = K_s[K_m(K_i + 2K_a) - 2\gamma(K_i - K_m)(K_m - K_a)] + \delta(K_s + 2K_a)[K_m(K_i + 2K_s) - 2\gamma(K_i - K_m)(K_m - K_s)]$$

$$1 + 3\delta = (1 + d/R)^3$$

Therefore, when $h \ll R$ and $d \ll R$, the membrane potential is then

$$\Delta U = \frac{3K_a(K_a + xK_m)Ehcos\theta}{K_m(K_i + 2K_a + 2\,Y_s/R) + 2x(K_m^2 + K_i K_a + K_i Y_s/R)} \tag{8}$$

and the frequency dependence of this membrane potential expression is plotted in Figure 2.6.1.

Neglecting the high frequency relaxation, and considering that $RG_m\rho_i \ll 1$ and that the surface admittance is real, $Y_s = G_s$. The membrane potential reduces to

$$\Delta U = \frac{1.5ERcos\theta}{1 + \frac{\rho_a G_s}{R} + R(G_m + i\omega C_m)\left[\rho_i + \frac{\rho_a}{2} + \frac{\rho_i \rho_a G_s}{R}\right]} \tag{9}$$

If there is no surface conductance, then the membrane potential reduces to

$$\Delta U = \frac{1.5ERcos\theta}{1 + R(G_m + i\omega C_m)\left[\rho_i + \frac{\rho_a}{2}\right]} \tag{10}$$

If the membrane conductance can be neglected, but there is a surface conductance, then the membrane potential would be

$$\Delta U = \frac{1.5ERcos\theta}{(1 + \frac{\rho_a G_s}{R} + i\omega RC_m)\left[\rho_i + \frac{\rho_a}{2} + \frac{\rho_i \rho_a G_s}{R}\right]} \tag{11}$$

Therefore, the membrane potential will decrease when the frequency ranges from the upper kHz to the lower MHz and this decrease is mainly due to the surface conductance of cells.

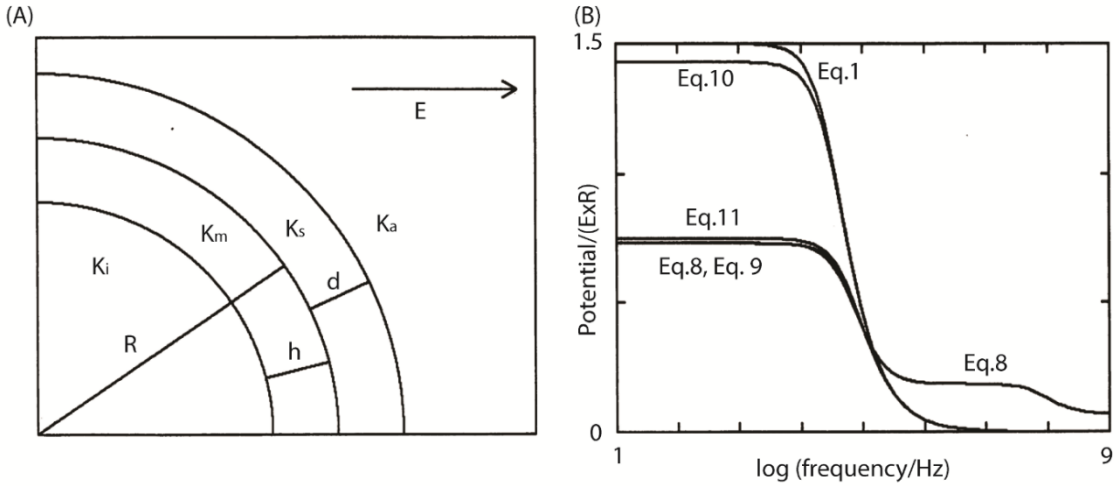

Figure 2.6.1. (A) Schematic representation of the cell model suspended in an electrolyte. The cell is considered to be a spherical cell in suspension, where R is the radius of the cell; h is the cell membrane thickness; d is the thickness of the conducting shell with an enhanced ion density close to the cell membrane; K_i, K_m, K_s *and* K_a are the conductivities of the cell interior, the cell membrane, the conducting shell, and the external medium, respectively; E is the field strength of the external EF stimulation. (B) The membrane potential changes with the frequency of EF stimulations according to different theoretical expressions. The labels of the curves correspond to the equation labels. From [73].

2.6.1.2. Minimum AC EF Stimulation for Membrane Potential Changes Larger than Thermal Fluctuations

Weaver *et al.* calculated the smallest EF stimulation required for cells to trigger changes greater than those due to random fluctuations such as thermal noise [74]. The thermal noise of the membrane potential in a resistance *R* is given by

$$\overline{(\delta U)_{kT}^2} = 4RkT\Delta f \tag{12}$$

where the product of the Boltzmann constant and the absolute temperature $kT \approx 0.025\ eV$ at 310 K, Δf is the frequency bandwidth within which information is sought, and $\overline{(\delta U)_{kT}^2}$ denotes a time average. Meanwhile, a cell membrane can be treated as a

combination of a resistance R and a capacitance C, resulting in an effective bandwidth $\Delta f = 1/(4RC)$ and a broad-band estimate of the thermal noise, $\overline{(\delta U)_{kT}^2} = kT/C$.

Thus, the capacitance for a spherical cell membrane of a cell radius r_{cell} is $C \approx \epsilon_0 K_m 4\pi r_{cell}^2/d$ and the thermal noise is

$$\overline{(\delta U)_{kT}^2} = kT\, d/(4\pi\epsilon_0 K_m r_{cell}^2) \tag{13}$$

where ϵ_0 is the free space permittivity, K_m is the membrane's dielectric constant and d is the membrane's electric thickness.

As discussed in the previous section, the change in membrane potential triggered by AC EF for a simple case of a perfectly insulating spherical shell membrane is $\Delta U_{max} \approx 1.5 E r_{cell}$, and the minimum AC EF stimulation needed to overcome the thermal normal will follow the relation $\Delta U_{max} \approx (\delta U)_{kT}$. The minimum AC EF stimulation applied thus follows the following equation:

$$E_{min} \approx \frac{2(\delta U)_{kT}}{3r_{cell}} = \frac{2}{3}\left[\frac{kTd}{4\pi\epsilon_0 K_m}\right]^{\frac{1}{2}} \frac{1}{r_{cell}^2} = \frac{2A}{3}\frac{1}{r_{cell}^2} \tag{14}$$

For a spherical cell with a cell radius r_{cell} of 10 μm, assuming that the membrane's dielectric constant K_m is typically 2 to 3 and the membrane's electrical thickness d is 50 Å, the magnitude of the minimum EF E_{min} is 20 mV/cm. For large elongated mammalian cells, the change in membrane potential will be $\Delta U_{max} \approx 0.5 E L_{cell}$, where L_{cell} is the length of the simplified cell (a cylindrical tube), and r_{cell} is its radius. The minimum EF for the elongated cell is

$$E_{min} \approx \frac{2(\delta U)_{kT}}{L_{cell}} = 2\sqrt{2}A\frac{1}{r_{cell}^{1/2} L_{cell}^{3/2}} \tag{15}$$

The magnitude of the minimum EF E_{min} is approximately 0.8 mV/cm for an elongated cell with L_{cell} =150 μm and r_{cell} = 25 μm.

If the bandwidth Δf is limited and the AC EF of fundamental frequency f is applied for a limited time period τ, then the minimum AC EF stimulation for elongated cells is

$$E_{min,\ \Delta f} \approx 2\sqrt{2}\left[\frac{\rho_m kTd\Delta f}{\pi}\right]^{1/2} \frac{1}{r_{cell}^{1/2} L_{cell}^{3/2} (f\tau)^{1/2}} \tag{16}$$

where ρ_m is the membrane resistivity.

Because the conformational transitions involve intramolecular movement of charges and dipoles in biological molecules, the changes due to the membrane potential alterations will induce electroconformational transitions, resulting in membrane-associated, enzyme-catalyzed reactions [70]. The enzyme electroconformational coupling is typically frequency dependent, and the typical frequency range of optimal coupling for many enzymes is from 100 Hz to 1 MHz, with a bandwidth Δf larger than 10 Hz.

2.6.1.3. Power Dissipation on Different Regions of a Cell under AC EF Stimulation

Kotnik *et al.* theoretically calculated the distributed power dissipation in biological cells under EFs in 2000 [75]. In their calculation, a biological cell was treated as a core/shell structure sphere for a second-order model with dielectric relaxation, representing the cell cytoplasm and membrane respectively, as illustrated in Figure 2.6.2. According to the experiment data, both cytoplasm and membrane have conductivity and dielectric permittivity, and these two parameters will be affected by the dielectric relaxation of water molecules. With these assumptions, the membrane voltage induced by the EF of amplitude E_e is given by the following equation:

$$U_m(\omega) = F_{S(2+DR)} E_e R cos\theta \tag{17}$$

with R denoting the cell radius and θ being the polar angle with respect to the EF direction. Moreover, $F_{S(2+DR)}$ is given by

$$F_{S(2+DR)} = \frac{3\sigma_{et}[3dR^2\sigma_{it} + (3d^2R - d^3)(\sigma_{mt} - \sigma_{it})]}{2R^3(\sigma_{mt} + 2\sigma_{et})(\sigma_{mt} + 0.5\sigma_{it}) - 2(R-d)^3(\sigma_{et} - \sigma_{mt})(\sigma_{it} - \sigma_{mt})} \tag{18}$$

where d is the membrane thickness, and σ_{it}, σ_{mt}, and σ_{et} are the admittivity of the cytoplasm, the membrane, and the cell exterior respectively, expressed by the following equations:

$$\begin{aligned} \sigma_{it} &= \sigma_i(\omega) + j\omega\varepsilon_i(\omega) \\ \sigma_{mt} &= \sigma_m(\omega) + j\omega\varepsilon_m(\omega) \\ \sigma_{et} &= \sigma_e(\omega) + j\omega\varepsilon_e(\omega) \end{aligned} \tag{19}$$

where $\sigma_i(\omega)$, $\sigma_m(\omega)$, $\sigma_e(\omega)$, $\varepsilon_i(\omega)$, $\varepsilon_m(\omega)$, and $\varepsilon_e(\omega)$ are effective conductivities and permittivities, which obey the following equations:

$$\begin{aligned} \sigma(\omega) &= \sigma(0) + \omega \sum_{k=1}^{n} \frac{\Delta\varepsilon_k \omega\tau_k}{1 + \omega^2\tau_k^2} \\ \varepsilon(\omega) &= \varepsilon(0) - \omega \sum_{k=1}^{n} \frac{\Delta\varepsilon_k \omega\tau_k}{1 + \omega^2\tau_k^2} \end{aligned} \tag{20}$$

where ω = 2πf, with f denoting the field frequency. Moreover, n is the number of steps of dielectric relaxation of the material, $\Delta\varepsilon_k$ is the magnitude of the k-th relaxation step, and τ_k is the time constant of the k-th step, while $\sigma(0)$ and $\varepsilon(0)$ are the conductivity and dielectric permittivity, respectively.

Assuming that θ = 0, the membrane voltage and membrane EF are as follows:

$$U_m(\omega) = F_{S(2+DR)} E_e R \tag{21}$$

$$E_m = \frac{U_m}{d} = \frac{F_{S(2+DR)} E_e R}{d} \tag{22}$$

The power dissipation in the membrane is thus given by

$$P_m = \sigma_{mt} \bar{E}_m^2 = \frac{\sigma_{mt} F_{S(2+DR)}^2 E_e^2 R^2}{d^2} \tag{23}$$

Based on the experiment data of cytoplasmic, membrane, and extracellular effective conductivities and permittivities (Figure 2.6.2), both the ratio of the membrane field to the EF (E_m/E_e) and the power dissipation in different regions in cells are plotted. The membrane field starts to decrease, and the membrane power dissipation begins to increase at approximately 10^5 Hz. This suggests that power dissipation in different regions may reflect the interaction between EFs and different cellular components.

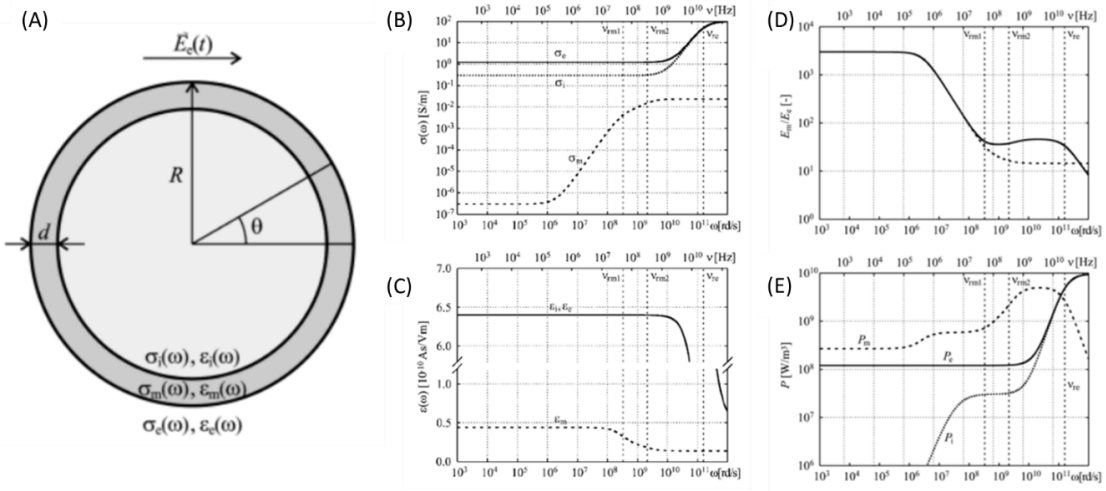

Figure 2.6.2. Theoretical evaluation of power dissipation in biological cells under an alternating current (AC) electric field (EF) [75]. (A) The cell schematics of the second-order model with dielectric relaxation. (B, C) Cytoplasmic, membrane, and extracellular effective conductivities and effective permittivities as functions of field frequency. (D) The ratio of the membrane field to the EF (E_m/E_e) as a function of frequency (solid line) and the corresponding prediction of the second-order model without dielectric relaxation (dash line). (E) Power dissipations in cytoplasm, membrane, and cell exterior at $E_e = \sqrt{2} \times 100\ V/cm$ as functions of frequency [75].

2.6.2. Experiment Works Regarding Cellular Modulations via AC EF Stimulation

Following theoretical simulations of possible membrane molecule modulation via AC EFs, modulations of cell functions are the next step. Chen demonstrated the synchronization of ion exchangers via an AC EF stimulation [76]. The Na^+/K^+ pump is one of the ion exchangers in the cell membrane, maintaining the Na^+ and K^+ concentrations inside and outside the membrane. In general, one Na^+/K^+ pump will transport three Na^+ ions to the extracellular environment and pump two K^+ ions into the intracellular environment by consuming the chemical energy during the hydrolysis of one adenosine triphosphate (ATP) in each cycle. By applying a square signal of 50 Hz, the membrane potential will be alternated from -30 mV to -150 mV at a membrane holding potential of -90 mV. During each cycle, the positive period, which is equivalent to a DC depolarization pulse, provides enough energy to transport two ions, thereby facilitating the Na^+ extrusion and hindering the K^+ influx. Meanwhile, the negative period will facilitate the K^+ influx and hinder the Na^+ extrusion. After several cycles of AC EF application, the Na^+ extrusion and K^+ influx processes of pumps will synchronize at the positive period and the negative period separately. Such a change in ion exchanger behavior results in a pattern change of the Na^+/K^+ pump current. Before the synchronization, ion pumps work randomly and the Na^+ extrusion and K^+ influx cancel each other. The AC EF stimulation synchronizes the pump behaviors so that all pumps extrude Na^+ ions during the positive period and pump in K^+ ions during the negative period. This is reflected by the current monitoring that outward current is 1.5 times the inward current, which follows the ion exchange ratio of one pump cycle.

The fundament principle of such synchronization is that the field-induced energy changes the ion transportation rate. This Na^+/K^+ pump is actually electrogenic and the process will be affected by membrane potential changes directly. However, there are other membrane molecules that are non-electrogenic and this synchronization method may not be applicable.

2.7. ERK Activation via AC EF Stimulation

According to the discussion in previous sections, researchers have been investigating cellular responses under exogenous EF stimulations over the past decades. Utilizing exogenous EFs to trigger cellular responses is an attractive research area for EF-based treatments as well as for the triggering of desired biological processes. However, apart from some early results regarding general theoretical simulations that work for all types of EFs, researchers focus on DC EF applications, such as wound healing, physical therapies, and drug delivery, and AC EF stimulations that achieve research or medical goals by damaging the cell integrity such as electroporation. At the same time, while studies and clinical trials have demonstrated the feasibility of DC EF stimulations, electroporation and radiofrequency ablation, the fundamental mechanism of interactions between cellular responses and EF stimulation is not yet clear.

To address this, the behaviors of membrane proteins and the downstream signaling pathways under exogenous EFs should be carefully examined. However, current research related to exogenous EF applications does not use the intermediate frequency range that may trigger membrane potential changes and possible conformational transitions of biological molecules based on theoretical models and experiment results. Meanwhile, the EF application setup usually involves a long-term

stimulation on a large population of cells, and it does not use real-time molecule detection methods. All these issues leave the cellular response process fraught with too many different parameters, including chemical, mechanical, and electrical signals, and experiment data from different research groups are consequently confusing or even contradictory and difficult to standardize and compare.

The project of ERK activation via intermediate frequency AC EF stimulation investigates the interaction between exogenous AC EF stimulation and membrane proteins in the frequency range that has been previously considered to have no biological effects. To avoid the possible interferences induced by the EF application and to achieve stimulation at the cellular level, we developed a microelectrode array chip that delivers AC EF signals to target cells within micron-level accuracy. Along with this new stimulation device platform, genetically modified epithelial cells were used for real-time imaging and quantification of the cellular response under the AC EF stimulation. In the following sections, I first explain the experiment design and the device characterization before introducing the ERK activation modulation results based on our device, and I finally discuss the possible mechanism of the interaction between signaling pathways and exogenous EF stimulations.

2.7.1. Experiment Setup Design and Characterization

2.7.1.1. EF Stimulation Device Design and Fabrication

Compared with the conventional experiment setup, the main issue lies in the possible EF-induced chemical signals and the mixed and averaging effect of response behaviors after a long-term stimulation on a large population of cells. To avoid these issues, the following points should be considered for the new EF stimulation device.

First, this device should be designed to apply an AC EF stimulation signal close to target cells without causing changes in local environment parameters, such as pH, temperature, Faradaic current, and ROS. Second, this device should have a strong capability of integration with commonly used real-time observation methods. Finally, the fabrication process should be simple, reproducible, and easy to scale up. Based on all of these considerations, the entire device that we designed consists of three components: (1) the microelectrode array chip for EF stimulation, (2) the confinement chamber as a medium reservoir, and (3) the printed circuit board (PCB) as a connection interface.

The microelectrode array chip is the center piece of the EF stimulation device. Figure 2.7.1 depicts the design of the microelectrode array chip. The pattern is usually defined on a 24×40 mm^2 rectangle glass coverslip with a #1 thickness (~170 μm), which is compatible with most optical microscope systems. The microelectrode array is designed at the center of the chip, with an area of 4×2 mm^2, and three groups of parallel microelectrode pairs are located in this center area. Each group has different microelectrode pairs with different orientations and distances, designed to simultaneously and individually stimulate different locations of a large population of cells.

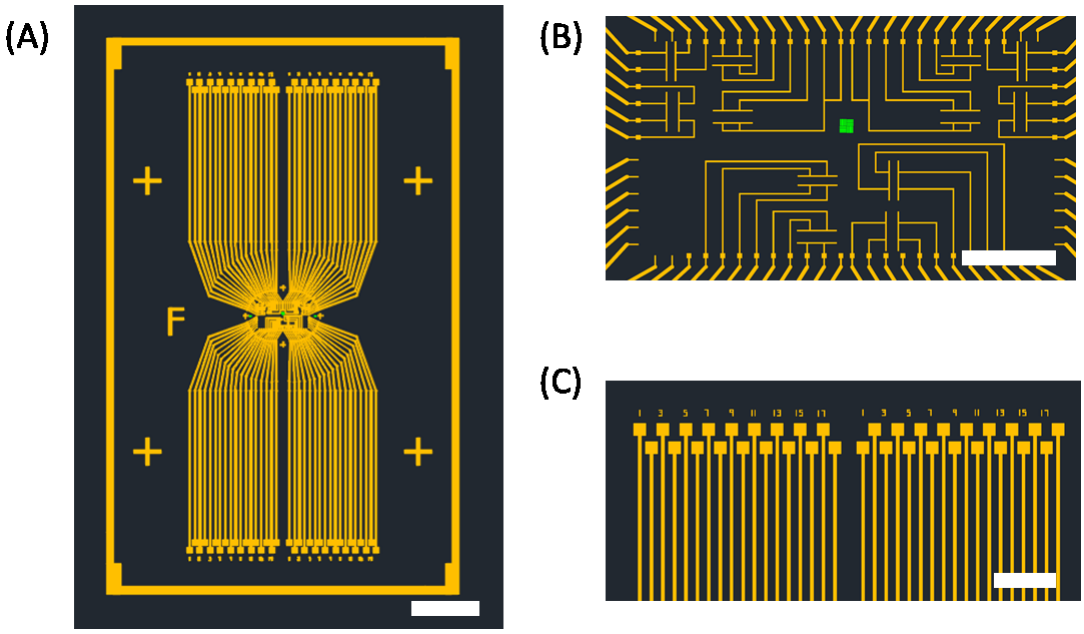

Figure 2.7.1. The AutoCAD design of the microelectrode array chip. (A) The overall design of one microelectrode array chip. This pattern is defined on a glass coverslip of 24×40 mm2. Scale bar: 5 mm (B) The center area of the microelectrode array. There are three groups of microelectrode pairs. Each group contains microelectrode pairs with different gap sizes and orientations, which are used for simultaneous stimulations with various EF strengths and orientations on cultured cells. Scale bar: 1 mm. (C) The connection pads between center microelectrodes with external instruments. The top and lower ends of the pattern are designed to have an easy connection to external instruments through wire bonding. Scale bar: 2 mm.

This microelectrode array chip is fabricated via photolithography methods and thin film deposition techniques. Before fabrication, substrate glass coverslips are cleaned with Piranha (a 3:1 mixture of concentrated sulfuric acid with 30% hydrogen peroxide) heated at 80 ℃ for 30 min to clean off any organic compounds and hydroxylate the glass surface. A 740 nm thick silicon oxide layer is then deposited on the glass surface via a plasma enhanced chemical vapor deposition (PECVD) system to increase the surface uniformity and smoothness. The fabrication of the microelectrode array structure includes three main steps. First, a microelectrode array structure, which has a gap distance ranging

from 50 to 200 μm in each microelectrode pair, is defined in the center area of the chip via standard photolithography techniques, followed by a bilayer metal structure of Cr/Au (1.5 nm / 25 nm) deposited via thermal evaporation. Second, an outer electrode pattern, which is used to connections of the center microelectrode array area, is defined via standard photolithography techniques and then a bilayer metal structure of Cr/Au (1.5 nm/50 nm) is deposited via thermal evaporation. Third, a uniform coating of hafnium oxide (HfO_2) is deposited on the entire chip surface, except for the connection pads via atomic layer deposition (ALD). The HfO_2 layer acts as an insulating layer, preventing possible faradic processes from occurring during the AC EF stimulation. After this fabrication, the metal connection lines are passivated by SU8 polymers via photolithography, excepting the parallel microelectrode pairs.

The cell chamber is designed as a medium reservoir and channel confinement. Figure 2.7.2 illustrates the design of the cell chamber and the way in which it is assembled with the microelectrode array chip. This cell chamber is made with a polycarbonate plate via a milling machine. Along the two sides of the cell chamber, two reservoirs are defined to store enough culture medium for cells. The bottom surface at the center is thinned by approximately 340 μm, and an observation window is opened. A piece of glass coverslip is cut to fit the size of the observation window, and it is supported by two strips of glass coverslips on the edge, forming a thin channel with an estimated height of 170 μm after binding with the microelectrode array chip. The center microelectrode area is exposed in the thin channel, allowing cells to culture on it before the EF stimulation experiments. These structures are sealed and bound with biocompatible silicone elastomer to avoid possible cellular toxicities.

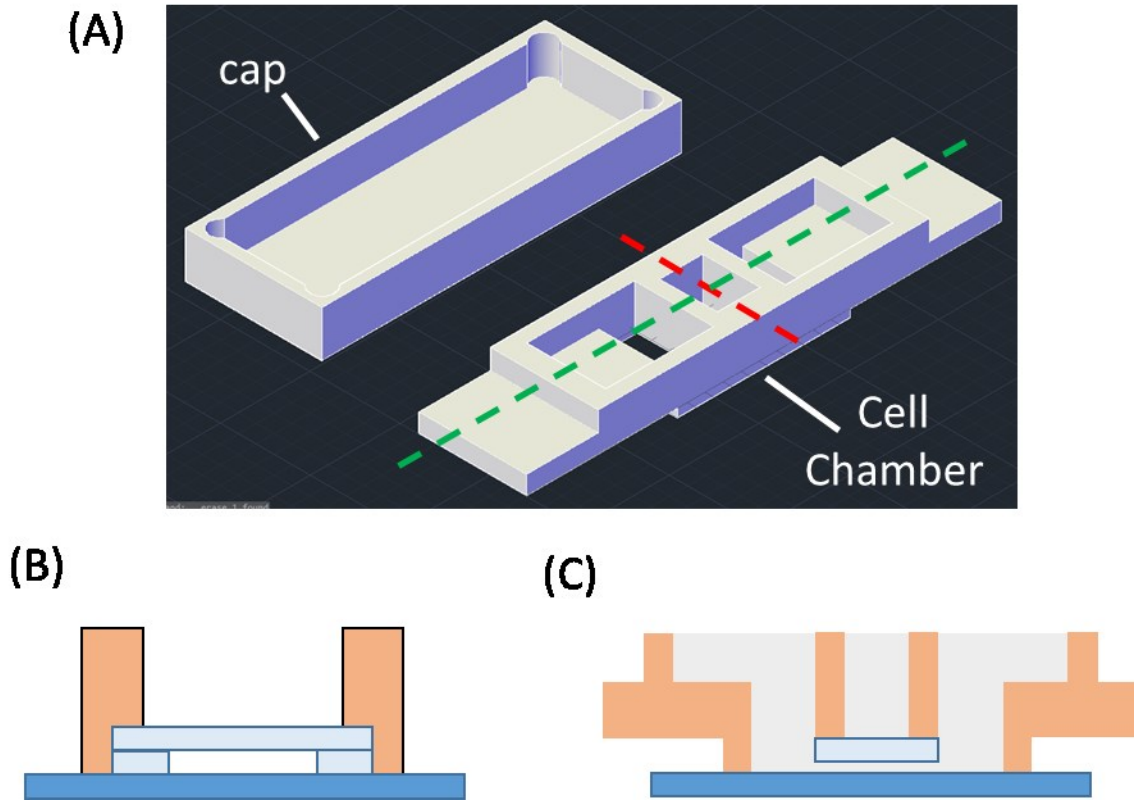

Figure 2.7.2. The design of the cell chamber. (A) The CAD design of the cell chamber and its cap. The cap is used to prevent medium evaporation during the electric (EF) stimulation experiment. (B) The cross section view of the center thin channel, denoted by the red dashed line in (A). This channel is formed by the device chip, the cell chamber and glass coverslips. (C) The cross section view of the cell chamber, indicated by the green dashed line in (A). It shows the two reservoirs on two ends and the optical window in the center. The yellow color denotes the polycarbonate cell chamber, the light blue color denotes the glass slides, and the deep blue color denotes the device chip substrate.

The customized PCB is designed and fabricated as an interface between the microelectrode array chip and external instruments. The assembled chip is fixed on the PCB with polymethyl methacrylate (PMMA), aligned with the center observation window, allowing direct optical access to dry and immersion objective lenses. The connection pads on the microelectrode array chip are connected to the PCB via wire

bonding. Figure 2.7.3 presents the image of the assembled device which is ready for cell culture and experiments.

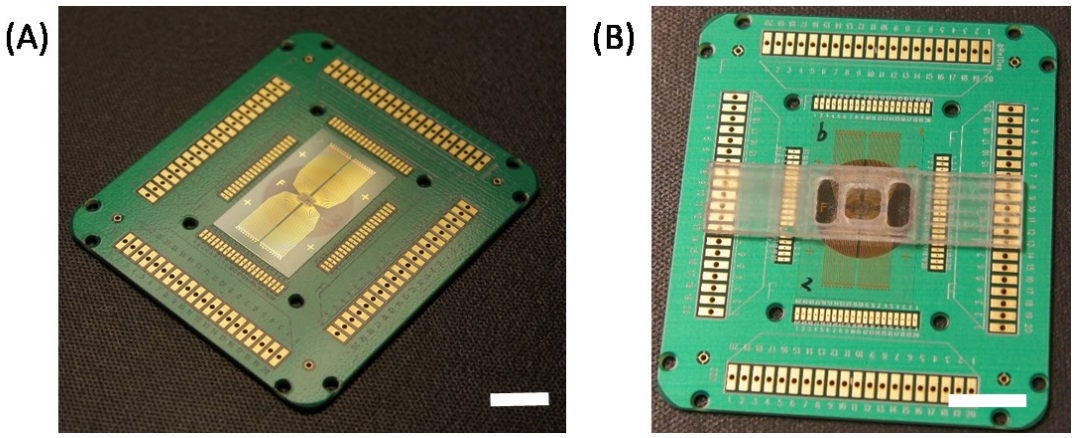

Figure 2.7.3. Images of the assembled device. (A) Image of the microelectrode array chip fixed on the customized printed circuit board (PCB). Scale bar: 2 cm. (B) The image of the assembled device, which is ready for cell culture and experiments.

2.7.1.2. Cell Type Selection and Culture.

Apart from using a new platform, another issue to be solved is the complicated process of protein characterization after the experiment. Common practice is to use electrophoresis based methods to determine the active species in signaling pathways during EF stimulation, which is time consuming and mixes effects from various biological processes. Recent developments in fluorescence labeling and genetic modification provide real-time and non-invasive observation of the response along the signaling pathway. Early attempts to detect different components on or within the cell membrane have involved immunofluorescent analysis to demonstrate the changes under EF stimulation. This method provides a straightforward demonstration of membrane protein redistribution under EF stimulations. Min et al. demonstrated the asymmetric

redistribution of epidermal growth factor receptors (EGFRs) after 20 min of EF stimulation with fluorescent-labelled epidermal growth factor (EGF) [77], showing that EGFR activation may be an early event in EF-directed migration. Moreover, Meng *et al.* showcased PIP3 asymmetric redistribution after EF exposure, highlighting the important role of the PI3K/Akt signaling pathway during the directed migration of NPC under EF stimulation [63]. These experiments using fluorescence labeling successfully demonstrate the membrane protein redistribution under EF stimulation; however, traditional analytical methods are still required for the detection of phosphorylation during the response of the signaling pathway.

To visualize the real-time process of phosphorylation during cellular response to the external environment, two commonly used genetically modified fluorescent labels have been invented, as depicted in Figure 2.7.4. Harvey *et al.* developed a genetically encoded, fluorescence resonance energy transfer (FRET) sensor for ERK activity, namely, the ERK activity reporter (EKAR), showing a high signal-to-noise ratio (SNR) and an optimal fluorescence lifetime imaging, since EKAR is correlated with ERK phosphorylation, which is only associated with ERK activity [78]. This sensor allows for the monitoring of ERK activity in the same cells for a long-term experiment and reveals additional levels of ERK signaling complexity.

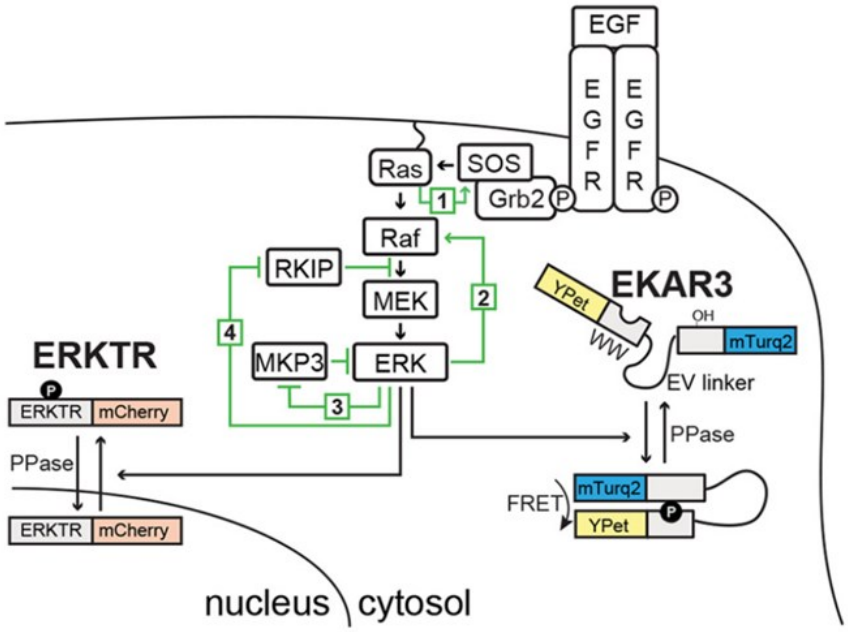

Figure 2.7.4. Schematic of two genetically modified fluorescence reporters for extracellular signal-regulated kinases (ERK) signaling pathway. Green arrows indicate positive feedback loops. The canonical ERK signaling pathway is illustrated in the schematic. ERK phosphorylation triggered by epidermal growth factor (EGF) will change the fluorescence properties of the two types of genetically modified reporters. ERKTR is a fluorescently tagged single peptide reporter that contains both an ERK docking site and consensus motifs for ERK phosphorylation. It is phosphorylated by ERKs when ERK activity increases. This change causes ERKTR to be exported to cytosol from the nucleus, where ERKTR localizes during an un-phosphorylated state. EKAR3 is a FRET-based sensor, and it displays a blue color when it is in a non-phosphorylated state. The conformational changes of EKAR3 induced by ERK activity will change the emission light wavelength to yellow. Both genetically modified fluorescence reporters allow for real-time imaging of cellular responses. From [79].

However, a FRET-based ERK sensor has its limitation in widespread utilizations. In practice, it has a low SNR and may not reflect the downregulation of the kinase because the closed conformation of the FRET sensor is stable, and its phosphorylated sites are not accessible to phosphatases. Regot *et al.* developed a technique to generate reporters of kinase activity for individual cells, converting phosphorylation into a

measurable nucleocytoplasmic shuttling event [80]. In this study, they constructed kinase translocation reporters (KTRs) for JNK activity translating phosphorylation into a localization change. Researchers have juxtaposed a docking site for a kinase to a module, which contains a phosphor-inhibited nuclear localization signal, a phosphor-enhanced nuclear export signal, and a fluorescent protein. When the kinase is inactive, the corresponding KTR is not phosphorylated and mostly nuclear, and when the kinase is active, the phosphorylation of KTR results in cytoplasmic translocation. This KTR technique can also be used to construct reporters of other MAP kinases, such as ERK and p38. Some researchers [79, 81] have demonstrated the consistence of this technology in different cell types and provide a powerful in vivo visualization for kinase activity and dynamics.

In our experiment, the cell used is genetically modified MCF10A mammary epithelial cell. Unlike neurons and muscle cells, epithelial cells are non-electrogenic cells and cannot be excited by physiological electricity. Epithelial cells may thus give a pure and fundamental cellular response, which would reveal the direct interaction between signaling pathways and EF stimulations instead of triggering electrogenic ion channels and causing related cellular response. The utilized cell line stably expresses ERKTR, and EKAR3 is generated by retroviral infection or transfection via the method described in Sparta's paper [79]. When the EGFR-Ras-ERK signaling pathway is activated, the mCherry-labeled ERKTR will be phosphorylated and transported from the nucleus to the cytosol, resulting in a decrease in fluorescence intensity in the nucleus while that in the cytosol will increase. For a quantitative analysis of the ERK activation in a single cell with a high temporal resolution, the ratio of fluorescence intensity in the cytosol (F_c) to

that in the nucleus (F_n), or the ERKTR ratio, is calculated and used. Thus, the ERKTR ratio will increase when the ERK activation grow stronger, and vice versa.

Those cells were cultured in a flask with MCF10A culture medium consisting of Dulbecco's modified Eagle's medium (DMEM)/F-12, supplemented with 5% horse serum, 20 ng/mL EGF, 10 mg/mL insulin, 0.5 mg/mL hydrocortisone, 100 ng/mL cholera toxin, 50 U/mL penicillin and 50 mg/mL streptomycin. To transfer the cells to the assembled device for experiments, the cells are detached, harvested and then plated on the assembled device, which is coated with FNC coating (Athena, NC9971265) to improve adhesion between the cells and chip surface. After 1 day of culturing in the assembled device, the cell culture medium is replaced by a low fluorescence medium consisting of DMEM/F12 without phenol red, supplemented with 0.5 mg/mL hydrocortisone, 100 ng/mL cholera toxin, 50 U/mL penicillin and 50 mg/mL streptomycin. The cell would be starved for 2 h before the EF stimulation experiment starts.

2.7.1.3. Microelectrode Array Chip Characterization

As mentioned previously, one of the major issues with the conventional EF stimulation setup is the EF-induced chemical signals during the experiments. HfO_2 coating is the solution we used to prevent the Faradaic current. To understand the difference between the device with and without HfO_2 coating, an impedance analysis is helpful to understand the status of the HfO_2 insulating layer.

Based on the recipe of the culture medium, the culture medium conductivity is

$$\kappa = \sum \Lambda_i \cdot c_i = 13.92 \times \frac{10^{-1}\, S}{m} = 1.392\, S/m \tag{24}$$

where Λ_i and c_i are the molar conductivity and the concentration of ion *i* in the medium, respectively. Thus, a simple estimation of the culture medium resistance between two microelectrodes is

$$R_{sol} = \frac{d}{\kappa A} = \frac{200um}{1.392S/m \times 0.0275mm^2} = 5.2\ k\Omega \tag{25}$$

where *d* is the distance between two electrodes.

For the microelectrodes without HfO_2 coating, the impedance between two microelectrodes includes the impedance of the culture medium and the electrical double layer (EDL). Based on the culture medium ingredients, its ionic strength *I* is given by

$$I = \frac{1}{2}\sum_{i=1}^{n} Z_i^2 n_i = 0.19\ M \tag{26}$$

where Z_i and n_i are the charge and the molar concentration of the ion species *i,* respectively. Based on the Gouy-Chapman theory, the Debye length is given by

$$d = \left(\frac{\varepsilon kT}{2Ie^2 N_A}\right)^{1/2} = \frac{0.304}{\sqrt{0.19}} = 0.697\ nm \tag{27}$$

where *k* is the Boltzmann constant, *T* is the absolute temperature, *e* is the unit charge, ε is the permittivity of the solvent and N_A is Avogadro number. Then the capacitance of the EDL at the interface between culture medium and Au microelectrode is

$$C_{EDL} = \frac{\varepsilon A}{d} = 27\ nF \tag{28}$$

where A is the area of the microelectrode and ε is the permittivity of the culture medium. Thus, the impedance of the EDL at the interface between the culture medium and the Au microelectrode at 50 kHz is hence as follows:

$$Z_{EDL} = \frac{1}{j\omega C_{EDL}} = \frac{1}{j} 118\ k\Omega \tag{29}$$

Therefore, the impedance between two Au microelectrodes without HfO_2 coating is

$$Z_{without\ HfO2} = R_{sol} + 2 \times Z_{EDL} = 5.2 + \frac{1}{j} 0.236\ k\Omega \tag{30}$$

For the HfO_2 coating layer, the ALD HfO_2 has a dielectric constant around 18. The capacitance of a 10 nm thick ALD HfO_2 layer on top of the Au microelectrode is thus

$$\begin{aligned} C_{HfO2} = \frac{\varepsilon_r \varepsilon_0 A}{t} &= \frac{18 \times 8.854 \times 10^{-12}\ F/m \times 0.0275\ mm^2}{10\ nm} \\ &= 0.4384 \times 10^{-9}\ F \end{aligned} \tag{31}$$

where A is the area of the electrode, ε_r is the relative permittivity of ALD HfO_2, ε_0 is the permittivity of the vacuum and t is the thickness of the ALD HfO_2. The impedance of the 10-nm thick ALD HfO_2 at 50 kHz is therefore

$$Z_{HfO2} = \frac{1}{j\omega C_{HfO2}} = \frac{1}{j} 7260\ \Omega = \frac{1}{j} 7.3\ k\Omega \tag{32}$$

where $\omega = 2\pi f$, f is the AC signal frequency.

The total impedance between two Au microelectrodes with a 10-nm HfO_2 coating is hence

$$Z_{with\ HfO2} = R_{sol} + 2 \times Z_{EDL} + 2 \times Z_{HfO2} = 5.2 + \frac{1}{j} 14.84\ k\Omega \tag{33}$$

Based on these calculations, the capacitive impedance of the HfO_2 layer at 50 kHz is comparable to the resistance of the medium between two electrodes.

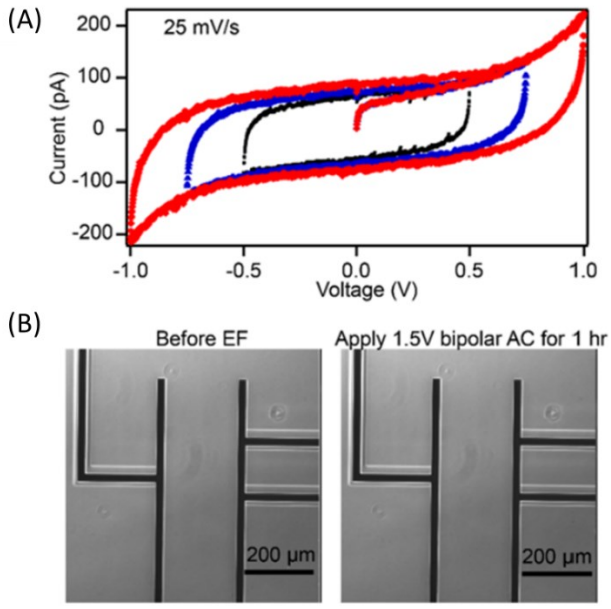

Figure 2.7.5. Microelectrode array chip stability test. (A) Cyclic voltammetry (CV) scan of Au microelectrode array in the culture medium DMEM/F-12. The parallel microelectrode pair are used as the working and counter electrodes, and the scan rate is 25 mV/s. There is no significant redox current during the scan. (B) Optical images of the Au microelectrode pair before and after the continuous application of a bipolar 10-µs width, ±1.5-V AC EF stimulation for more than one hour. There is no visual damage on the exposed Au microelectrodes, demonstrating the stability of the microelectrode array in the culture medium.

Instead of DC EF signals, bipolar symmetrical electric pulses are used to stimulate cells, avoiding the net DC ionic flows in the system. As mentioned previously, the small exposed microelectrode surface allows EF signals to couple with the culture medium capacitively through a high-pass filter with an impedance around 120 Ω at 50 kHz. Cyclic voltammetry (CV) scans of the fabricated device chip are performed and shows no redox current between -1.0 and 1.0 V at a slow scan rate of 25 mV/s, shown as Figure 2.7.5A. With an increase in bipolar pulses stimulation at ±1.5 V for more than one hour, there is no visual degradation or damage on the exposed parallel microelectrodes,

proving a high stability of the microelectrode array in the culture medium, as depicted in Figure 2.7.5B.

In addition, the computer simulation (COMSOL Multiphysics) of the EF distribution in the culture medium is demonstrated (Figure 2.7.6). The microelectrode array on the device chip is simplified as two parallel Au microelectrodes on top of a 1200 μm × 1200 μm × 10 μm (L × W × H) silicon dioxide substrate. The dimension of each microelectrode is 100 μm × 10 μm × 50 nm (L × W × H) and the gap distance between these two microelectrodes is 200 μm. The whole model is set in an aqueous solution, which has a dielectric constant of 78. When an AC EF signal (1 V, 50 kHz) is applied between the Au microelectrode pair in a homogenous medium, the field strength will change with the distance between the target position and the exposed microelectrode edge. The field strength is close to 24 V/cm near the microelectrode edge and it decreases to approximately 8 V/cm on the substrate surface at the center between the microelectrode pair.

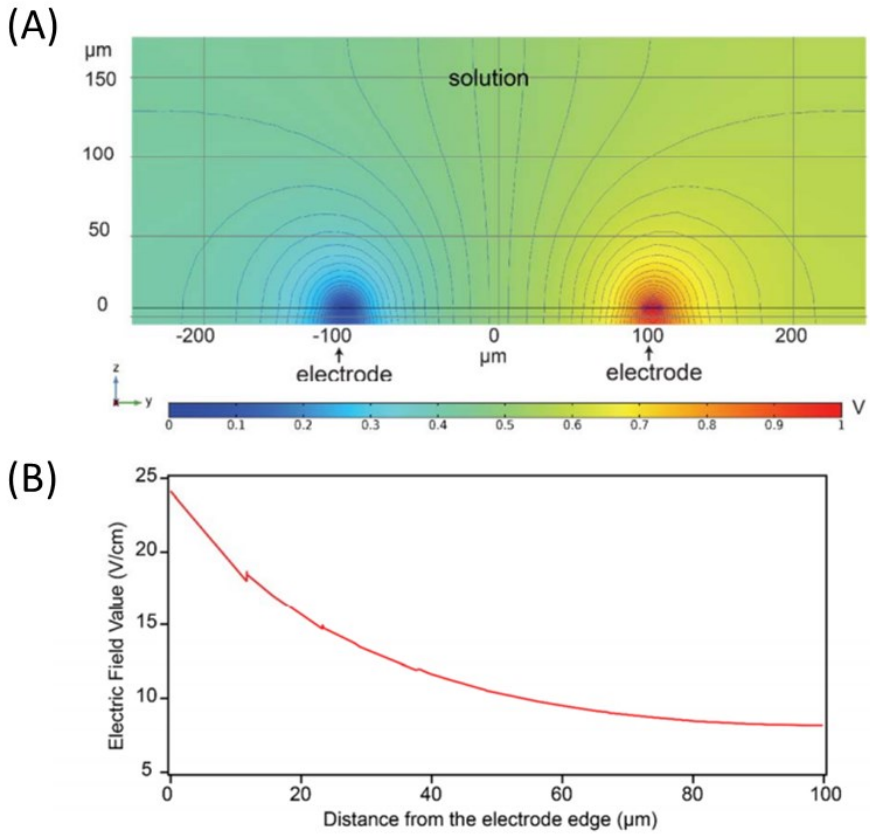

Figure 2.7.6. The computer simulation of the AC EF strength distribution between a parallel microelectrode pair. (A) Simulation of the electric potential distribution at a cross section of the microelectrode pair. The microelectrode at -100 μm is grounded and the one at 100 μm is connected to an AC voltage with an amplitude of 1 V and a frequency of 50 kHz. The equal potential line distribution shows a high density close to the microelectrodes, and it gradually decreases with the distance from the microelectrode edge. (B) Simulation of the field strength along the line between the two centers of the microelectrodes on the substrate surface. The nominal field strength is about 24 V/cm near the microelectrode edge and decreases to roughly 8 V/cm 100 μm away from the microelectrode.

2.7.2. ERK Activation Tests with the Assembled Device

The assembled device creates a thin fluidic channel (W × L × H: 0.5 cm × 1 cm × 170 μm), which provides an ideal optical access with a low background from the culture medium and confines the EF distribution. This assembled chip is placed on the automated stage of an optical microscope, which includes an automated filter turret and an

environmental control chamber. MCF10A cells are transferred to and cultured in the thin channel of the assembled device before the EF stimulation experiments. To reduce the background fluorescence noise, cells are starved for 2h in a low fluorescence culture medium right before the stimulation. During the experiment, the temperature and carbon dioxide concentration are automatically maintained at 37 ℃ and 5%, respectively, in the environmental chamber. The AC EF stimulation signal used is a 50-kHz bipolar square wave, which is designed and delivered by a compactRIO controller that is controlled by a customized LabVIEW program.

During the stimulation, the ERKTR will be transported from the nucleus to the cytosol when the EGFR-Ras-ERK signaling pathway is successfully activated. This process will increase the fluorescence intensity in the cytosol and decrease that in the nucleus and the fluorescence intensity can be analyzed quantitatively in real-time observation. In the following section, I introduce the experiment results of modulated ERK activation via AC EF stimulation.

2.7.2.1. Localized Activation of ERK via AC EF Modulation

The fluorescence intensity of the nucleus typically starts to decrease, and that in the cytosol increases roughly 3-6 min after the AC EF stimulation, indicating that the EGFR-Ras-ERK signaling pathway is activated. At the same time, this ERK activation shows a location dependence related to the microelectrodes. Figure 2.7.7A depicts a fluorescence image 9 min after AC EF stimulation. Cells close to the microelectrode display a clear ERK activation after 9 min of stimulation (Figure 2.7.7B), while cells more than 200 μm away from the exposed microelectrode have no significant change in fluorescence intensity. Note that some cells close to microelectrodes remaining silent in

Figure 2.7.7C because the SU8 passivation layer on the microelectrodes works as an insulation for AC EF signals.

Based on the fact that MCF10A cells stably express EKAR3 in the nucleus and ERKTR, a Matlab (Mathworks) program identifies the nuclei using the yellow channel fluorescence of EKAR3 and the cytosol region is defined by the neighboring seven pixels outside the nucleus. The average red fluorescence intensity of ERKTR in the nucleus and that in the cytosol are calculated. The ERKTR ratio, which is the ratio of the average fluorescence intensity in the cytosol (F_c) and that in the nucleus (F_n), is used to quantify the ERK activation.

A comparison of the ERKTR ratio changes of cells located within 100 μm of the microelectrode during the stimulation reveals a synchronized ERK activation initialization with heterogeneous dynamics in these cells (Figure 2.7.7D). Before the AC EF application, only a limited number of cells display limited low-level spontaneous ERK activity. At about nine minutes after the stimulation, cells begin to demonstrate ERK activations with different amplitudes and durations. Most of the cells in this region respond between 6 min and 18 min after the stimulation. In this experiment, the AC EF stimulation is continuous, and the ERK activation level of most cells decreases after the first ERK activation and eventually reaches a higher baseline in 29 ± 13 min. In comparison, cells between 200 μm and 700 μm away from the exposed microelectrode show no ERK activation during the continuous EF stimulation.

After investigating the distribution of cells that exhibit clear ERK activation in the continuous AC EF stimulation, more than 80% of these cells appear to be located within 50 μm of the exposed microelectrodes (Figure 2.7.8). When the distance increases to

more than 100 μm from the exposed microelectrodes, the number of ERK-activated cells drops rapidly.

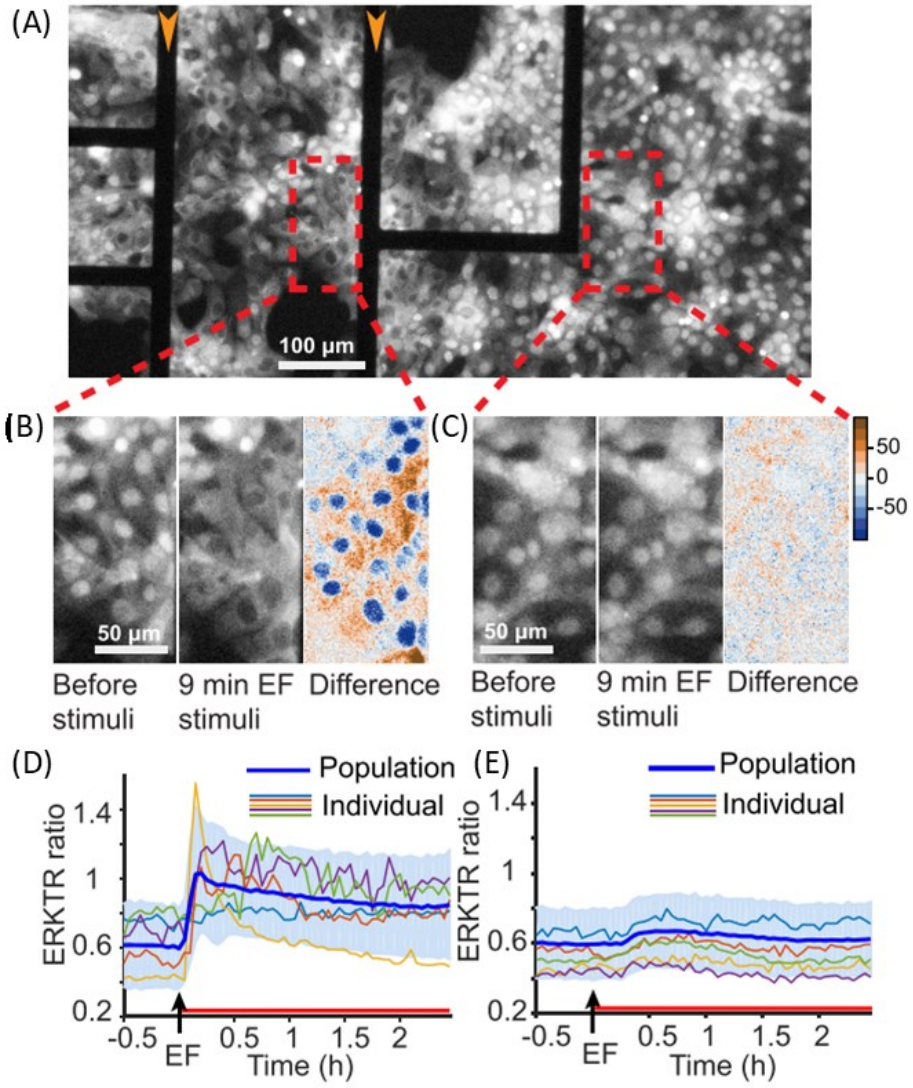

Figure 2.7.7. Localized ERK activation via AC EF stimulation. (A) A fluorescence image of one pair of microelectrodes during the AC EF stimulation. The orange arrow heads represent the exposed microelectrodes. (B, C) The comparison of cells at region (B) within 100 μm of the exposed microelectrode and (C) w between 200 μm to 300 μm away from the exposed microelectrode. The left and center panels of (B, C) show fluorescence images before and at 9 min after AC stimulation. The right panel of each image shows the difference in fluorescence intensity after and before the stimulation. The blue area indicates the intensity decrease while the orange indicates the intensity increase. (D) The time traces

of the ERKTR ratio of individual representative cells and the population average from 164 cells in the region within 100 µm from the exposed microelectrode. The average data is presented as mean (thick blue line) ± standard deviation (light shadow). The black arrow marks the start time of AC EF stimulation and the red line indicates the continuous AC EF stimulation. (E) The time traces of the ERKTR ratio of individual representative cells and the population average from 160 cells in the region ranging between 200 µm and 700 µm away from the exposed microelectrode. The average data is presented as mean (thick blue line) ± standard deviation (light shadow). The black arrow marks the start time of AC EF stimulation and the red line indicates the continuous AC EF stimulation.

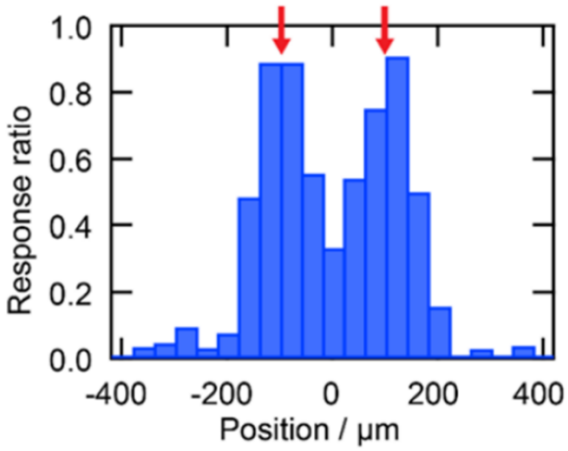

Figure 2.7.8. The distribution of cells that show clear ERK activation during the continuous AC EF stimulation. The x-axis is defined to be perpendicular to the exposed microelectrode pair in the fluorescence image. The origin of the x-axis is the center point between the two exposed microelectrodes and cell positions are the projection on the defined x-axis. The exposed microelectrode positions are denoted by the red arrows.

Previous experiments [79] have demonstrated an oscillatory pattern of ERK activation during a continuous chemical stimulation. A similar oscillatory pattern is discovered in a few cells in the continuous AC EF stimulation. A Matlab program is used to identify the peaks and valleys of the ERKTR ratio recordings, revealing that approximately 20% of cells during the continuous AC EF stimulation have multiple ERK activation cycles, as shown in Figure 2.7.9.

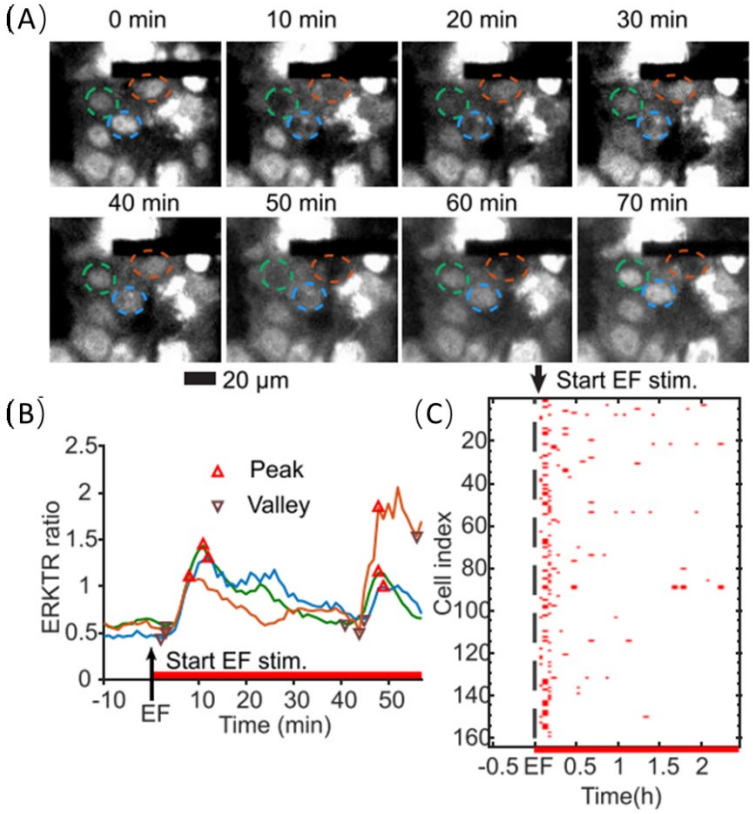

Figure 2.7.9. Oscillatory pattern of ERK activation during a continuous AC EF stimulation. (A) Key frames of the time lapse recording of three cells show an oscillatory pattern of ERK activation during the continuous AC EF stimulation. The cells in the orange, blue and green circles exhibit multiple cycles of ERK activation and relaxation. (B) The ERKTR ratio recordings of the three cells circled in (A). Two cycles of the ERKTR ratio are identified with peaks and valleys on the trace. The black arrow and the red line denote the start time and the duration of the continuous AC EF stimulation, respectively. (C) The heat map of the peak time during the time lapse recording of 164 cells in the region of Figure 2.7.14B. There are 35 cells demonstrate multiple ERK activation cycles during the 3-h continuous AC EF stimulation. The black arrow and the red line denote the start time and the duration of the continuous AC EF stimulation, respectively.

2.7.2.2. Precisely Synchronized Activation of ERK via AC EF Modulation.

Continuous AC EF stimulation at 50 kHz has shown a localized ERK activation based on previous sections. Whether AC EF stimulation can be used for controlling the

ERK activation on the designed timing is the next interesting question. In order to demonstrate the feasibility, we use a 3-min train of bipolar pulse to trigger the synchronized ERK activation in a temporal manner, and the result suggests a reproducible, synchronized, and enhanced ERK activation. Compared to the continuous AC EF stimulation, one stimulation cycle starts with a 3-min train of 1-V 50-kHz AC signal and the microelectrode then remains silent for approximately 40 minutes (Figure 2.7.10). This cycle is repeated three times during the AC stimulation. During the stimulation, three ERK activation events are observed at about three to six minutes after the pulsed AC signal application and cells restore to a low ERK activity level within an average time of 15 ± 6 min (Figure 2.7.11). Interestingly, the number of cells that display ERK stimulations increases from the first to the third cycle. About 50% of cells within 100 μm of the microelectrode show ERK activation in all three cycles, and roughly 30% more cells start ERK activation in the second or third cycle. Moreover, the later stimulation will trigger ERK activation in a temporal synchronized manner. Multiple tests demonstrated that when the pulsed AC signal is shorter than 3 min, the number of cells that demonstrate ERK activation is reduced and the activation is less reproducible. Based on this result, precisely synchronizing the ERK activation via a pulsed and localized AC EF signal is feasible.

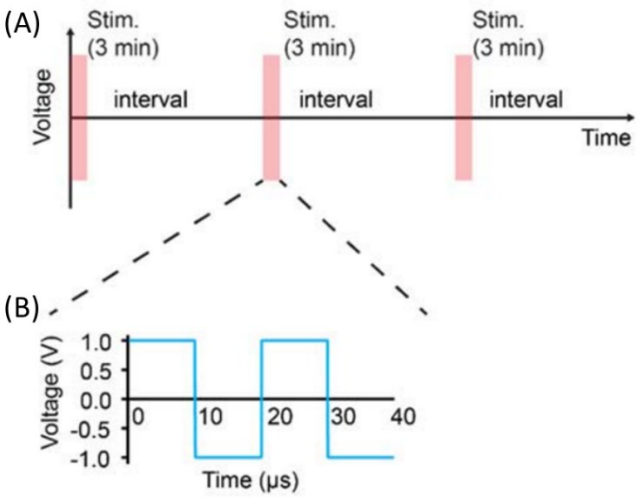

Figure 2.7.10. The schematics of the pulsed AC stimulation signal. (A) The complete AC stimulation signal, which includes three cycles consisting of a 3-min AC stimulation and a 40-min interval silent period. (B) A zoom-in on the AC signal in the 3-min AC stimulation. This 3 min stimulation is a train of bipolar square waves with an amplitude of 1.0 V and a frequency of 50 kHz.

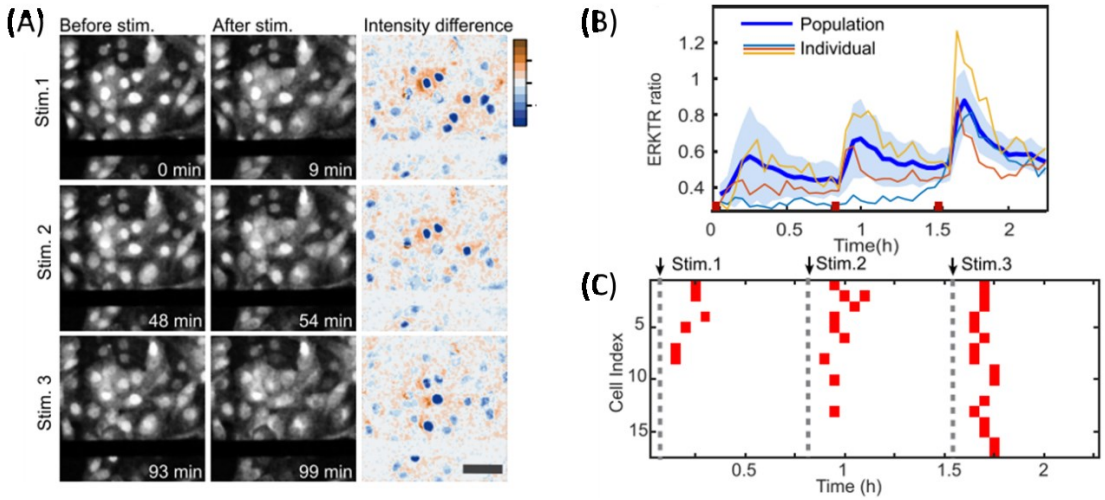

Figure 2.7.11. Precisely synchronized ERK activation with pulsed AC EF stimulation. (A) Fluorescence images of cells before (left) and after (middle) each stimulation. The stimulations start at 0 min, 48 min, and 93 min, and each one lasts for 3 min. The right panel illustrates the ERKTR fluorescence intensity changes before and after the stimulation. The orange and blue colors denote the fluorescence intensity increase and decrease, respectively. Scale bar: 50 μm. (B) the ERKTR ratio recordings of individual representative cells and the population average of 17 cells. The red line shows the duration of each AC stimulation. Data are presented as mean (blue line) ± standard deviation (light

blue shadow). (C) The time map of ERKTR peaks. The black arrows denote the timing of each AC stimulation.

2.7.3. Control Tests of Membrane Integrity, Cell Viability, Electrochemical Reactions and Temperature

In order to understand the underlying mechanism of the ERK modulation under AC EF stimulation, control tests are demonstrated to prove our device would not trigger ERK activation because of cell damage and chemical changes induced by EF stimulation. As mentioned previously, conventional AC EF stimulation is normally used for electroporation and radiofrequency ablation, which would change the cell membrane permeability or damage the cells via their thermal effect. At the same time, conventional EF stimulation would introduce Faradaic processes, resulting in possible Ca^{2+} or ROS changes during the stimulation. To demonstrate the safety and purity of our experiment setup, three control tests are performed.

The first control test performed is the membrane integrity test. To test the membrane integrity during a long term AC EF stimulation, cell-impermeant nucleic acid stain is used. SYTOX® Orange nucleic acid stain is a fluorescence stain that has a high affinity to nucleic acid. After binding with nucleic acid, the stain would emit 570 nm light when it is excited with a 520–550 nm light source. This molecule would easily penetrate cells with a compromised cell membrane; however, it will not cross the intact cell membrane of live cells. The fluorescence intensity of this molecule will increase by more than 500 times when it binds with nucleic acid, thereby providing a clear distinction from background noise. This property makes SYTOX® Orange a good candidate as a simple and quantitative one-step indicator of distinguishing dead cells.

The cell membrane integrity test is performed after plating MCF10A cells in our assembled device. Before the 1.5-V AC EF continuous stimulation, 50 µM SYTOX® Orange (Invitrogen) is added into the culture medium, and the total time of the stimulation is more than one hour. Comparing the fluorescence images before and after the simulation, there are only a couple of cells that show fluorescence signal after the stimulation, demonstrating that the cell membrane integrity is intact after a long term stimulation in our experiment setup (Figure 2.7.12).

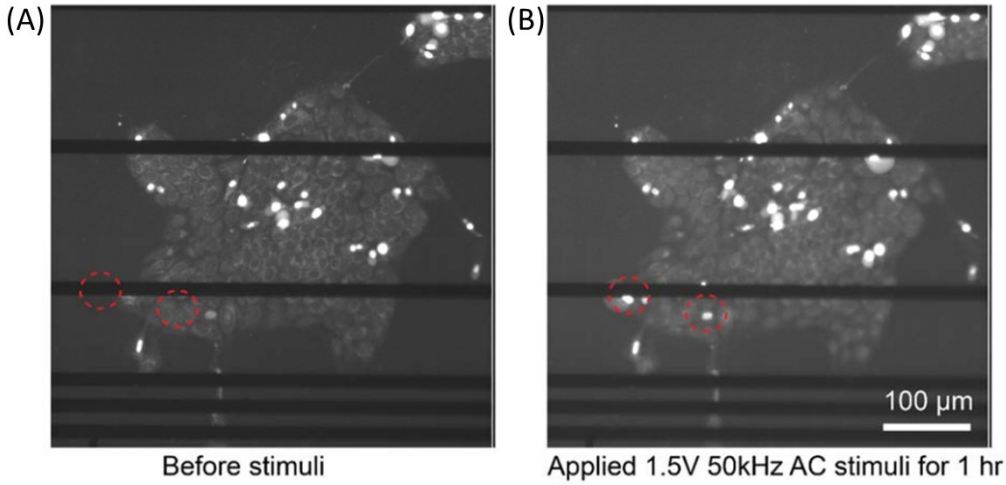

Figure 2.7.12. The cell membrane integrity test. Before the stimulation, 50 µM cell-impermeant fluorescence stain SYTOX® Orange is added to the culture medium. Time lapse images are taken during the 1 h of 1.5-V 50-kHz AC EF stimulation. (A) The fluorescence image before the AC EF stimulation is applied. (B) The fluorescence image after 1 h of AC EF stimulation. The black bars in the image are the exposed microelectrodes. The bright dots in the cell cluster are the stained cells with a broken membrane. The red dash circles indicate the cells that display membrane integrity changes during the AC EF stimulation. Only a few cells exhibit membrane permeability changes during the experiment.

The second control test concerns the cell viability and the proliferation rate during and after the stimulation test. The possibility exists that the EF-induced ERK activation

may be the result of cell apoptosis triggered by the stimulation. Ruling out this possibility is also important.

The ReadyProbe® Cell Viability Imaging Kit (Cat#R37609, Life Technologies) is used for the cell viability test. Two room temperature, stable reagents are available in this regard: NucBlue® Live reagent stains the nucleus of all living cells and can be detected with a standard DAPI (blue) filter, and NucGreen® Dead reagent stains the nucleus of the cells that have compromised plasma membrane integrity and can be detected using a standard FITC/GFP (green) filter.

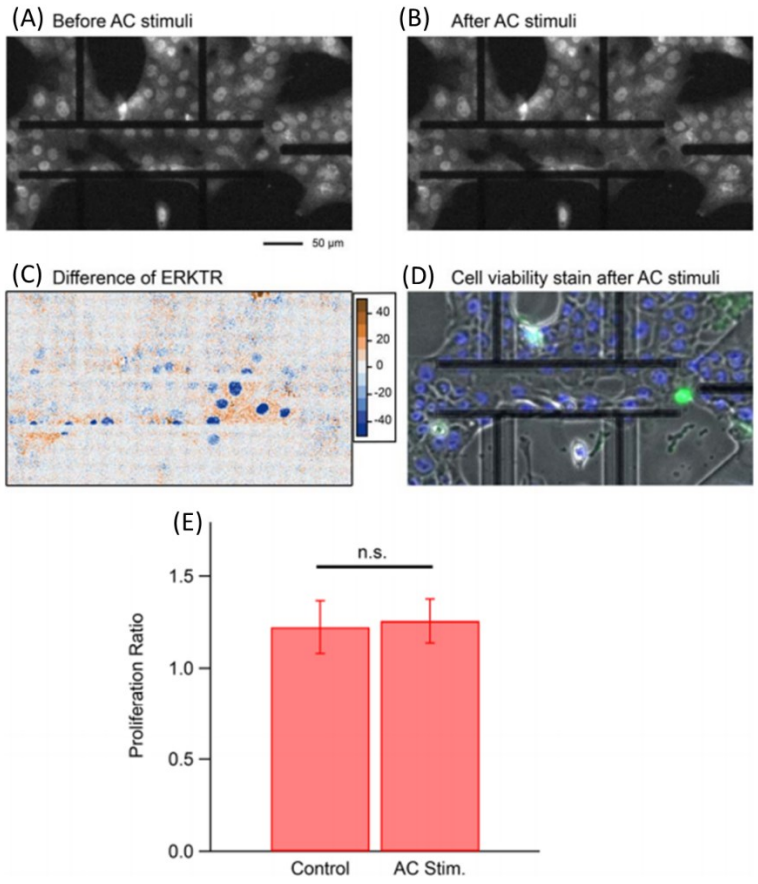

Figure 2.7.13. The cell viability and cell proliferation rate test. (A-D) display the cell viability test with fluorescence staining. (A) The fluorescence image of cells before the AC

EF stimulation. (B) The fluorescence images of cells after the AC EF stimulation. (C) The color-coded map of the fluorescence intensity changes between image (B) and (A). The orange color indicates the ERKTR fluorescence intensity increase and the blue color indicates the ERKTR fluorescence intensity drop. (D) A combined image of the phase contrast and fluorescence imaging result after 2 h of AC EF stimulation. The blue staining shows the live cells and the green stain labels the dead cells. (E) The cell proliferation rate of cell groups in the AC stimulation region and the control region. There is no significant difference between these two groups of cells. $p > 0.05$ (n=4).

Fifteen minutes before the AC EF stimulation test, two drops of each reagent are added to the culture medium in the assembled device with plated MCF10A cells. AC stimulation regions are selected to be the area within 150 μm from the exposed microelectrodes. Control regions are areas more than 200 μm away from the exposed microelectrode, where no ERK activation is normally observed in series tests. The total cell number is counted before the first AC EF stimulation on Day 1, and these activated cells are put back into the incubator for 24 h culture. On Day 2, the AC EF stimulation is applied on the same areas in the assembled device, and the cell number is also counted. The second AC EF stimulation confirms the reproducible ERK activation on the same group of cells and the stain result shows that more than 95% of cells remain alive and healthy after the experiment. The total cell number counted at the first and second AC EF stimulations actually indicates that the cell proliferation rate of the EF-induced ERK activated cells is 1.26 ± 0.11, with no significant difference from the cell proliferation rate of the cells in the control regions. The cell proliferation rate result is calculated based on four sets of ratios from two independent stimulation experiments (Figure 2.7.13).

The third control test aims to exclude electrochemical reactions interfering with the ERK activation. Conventional stimulations use DC voltage, which may introduce net ion flows during the experiment. The solution we propose is to add a high-k passivation

layer, which is an HfO_2 ALD layer, as mentioned previously, on the surface of the exposed microelectrodes. Since AC EF stimulation is applied in our device, the HfO_2 ALD layer will block redox reactions and would not significantly increase the impedance of the exposed microelectrode, which is proved by the theoretical calculation in the previous section (Figure 2.7.14). Different thicknesses of HfO_2 coating were tested in our experiments, and a 10-nm HfO_2 layer is chosen for our stimulation system. The CV test confirms that there is no Faradaic process detected when the exposed microelectrodes are not coated by HfO_2. Compared to the bare Au microelectrodes, HfO_2-coated microelectrodes can still activate the ERK signaling pathway with a higher AC voltage, which ranges from 1.5 V to 3 V based on the experiment results. This is understandable due to the increase in the total impedance on the microelectrode surface. The HfO_2-coated microelectrode thus prohibits the electrochemical reaction and related pH changes in the local environment.

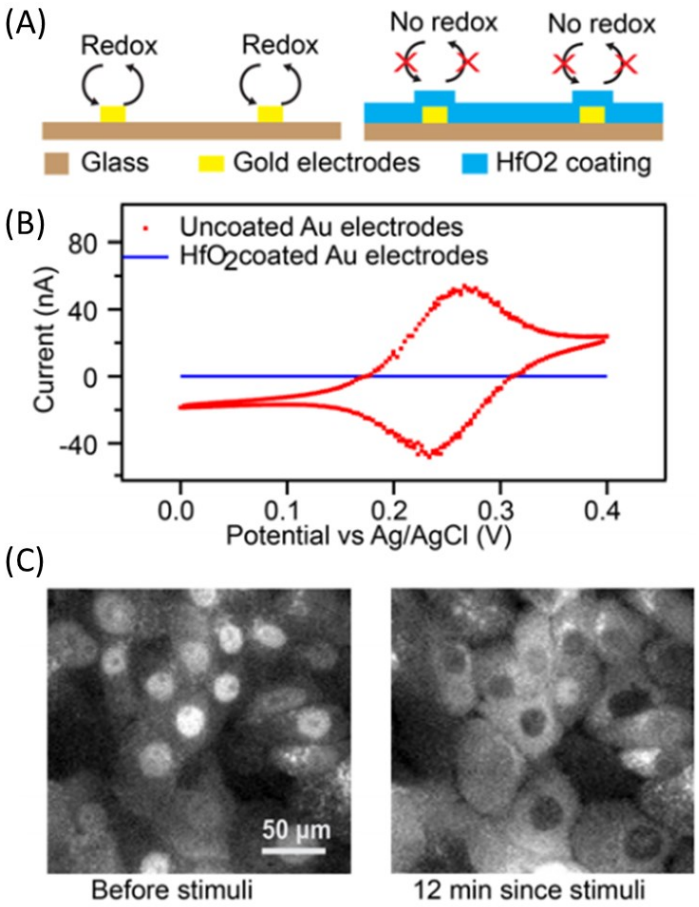

Figure 2.7.14. Cyclic voltammetry (CV) scan and ERK activation on HfO_2-coated microelectrodes. (A) A schematic illustration of redox reactions during stimulation. Left panel: Redox reactions would occur on the surface of bare metal microelectrodes. Right panel: the high-k HfO_2 insulating coating on the microelectrode surface will suppress the redox reactions. (B) CV scan of exposed microelectrodes in 5 mM solution of ferrocyanide and ferricyanide with 0.1 M KCl supporting electrolyte with a three electrode configuration with a scan rate of 50 mV/s. An Ag/AgCl agar gel salt bridge reference electrode is used as the reference electrode, a Pt wire as the counter electrode and the exposed microelectrode as the working electrode. The red dot indicates the current of the bare Au microelectrode, which shows significant peaks of redox and oxidation process. The blue line denotes the current of the microelectrode with HfO_2 coating, showing a complete suppression of the redox process. (C) Fluorescence image of ERK signaling pathway activation with HfO_2-coated microelectrodes via AC EF stimulation.

In addition, control tests with Ca^{2+} chelator (BAPTA AM, 3 µM, Life Technologies) and ROS quencher (Trolox, 350 µM, Sigma-Aldrich) were performed to

prove that the ERK activation is not a result of EF-induced Ca^{2+} flux or ROS (Figure 2.7.15). In the stimulation with these reagents, ERK activation can still be triggered reproducibly by AC EF stimulation, suggesting that AC EF simulation is not associated with the redox process, Ca^{2+} and ROS, which indicates that the coupling mechanism is different with DC EF stimulation tests.

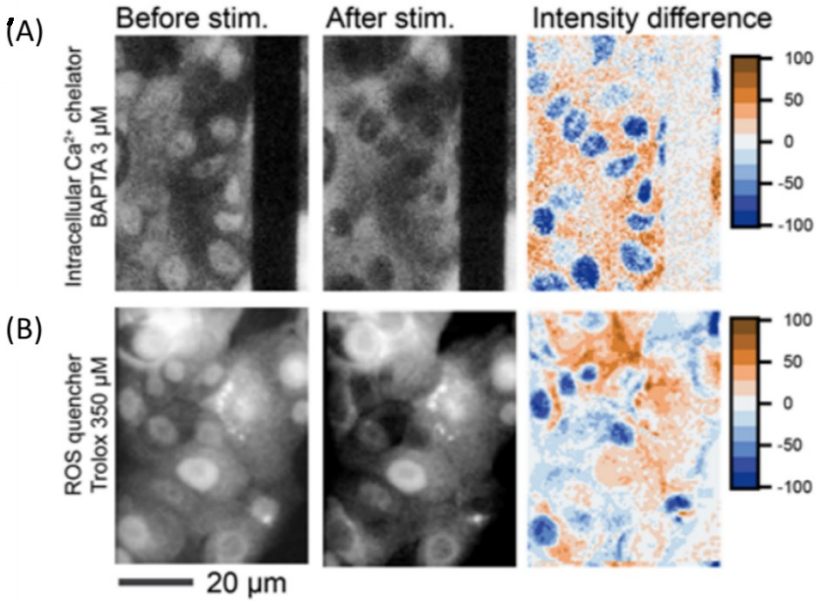

Figure 2.7.15. ERK activation control tests with intracellular Ca^{2+} chelator and ROS quencher. The AC EF stimulation can still trigger ERK activation when (A) the Ca2+ chelator BAPTA AM presents at 3µM in the culture medium and (B) the ROS quencher Trolox presents at 350 µM.

The fourth control test is related to the possible temperature or diffusion limited changes occurring in the thin channel. The local temperature near microelectrodes is tracked by the current of a patch clamp pipette electrode based on the method provided in Yao's paper [82]. The patch clamp pipette is prepared from a commercial borosilicate capillary glass tube by a micropipette puller (P-1000, Sutter Instrument). This pipette is

filled with 0.1 M KCl and has a typical resistance of 7 MΩ to 10 MΩ. In order to measure the temperature, the pipette is mounted on a patch clamp amplifier through an Ag/AgCl reference electrode and positioned 10 μm above the device chip surface, at the middle between two parallel microelectrodes in the culture medium. Another Ag/AgCl reference electrode filled with 0.1 M KCl is connected to the medium in the chamber. Then, a 10-mV bias is applied to the pipette and current readout is recorded at a sampling rate of 20 kHz. If the temperature near the microelectrode increase during the AC EF stimulation, then the ion mobility would increase, resulting in a higher conductivity. Furthermore, given the small size of the pipette tip, the conductivity changes will generate sensitive changes in current. As the room temperature in our lab is regulated at 21.6 ± 0.2℃, the temperature can be calculated as follows:

$$T = \frac{1}{\frac{1}{T_0} - \frac{R}{E_a}\ln(\frac{I}{I_0})} \tag{34}$$

where R is the gas constant of 8.31 $J \cdot mol^{-1} \cdot K^{-1}$, T_0 is the room temperature, I is the pipette current measured at temperature T, and I_0 is the pipette current at temperature T_0. Moreover, E_a is the nominal activation energy estimated by Yao: 16.07 kJ/mol [82].

Ten measurements are conducted for both 3-min and 10-min AC EF stimulation each. The first 10 min of current recordings in each stimulation is used for data calibration, and 60-sec recordings immediately before and after the AC EF stimulation are used for the temperature calculation. For the bare Au microelectrode, the temperature changes during the 3-min and 10-min AC stimulations are 0.00 ± 0.05 ℃ and 0.01 ± 0.07 ℃, respectively. For the HfO_2 coated microelectrode, the temperature changes during 3-min and 10-min AC stimulations are 0.03 ± 0.07 ℃ and 0.01 ± 0.05 ℃,

respectively. Thus, there are no obvious local temperature changes near the microelectrode during the AC EF stimulations (Figure 2.7.16). At the same time, the spontaneous ERK activation ranging from 35 ℃ to 39 ℃ is evaluated. The MCF10A cells between 35 ℃ to 37 ℃ exhibit active ERK activities and the spontaneous ERK activities would significantly reduce when the temperature is above 37 ℃ (Figure 2.7.17). Therefore, the allowed temperature range of ERK activation is much larger than the local temperature change and will not affect the observed ERK activation.

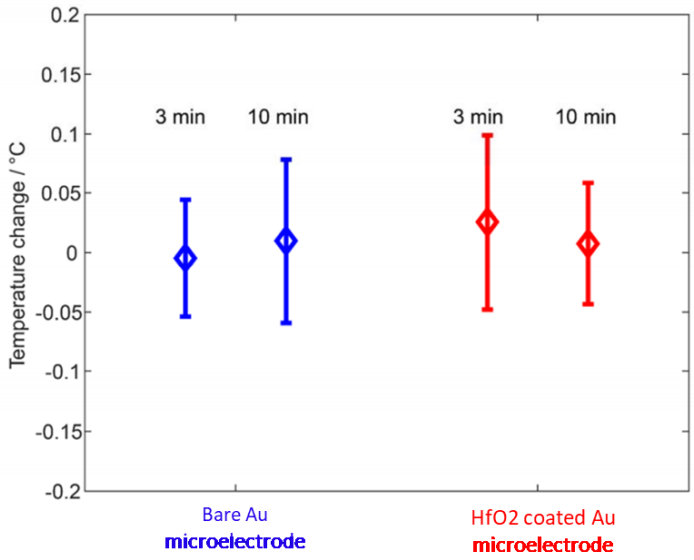

Figure 2.7.16. Local temperature changes before and after AC EF stimulations on different types of microelectrodes. The room temperature is measured to be 21.6 ± 0.2℃. The patch clamp pipette used for measurement is placed at the middle point between one pair of microelectrodes. The AC signal applied on the bare Au microelectrode is a 1-V 50-kHz square wave, and that on HfO_2 coated Au microelectrode is a 6-V 50-kHz square wave. For each result, 10 groups of measurements are done for 3-min and 10-min AC EF stimulations.

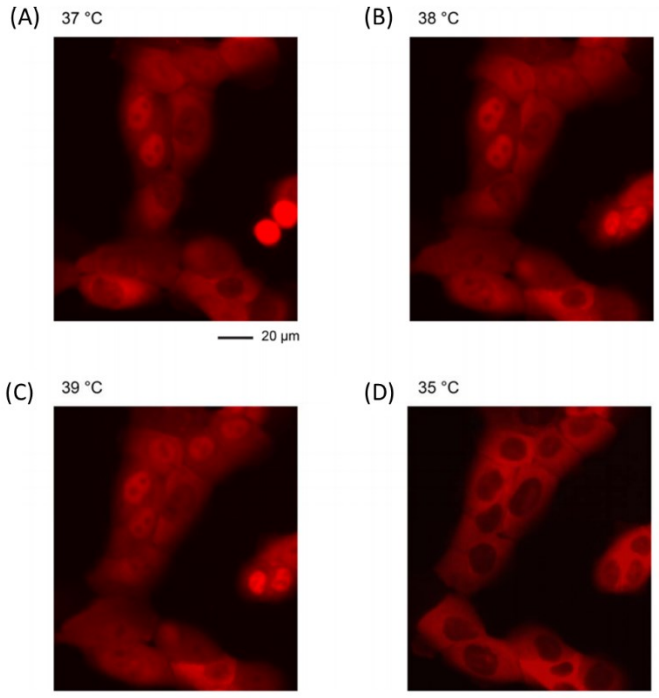

Figure 2.7.17. The fluorescence image of spontaneous ERK activity at (A) 37 ℃, (B) incubation at 38 ℃ for 10 min, (C) incubation at 39 ℃ for 10 min, and (D) incubation at 35 ℃ for 10 min.

In addition, the relation between the ERK response onset time of cells one the one hand and the distance between cell locations and the exposed microelectrode on the order is investigated. Although a wide range of ERK onset time of different cells exists—spanning from 6 min to 36 min—more than 79% of 216 cells with ERK activation exhibit a response within 15 min after the application stimulation regardless of the cell locations (Figure 2.7.18). Furthermore, all cells that response after 18 min of stimulation are randomly located 25 µm away from the exposed microelectrodes. This may be the result of either spontaneous ERK activity or a diffusion related process, such as intercellular communications. If the localized heating changes triggers the ERK activation, then the ERK activation onset time would have a position dependent relation because of the heat

transferring. Compared to the result, the temperature change or heat transfer is not important during AC EF stimulations.

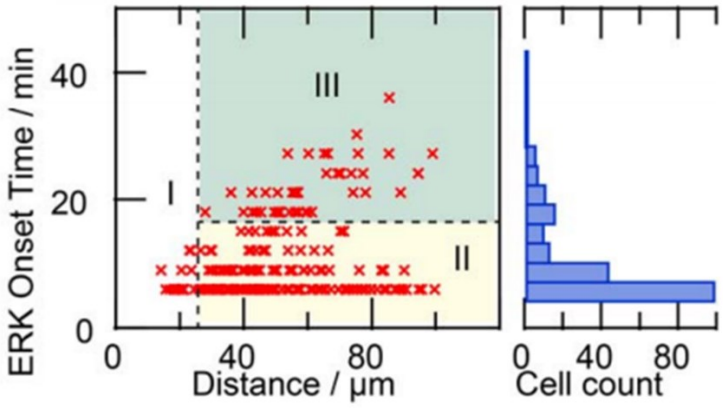

Figure 2.7.18. Left panel: the distribution of the ERK activation onset time and the distance between the cell location and the exposed microelectrode. The 216 cells investigated are located within 100 μm of the microelectrode. Region I: Cells located within 25 μm of the exposed microelectrodes are all activated within 10 min. Region II: About 77% of cells located more than 30 μm away from the exposed microelectrode show a distance-independent short ERK response time, which is shorter than 15 min. Region III: About 23% of the cells located more than 30 μm away from the exposed microelectrode show a longer onset time with a random distribution. Right panel: Histogram of ERK activation onset time.

2.7.4. Inhibitor Test for Determining the Interaction Site between Cellular Response and AC EF Stimulation

Previous experiment results have demonstrated that EF-induced ERK activation is independent of electroporation, pH, ROS, Ca^{2+}, and temperature changes. This leads to a possibility that the AC EF may interact with the EGFR-Ras-ERK signaling pathway directly. In order to identify the possible interaction site of the coupling between AC EF stimulation and the signaling pathway, a series inhibitor test is conducted based on the canonical EGFR-Ras-ERK signaling pathway.

The EGFR signaling pathway is an important pathway in cell growth regulation, survival, proliferation and differentiation in mammary cells. The canonical EGFR-Ras-ERK signaling pathway starts with the binding of EGF and the extracellular domain of its receptor EGFR. Two EGF molecules bind with a pair of EGFRs on the cell membrane, triggering the dimerization, activation of intrinsic kinase activity, and phosphorylation of EGFR. One of the proteins recruited to active EGFRs, growth factor receptor-bound protein 2 (GRB2), binds to the phosphotyrosine residue and recruits Son of Sevenless (SOS), which are a set of genes encoding guanine nucleotide exchange factors that act on the Ras subfamily. SOS activates the guanosine diphosphate (GDP) / guanosine triphosphate (GTP) exchange which recruits Raf to the membrane, and Raf in turn phosphorylates MEK, which will then activates ERK. Thus, we applied different inhibitors targeting the MEK, the Raf, the small molecule tyrosine kinase domain of the EGFR (i.e. ErbB) family, and the EGFR extracellular binding site, as illustrated in Figure 2.7.19. The names and concentrations of the inhibitors used are listed in Table 2.7.1. For each group of tests, cells with corresponding inhibitors are stimulated with AC EF and then with EGF as a comparison. The inhibition of the ERK activation in both cases is observed when MEK inhibitor, Raf inhibitor, and tyrosine kinase inhibitors (TKIs) are applied. However, when the EGFR antibody cetuximab is added, the AC EF stimulation can still activate the ERK while the control group under EGF stimulation shows ERK inhibition (Figure 2.7.20). Although a reduction in fluorescence intensity and a lag in ERK activation are noticed, the result suggests that the interaction between AC EF and EGFR signaling pathway is initialized by an EF-induced and EGF-independent kinase activity of EGFR.

Target	Inhibitor	Concentration
MEK	Trametinib (Selleck Biochemcials)	0.5 μM
Raf	Sorafenib (Biotang)	20 μM
ErbB	Afatinib (Selleck Biochemcials)	5 μM
	Erlotinib (Selleckchem)	2 μM
	Gefitinib (Selleckchem)	50 μM
EGFR extracellular binding site	Cetuximab (ERBITUX)	100 μg / mL

Table 2.7.1. The list of the inhibitor used for the EGFR signaling pathway inhibition test.

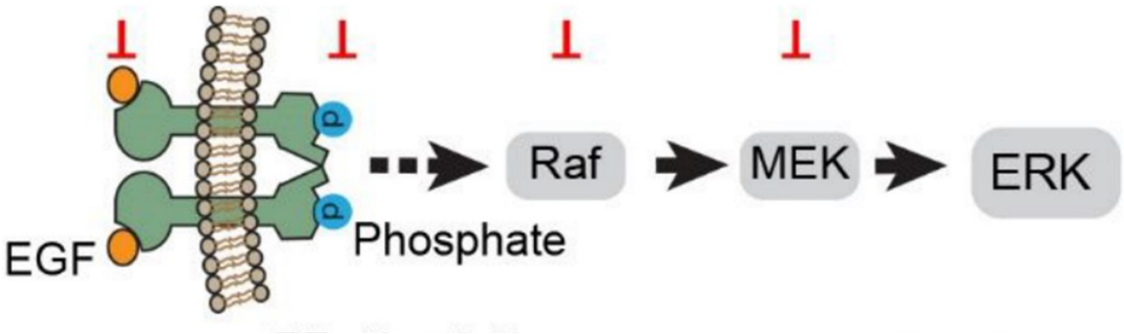

Figure 2.7.19. Schematics of the canonical ERK signaling pathway and the blocked sites, including the extracellular EGF binding site, the intracellular phosphorylation site of EGFR, Raf and MEK.

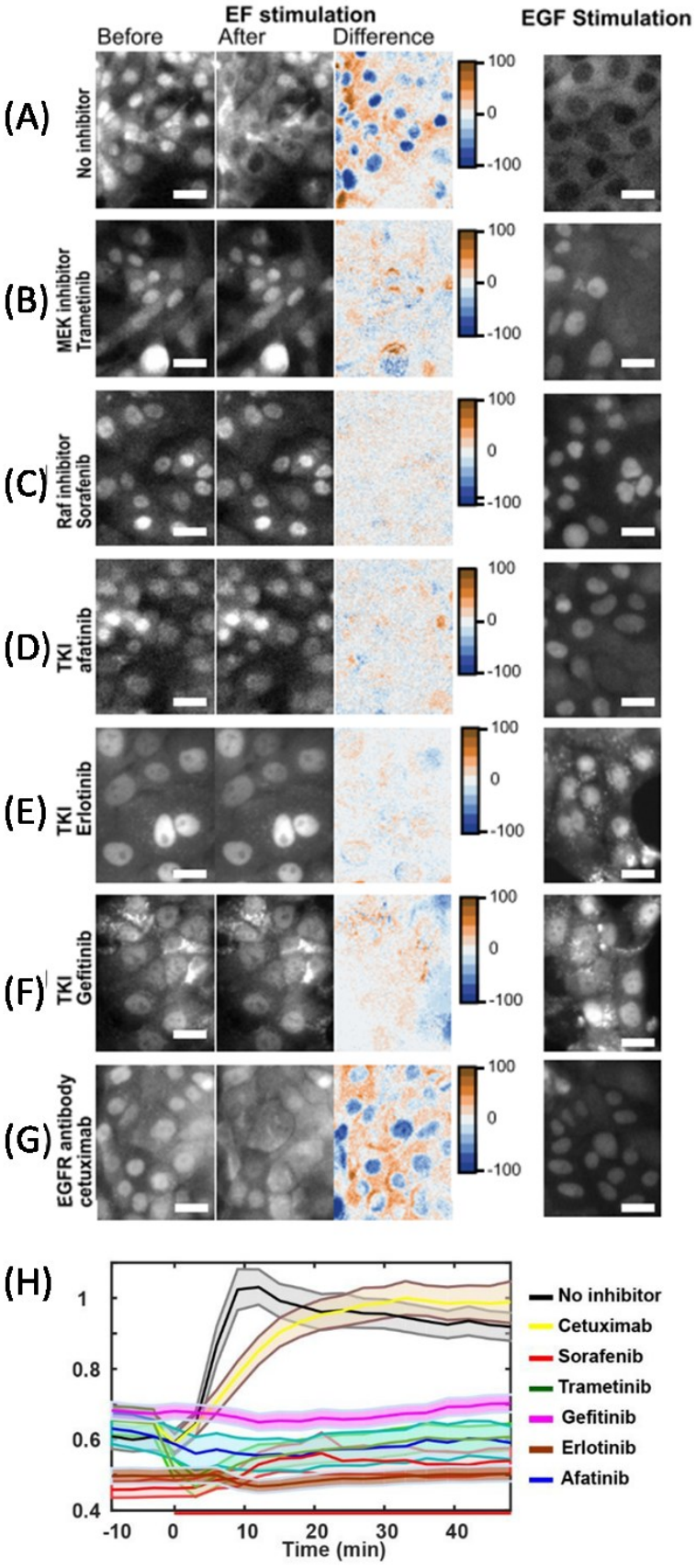
EF stimulation
EGF Stimulation
Before
After
Difference
(A)
No inhibitor
(B)
MEK inhibitor Trametinib
(C)
Raf inhibitor Sorafenib
(D)
TKI afatinib
(E)
TKI Erlotinib
(F)
TKI Gefitinib
(G)
EGFR antibody cetuximab
100
0
-100
(H)
1
0.8
0.6
0.4
-10
0
10
20
30
40
Time (min)
No inhibitor
Cetuximab
Sorafenib
Trametinib
Gefitinib
Erlotinib
Afatinib

Figure 2.7.20. The inhibitor test based on the EGFR signaling pathway. The left group constitutes the fluorescence images and intensity difference before and after AC EF stimulation and the right group portrays the fluorescence image after 2 ng / mL EGF chemical stimulation when (A) no inhibitor is applied, (B) 0.5 μM MEK inhibitor trametinib is applied, (C) 20 μM Raf inhibitor sorafenib is applied, (D) 5 μM TKI afatinib is applied, (E) 2 μM TKI erlotinib is applied, (F) 50 μM TKI gefitinib is applied and (G) 100 μg/mL EGFR antibody cetuximab is applied, respectively.(H) Time traces of ERKTR ratio as population average from cells under AC EF stimulations in (A-G). Mean and ± 95%CI are shown as a solid line and shadow region, respectively (n > 100 cells for each group).

2.8. Discussion and Conclusion

The modulation of cellular behavior has been an attractive topic since the discovery of physiological electricity in the living system. Conventional investigations into exogenous EF stimulation focus on DC voltage and suffer from both possible EF-induced environmental changes and the averaging effect of the long experiment and analysis time. In order to solve these issues, we developed a new chip platform that can deliver EF stimulations to cells with a finer temporal and spatial resolution.

In this project, we have achieved precise localized and synchronized ERK activation under AC EF stimulation at an intermediate frequency range, which would have direct influences on the conformations of membrane proteins based on previous theoretical models. Compared with previous studies, our experiment has three advantages. First, in our experiment system, we applied bipolar symmetric AC EF signals through high-k dielectric HfO_2 passivated microelectrodes, which eliminates Faradaic processes and avoids possible biochemical changes induced by DC or asymmetric EF signals through salt bridges or bare metal electrodes. Thus, for the first time, we demonstrate that an ERK signaling pathway activation with AC EF stimulation does not requires intermediate ion flows and chemical species induced by electrochemical

processes. Second, the cell was intact, and no strong perturbations were observed after stimulations. The EF signal we chose has a low amplitude and an intermediate frequency (50 kHz), which are thought to have no biological meanings in conventional studies. Third, the inhibitor test identified that AC EF may induce phosphorylation of EGFR without chemical signals. Unlike electrogenic membrane proteins such as ion pumps, EGFR is non-electrogenic and not sensitive to ion gradient. Our result suggests that EF stimulation can directly trigger ERK phosphorylation without EGF binding. Based on the theoretical simulations introduced in previous sections, our stimulation method will provide new insight into the interaction between cells or membrane proteins and EF stimulations.

In summary, we have demonstrated a new method to precisely modulate ERK activation at a fine temporal and spatial resolution via bipolar AC EF stimulation. Our HfO_2 passivated microelectrodes eliminates electrochemical processes, allowing for a clean analysis of the interaction between cells and AC EF stimulation. The ERK activation observed was triggered by an EF-induced EGF-independent phosphorylation of EGFR and does not relate to environmental changes such as pH, Ca^{2+}, and ROS.

2.9. Future Works

The modulation of ERK activation via bipolar AC EFs at an intermediate frequency is the first demonstration that suggests a direct interaction between AC EF signals and membrane proteins, and our newly designed device chip can be used as a novel platform for related investigations. Based on our experiment results, there are two aspects of future works we are interested in.

First, Ras is a family of proteins expressed in animal cells and involved in transmitting signals within cells. A recent discovery has suggested that mutated or overactive Ras signaling would lead to cancer development; therefore, the investigation and modulation of Ras protein is becoming an interesting topic. At the same time, Ras is an important signaling molecule between EGFR phosphorylation and Raf activation. Thus, our experiment setup may be a prime candidate for Ras behavior modulation and lead to new possible therapies for cancer treatment. However, as we are still in the early stage of this technique, there is a long journey ahead of us.

Second, the AC EF signal used in our ERK activation is a symmetric bipolar pulse at 50 kHz. Would this wave form necessary for the ERK activation? Investigation about the wave form itself, such as square wave, saw tooth wave and sine wave, would be an interesting topic. Furthermore, the change in the potential applied to local cells will affect the EF strength acting on the target cells, and this change in EF strength would also changes the membrane potential, which would trigger conformation changes of membrane proteins, resulting in downstream signaling pathway activities. Currently my lab mate Minxi has some ERK modulation experiment results about the wave form dependence and she is working hard on the data analysis.

CHAPTER 3. PLANAR NANOPORE DEVICE WITH AN ENGINEERED ELECTRIC POTENTIAL PROFILE

3.1. Introduction

Manipulation and detection of molecules is an important technique necessary to biochemical analysis and clinical diagnosis. Conventional methods have been developed based on specific binding, fluorescence imaging and electrophoresis. However, the sample preparation and instrument requirements limit the data analysis. Is there another possibility that avoids such complication? Apart from biochemical reactions specific to certain biomolecules, the charge and dipole distributed in molecule structures constitute another specific signature, which could be used to distinguish different molecules. Thus, sensing biological molecules based on their electric properties would be a straightforward paradigm for the next generation of biomolecule sensing. In addition, the electric potential and field distribution can be manipulated to govern the movement of charged and/or neutral molecules. Meanwhile, the development of semiconductor fabrication techniques achieves subtle fabrications down to a sub-10-nm level, allowing for the detector fabrication with a size close to a single molecule. Combining these two advantages together, a prime question to ask is whether the EF distribution can be engineered to manipulate and sense a single molecule at an ultimately small resolution.

To answer this question, many candidates for next-generation sensing techniques have been checked, and we believe that a nanopore device is a key platform for our investigation. Nanopore devices have demonstrated their capabilities in detection at the single-molecule level because of their precise and ultra-small channel size. Considering the principle of nanopore-based sequencing, which is based on a change in the current

through the nanoscale pore to detect the motion and structure of molecules that pass through it, it is essentially based on an engineered EF distribution at a length scale comparable to the diameter of a DNA molecule. The question is, can additional structures and facilities be built around a nanopore structure to achieve more complicated EF profiles for accurate manipulation and detection? In addition, there are two major paradigms of DNA sequencing via nanopores: On the one hand, the majority of studies focus on the analysis of ionic current which is directly associated with the geometry and size of the molecule; on the other hand, studies have also been conducted on detection based on tunneling current across the translocating molecule. Although integrating tunneling junctions into a nanopore device is highly attractive to achieve a higher resolution and additional control of molecule motions, the difficulties in the fabrication are overwhelming.

In this chapter, I first review the basic principles of nanopore devices and their fabrication methods. Then, I expand the discussion to include several approaches for the integration of additional modules for a flexible and precise control of molecules. After the literature review section, I will introduce our planar solid-state nanopore device with a microfluidic guidance structure for highly precise EF manipulation of molecules and detection by tunneling current. Last, I summarize our recent results regarding the correlated detection of DNA translocation events in both ionic and tunneling current channels for the first time.

3.2. History of Nanopore Sensing

During the past decades, researchers have discovered that DNA, first discovered via X-ray crystallography by Watson and Crick in 1953 [83], plays an important role in

different aspects of living cells. With advancing physical probing techniques, the DNA molecule is commonly known to be a stable, double-helix-structured polymer consisting of repeating basic units called nucleotides. Each nucleotide is made up of a deoxyribose sugar, a phosphate group, and one of the following four nitrogenous bases: adenine (A), thymine (T), cytosine (C), or guanine (G). The DNA double helix structure is formed by two chains of nucleotides connected with hydrogen bonds between A and T or between C and G. This structure has a diameter of approximately 2.2 nm for double-stranded DNA, and the spacing between two consecutive nitrogenous bases is about 3.4 Angstrom [84]. Apart from the simple structure, the sequence of nucleotides in a DNA strand contains all the information for building the structure and fulfilling the functions of an organism. The process of synthesizing proteins based on the DNA nucleotides involves two steps: transcription and translation. In the transcription process, messenger ribonucleic acid (mRNA) copies the sequence of bases of a certain section in DNA, and in the translation process, ribosomes build the target protein from amino acids according to the nitrogenous base sequence of mRNA. The structure and function of proteins thus directly relate to the nucleotide sequence of DNA.

Given the critical role of DNA in biological systems, determining how to better analyze the structure of a DNA sequence is an interesting topic for various reasons. Twenty-four years after the discovery of the DNA structure, Sanger's development of "chain-termination" opened the door to full DNA sequencing in 1977 [22], but only for DNA fragments with a length shorter than 1 kilobase (kb). The first-generation DNA sequencing technique was developed based on "chain termination" and electrophoresis, providing a slow but accurate DNA sequencing result. Twenty-one years later, Ronaghi

and his colleagues developed the second-generation DNA sequencing technique [23] based on the real-time signal collection of pyrophosphate. This method allows for a mass parallelization of sequencing reactions, thereby increasing the amount of DNA tested in a single run. Both Sanger and Ronaghi's methods are "sequence-by-synthesis (SBS)" methods working with short DNA fragments, and they require DNA polymerase and massive DNA samples during the sequencing. To achieve single-molecule sequencing and real-time sequencing, several novel sequencing methods at the single molecular level have been developed in the past 40 years [24-27]. However, they all require preparation of samples before testing, which complicates and slows the analysis process.

Among all those candidates for third-generation DNA sequencing techniques, nanopore analysis is a promising and versatile method permitting single-molecule detection without substrate labeling and immobilization. Developed from the idea of mimicking molecule transportation through protein channels between intracellular and extracellular environments, current nanopore sensor devices have already demonstrated their promising results at a single-molecule level and label-free detection in the characterization of DNA and other biomolecules. However, there are still challenges for existing nanopore technology to achieve the scalability and reproducibility of fabrication, translocation control, and high-resolution signal readout.

3.3. Mechanisms of Nanopore Based Sensing

Unlike the first and second generation techniques for DNA sequencing, nanopores provide a straightforward method to detect DNA sequence and other molecules without complicate sample preparation. In general, nanopore-based sensing determines DNA sequences according to the modulation of current measured during the translocation.

Based on this measured current, there are two paradigms of nanopore sensing: ionic current sensing and tunneling current sensing.

3.3.1. Nanopore Sensing Based on Ionic Current

Inspired by natural molecular translocation through cell membrane via protein channels, a nanopore device consists of a nanopore inserted into an insulating membrane, which separates two liquid chambers. The principle of nanopore sensing is similar to the Coulter principle [28] in the field of flow cytometry, and a typical nanopore structure is illustrated in Figure 3.3.1. One (the *trans*- chamber) of these two chambers is filled with an electrolyte solution, and the other (the *cis*- chamber) is filled with an electrolyte solution with biological molecules. A potential is applied across the membrane between the two chambers via two Ag/AgCl electrodes, inducing an ionic current through the nanopore, which is monitored by an amplifier. Negatively charged molecules in the *cis* chamber, which has a lower potential, will be driven toward the nanopore, causing transient reductions in the ionic current. If the nanopore size is comparable to the width of a molecule, then the molecule will be forced to uncoil and pass the nanopore in a single file. The amplitude, translocation duration, and event frequency of the transient current modulations are the result of the intrinsic physical properties of molecules and the interaction between the nanopore and target molecules.

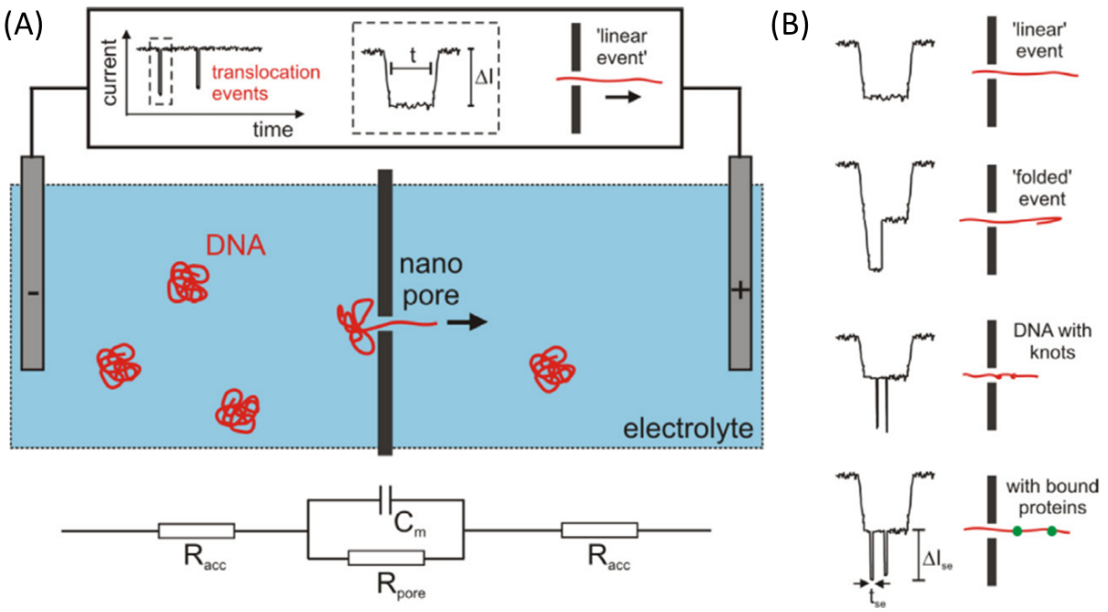

Figure 3.3.1. Nanopore DNA sequencing principle via ionic current. (A) A basic nanopore DNA sequencing setup with an insulating membrane, with a nanopore (black) separating two reservoirs filled with electrolytes. A potential is applied through the nanopore via electrodes, and DNA molecules (red) are driven through the pore channel. Top: illustration of the ionic current readout of the DNA translocation event. (B) Examples of different translocation signal shapes and the possible DNA structures according to each type of signal. From [30].

3.3.2. Nanopore Sensing Based on Tunneling Current

Recent research has also developed a new detection method using the quantum tunneling current instead of the ionic current. By applying this measurement paradigm, two significant advantages can be achieved. First, the spatial resolution of detection will be highly improved because the cross section of the detection components, such as embedded electrodes, is comparable with the cross section of a single base [85]. Meanwhile, the ionic current detection cannot reach such a spatial resolution unless the pore thickness is comparable with its width. The second advantage is that the quantum tunneling effect can achieve transit times as fast as a femtosecond, allowing for fast recording and distinguishing of single bases [86, 87]. In this method, molecules are

driven through a nanopore or nanochannel, where a set of sensing components, typically a pair of electrodes, is normally created close to the channel. This set of sensing components will measure the electron tunneling current between the gap of two electrodes. When different bases are passing through the electrode gap, unique signatures will be recorded due to the difference in electronic and chemical structures. These signature signals are independent of their neighborhoods, making them a gold standard for future single-base sequencing. A schematic of the basic idea of tunneling sequencing in a typical nanopore device is presented in Figure 3.3.2, and different approaches have been developed over the past decades.

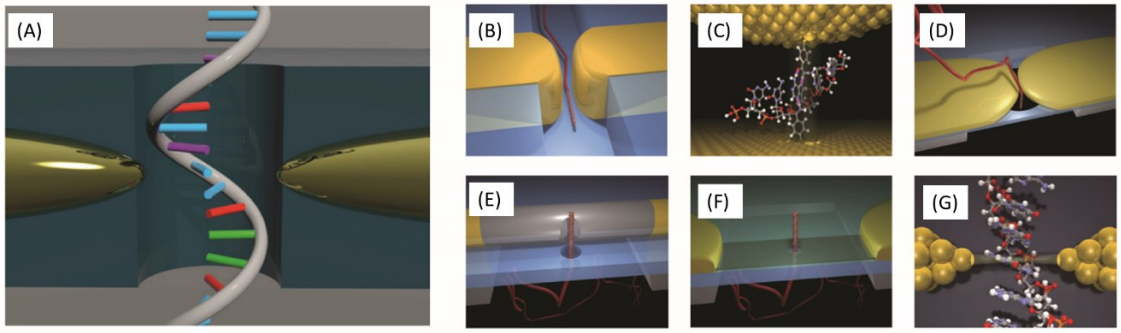

Figure 3.3.2. Schematics of the tunneling sequencing in a typical nanopore device (A) and other approaches (B–G). (A) An embedded nanogap in a typical nanopore made on a silicon substrate. (B) A nanogap embedded in a nanofluidic channel. (C) Single-base molecule detection via tunneling currents flowing between a gold probe and a gold substrate that are functionalized with recognition molecules. (D) A nanogap aligned with a solid-state nanopore. (E) A nanopore embedded in a silicon nanowire field-effect transistor (FET). (F) A nanopore embedded in a graphene nanoribbon. (G) A nanogap between gold electrodes made by a mechanically controllable break junction. From [88].

3.4. Development of Nanopore Devices

In recent decades, a variety of nanopore devices with various characteristics have been developed, and these applications can generally be divided into two types based on

the nature of the nanopore: biological nanopores and solid-state nanopores [89-92]. A biological nanopore device embeds existing nanopore structures, such as toxins and protein channels on a cell membrane, into electrically insulating membranes, while a solid-state nanopore device has its nanopore fabricated from thin, inorganic, polymeric membranes. In the next part of the review, I first introduce biological nanopores and conventional solid-state nanopores. Then, I discuss the attempts made to slow down the translocation speed of conventional solid-state nanopores. Last, I introduce the novel nanopore utilizing the quantum tunneling method and mutant devices such as nanopipettes.

3.4.1. Starting from Biological Nanopores

The first functional nanopore device was demonstrated by Kasianowicz et al. in 1996 [93]. This first biological nanopore uses α-hemolysin because its protein channel has a limited aperture size of 1.5 nm, which allows only single-stranded DNA (ssDNA) and RNA molecules to pass through (as illustrated in Figure 3.4.1). The polynucleotide translocation through the nanopores creates transient current modulations, whose duration is proportional to the molecular length and inversely proportional to the potential bias. This initial demonstration highlights the capability of DNA sensing and lays the foundation for nanopore sensing.

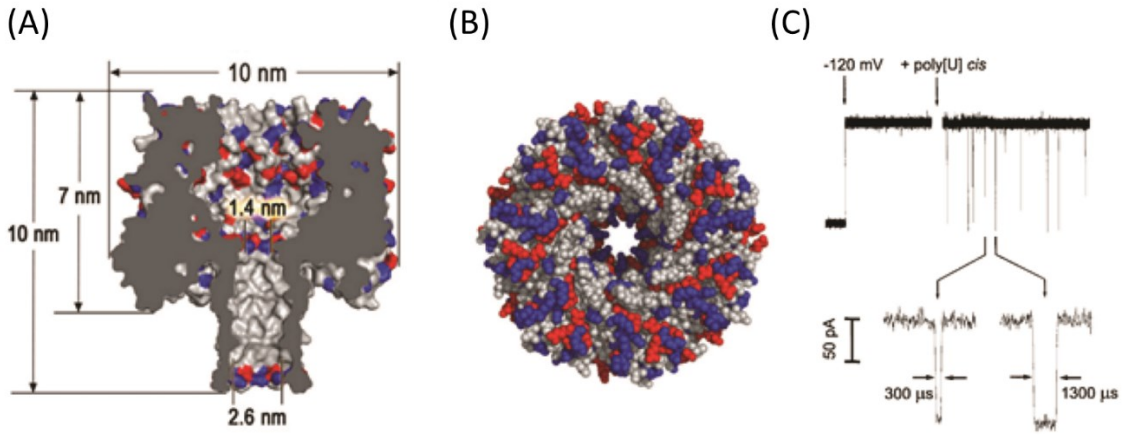

Figure 3.4.1. Heptameric α-hemolysin toxin structure and translocation data. (A, B) Side and top views of heptameric α-hemolysin toxin [94]. (C) The ionic current readout when oligomers of poly[U] are driven through the α-hemolysin. When oligomers of poly[U] are added, the ionic current baseline under -120 mV is interrupted by transient blockade spikes. A detailed depicts typical spikes with their amplitudes and duration times. From [93]

In 1999, Akeson et al. demonstrated the nucleotide type discrimination based on the ionic current signal with α-hemolysin [95]. In this experiment, homopolymers of polycytidylic acid (poly C), polyadenylic acid (poly A), and polyuridylic acid (poly U) were distinguished from one another based on the blockade's ionic current amplitude and duration. During this time, the translocation time of DNA and RNA molecules ranged from several hundred microseconds to a few milliseconds, which is still too fast to determine the nucleotide sequence. Therefore, slowing down the DNA translocation speed is an important research aspect in DNA nanopore sequencing. In 2012, phi29 DNA polymerase (DNAP) performed a control of DNA translocation using α-hemolysin and Mycobacterium smegmatis porin A (MspA) [96, 97]. In this application, the target DNA molecule is combined with phi29 DNAP and a blocking oligomer. The nanopore captures this DNA-polymerase complex, and the DNA will be unzipped from the blocking oligomer and driven from the *cis*- chamber to the *trans*- chamber under bias. Once the

blocking oligomer is completely unzipped, the 3'-OH terminus of the DNA is exposed in the polymerase active site, and phi29 DNAP will start DNA replication, which pulls the DNA molecule through the nanopore from the *trans*- to the *cis*- chamber. The target molecule will be read twice, and a 90% reading accuracy is achieved in this paradigm. Apart from α-hemolysin and MspA, other biological nanopores have been reported for DNA sequencing, including Escherichia coli cytolysin A (ClyA) [98], bacteriophage SPP1 DNA packaging motor [99], outer membrane protein G (OmpG) [100], and aerolysin [101].

In 2014, Oxford Nanopore released the first commercial DNA sequencing device, MinION, in its large-scale collaborative MinION Access Program (MAP). The MinION is a compact and portable device controlled by software. One flow cell of the device contains 2,048 individual protein nanopores, and a quarter of them are monitored by the software. This allows for a deconvolution method to further improve the sequencing accuracy. At any given time, the readout signal is assumed to be a contribution of five bases, or "5-mers." The whole system is thus treated as a hidden Markov model in which the 5-mer sequence produces an observable data set. As DNA molecules translocate through pores, a Viterbi algorithm will interpret the data set into the most likely DNA sequence. One year after release, due to improvements to the software algorithm, the readout accuracy has improved to 99% accurate reads mapping to references at a mean identity of 85% [102], from only a quarter of reads mapping to references at an under-10% average identity [103]. Oxford Nanopore Technologies continues its efforts regarding nanopores in both hardware and software, and the company has demonstrated

the promising sequencing result with its commercial nanopore devices [104], indicating that MinION and its successors will be the next-generation sequencing instruments.

3.4.2. Conventional Solid-state Nanopores via Ionic Current Detection

The biological nanopore and its commercial products demonstrate the nanopore's high sensitivity and fine resolution; however, there are still other reasons to conduct research on solid-state nanopores. On the one hand, the biological nanopore is limited by its fixed pore size, and only a few target molecules can hence be detected. On the other hand, the biological nanopore structure has mechanical and/or chemical issues compared to dielectrics and metals. A solid-state nanopore will overcome these limitations of the biological nanopore because of its adjustable pore size, mechanical and chemical stability, reproducible fabrication techniques, and integration compatibility with electronics.

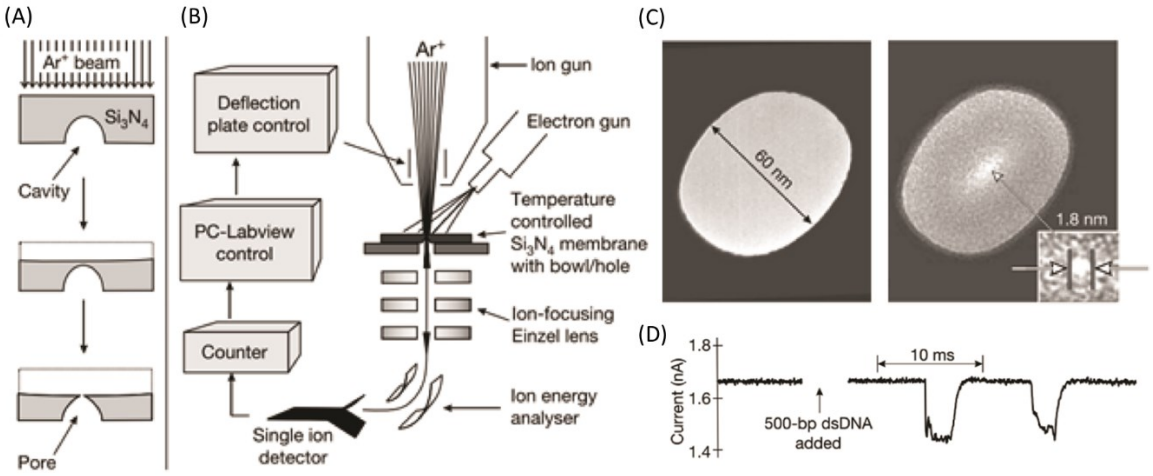

Figure 3.4.2. The first solid-state nanopore. (A) The fabrication of a freestanding Si_3N_4 membrane with a cavity. (B) Schematics of the feedback-controlled ion beam sculpting system. (C) TEM image of the initial 61-nm diameter pore by FIB (left) and the same pore after Ar^+ ion beam exposure. The insert displays the final nanopore. (D) The translocation of DNA through a 5-nm diameter pore. From [105].

The first solid-state nanopore was reported by Li *et al.* [105] in 2001, shortly after the first demonstration of Akeson's biological nanopore. As illustrated in Figure 3.4.2, a bowl-shaped cavity was made by reactive ion etching (RIE) on the bottom surface of a freestanding silicon nitride (Si_3N_4) membrane. Then, an Ar ion beam was used to remove the material from the top surface of the Si3N4 membrane. Once the single ion detector received any signal through the membrane, the nanopore formed at the center of the cavity. Due to the geometric relation between the overall milling and the bowl-shaped cavity, the transmitting ion flux through the pore was monitored during the milling, and it could be used as an indicator to control the pore size when an ideal flux value was reached. With a precisely controlled nanopore, DNA translocation was hence demonstrated with a 5-nm-diameter pore [106].

In 2003, Storm *et al.* demonstrated the most commonly used structure of solid-state nanopores [107]. They reported a new technique with single nanometer precision and direct visual feedback, utilizing state-of-the-art silicon technology and transmission electron microscopy (TEM), as illustrated in Figure 3.4.3. An initial pore between 20 nm and 200 nm was fabricated on a silicon-on-insulator (SOI) wafer via electron beam lithography and anisotropic etching, and then a 40-nm-thick silicon oxide (SiO_2) was then formed on the surface of the pore. After the initial pore was prepared, the researchers used a TEM beam with an intensity between 10^5 and 10^7 $A \cdot m^2$ to deform the pore. Based on their experience, a pore with a diameter larger than 80 nm will expand under the TEM beam, while a pore with a diameter smaller than 50 nm will contract at a rate of 3 Å per minute. This phenomenon enables fine tuning of the pore size with a precision related to the instrument resolution and the SiO_2 surface roughness. After the precise control of the

pore size on a SiO_2 membrane, the researchers studied the model and experiments of dsDNA translocation through their device in 2005 [108]. The most probable translocation time τ and the polymer length L_0 revealed a power-law relation $\tau \sim L_0^{1.27}$ for a DNA fragment from 6,557 to 97,000 base pairs (bps), and Storm's model yielded a comparable result of $\tau \sim L_0^{1.22}$. Interestingly, this result demonstrates a fast DNA translocation through a solid-state nanopore, while the biological nanopore exhibited a slow translocation.

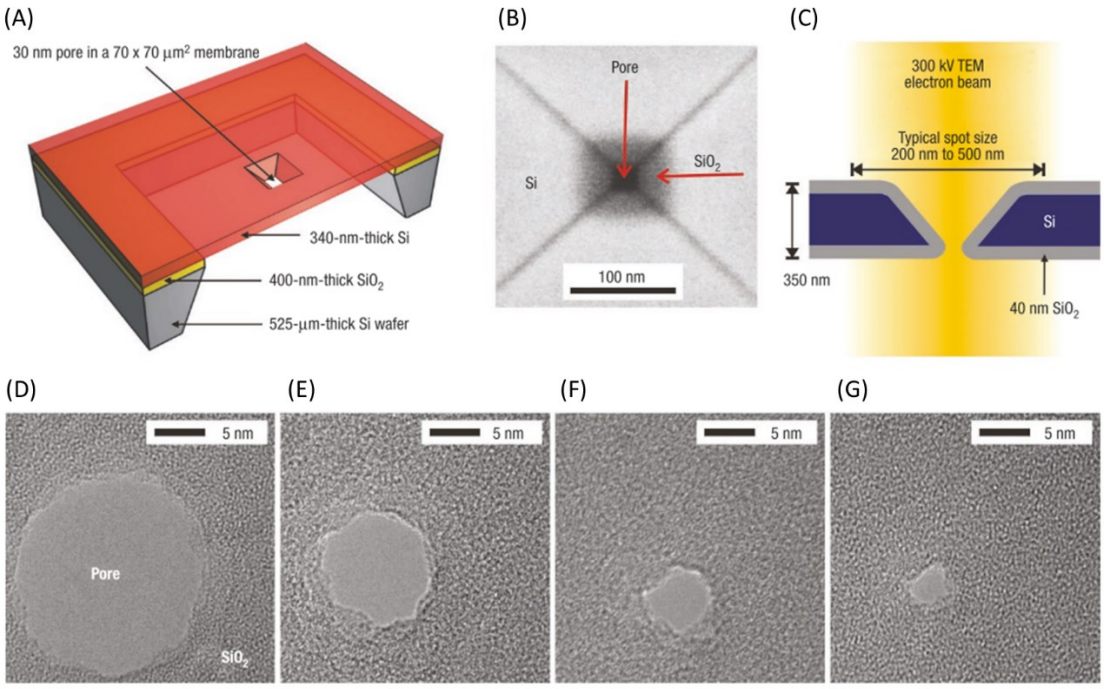

Figure 3.4.3. Fabrication of silicon oxide nanometer-sized pores via the effect of electron irradiation. (A) Cross-section view of the device. (B) SEM of the top view of the initial pore after wet etch. (C) A cross-section schematic of the pore during TEM electron irradiation. (D–G) TEM images of the pore shrinking from its initial size to the desired size. From [107].

Since the successful size-control-based TEM from Storm, many researchers have focused their efforts on improving the nanopore fabrication technique and understanding

the mechanics of DNA translocation through a nanopore. Heng *et al.* conducted an electromechanical property study of DNA driven through a nanopore under EFs in 2006 [109]. They fabricated nanopores in a silicon nitride (Si_3N_4) membrane by stimulated decomposition and sputtering with a tightly focused electron beam in TEM, creating nanopores with an hourglass shape in cross section with aperture diameters under 3 nm. Their study demonstrates that the threshold of dsDNA permeation through a pore with a diameter under 3 nm is dependent on the EF and pH of the DNA solution. The threshold EF required for dsDNA translocation decreases when the pH becomes more acidic, resulting in the destabilization of the double helix. In 2008, Wanunu *et al.* performed a detailed investigation of the surface interaction between solid-state nanopore size and DNA molecules [110]. The authors systematically analyzed the translocation dynamics as a function of nanopore size, DNA length, driving potential, and temperature in a range where DNA can only enter the nanopore in a single-file configuration. Their results suggest that a subtle decrease in nanopore size will lower the probability of DNA translocation, and an increase in the translocation time by decreasing the nanopore size or temperature is greater than an order of magnitude compared to larger pores, which may relate to increased interaction between DNA and nanopores.

3.4.3. Slowing Down the Translocation

At the early stage of the development of biological nanopores, studies have shown the precise size control of solid-state nanopores and successful DNA translocations; however, one major issue makes solid-state nanopores less competitive than biological nanopores: the DNA translocation speed. Although slowing down the DNA translocation speed is necessary in both biological and solid-state nanopore applications, the

translocation speed in solid-state nanopores is a few orders of magnitude faster than in biological nanopores.

To slow down the translocation speed in solid-state nanopores, three major strategies are investigated. The first strategy involves modifying the experimental condition based on the initial work. Li *et al.* showcased the slowing down by a systematical control of solution viscosity, bias, DNA molecule length, electrolyte temperature, and salt concentration after their demonstration of the first nanopore [111, 112]. Furthermore, in 2012, Kowalczyk demonstrated a slowing down of DNA translocation by replacing the normally used a potassium chloride (KCl) solution with sodium chloride (NaCl) or lithium chloride (LiCl) [113]. He studied the charge reduction of DNA molecules when binding to different counterions with all-atom molecular dynamics (MD) simulations, and he found that the translocation speed through a solid-state nanopore slows down when the counterions decrease in size from K^+ to Na^+ to Li^+, both for dsDNA and ssDNA (illustrated in Figure 3.4.4). The second strategy involves dragging the DNA molecule with physical forces. Keyser *et al.* presented a combination of solid-state nanopores and optical tweezers [114]. Unlike flowing only DNA molecules through a nanopore, they made beads coated with DNA molecules and used optical tweezers to control the bead position near the nanopore precisely. Peng *et al.* also reported a similar method using magnetic tweezers to achieve a "reverse DNA translocation" to slow down the translocation [115]. The third strategy involves modifying the nanopore structure material or surface coating to enhance the interaction between the nanopore and DNA molecules. Venkatesan *et al.* demonstrated a reduction in translocation speed in a nanocrystalline aluminum oxide (Al_2O_3) nanopore in comparison

to Si_3N_4 and SiO_2 architectures [116]. The translocation speed reduction is the result of the strong electrostatic binding events between DNA and positively charged nanopore surfaces, which have a high surface charge density and roughness. Similar methods using different materials have also been investigated, including graphene [117], boron nitride [118], DNA origami [119], and hafnium oxide [120].

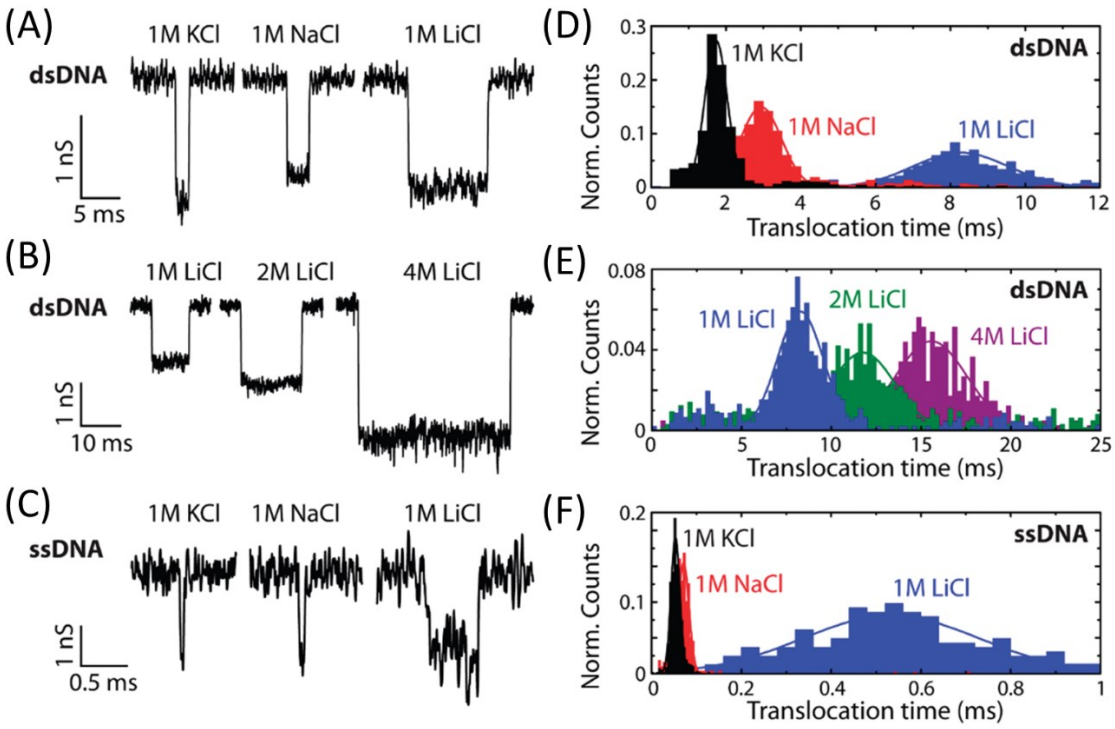

Figure 3.4.4. Slowing down the DNA translocation in LiCl. (A) Ionic current recording for lambda dsDNA filter at 5 kHz in 1 M KCl (left), 1 M NaCl, and 1 M LiCl. (B) Ionic current recording for lambda dsDNA with different LiCl concentrations. (C) Ionic current recording for M12mp18 ssDNA in an additional 8-M Urea, filtered at 30 kHz. (D–F) Translocation time histogram of (A–C). From [113].

3.4.4. Besides the Nanopore

Despite all of the above-mentioned attempts to slow down the translocation speed, none of them have demonstrated a three to four orders of magnitude reduction that would enable single base sequencing. Apart from modifying the parameters within a

conventional solid-state nanopore structure, adding an additional set of control electrodes seems to be emerging as an active method to slow down the translocation speed through a gating effect. Moreover, the additional set of electrodes offers the chance to detect the current in a transverse direction, or tunneling current, when DNA molecules are passing through the nanopore. The promising potential of the detection method has been demonstrated, and it is becoming a new branch of nanopore sensing techniques.

In 2007, Polonsky *et al.* proposed the concept of embedding a pair of control electrodes within a solid-state nanopore [121]. The membrane of the nanopore they proposed has a sandwich structure consisting of dielectric layers on either side of an electrode stack. The electrode stack consists of three thin metal layers separated by dielectric films. The calculation suggests that such a structure will trap DNA in a potential well and step it one base at a time through the nanopore when the thickness of the inner metal layer and its two adjacent dielectric layers are controlled. To create an energy barrier to trap DNA molecules, the dielectric layers should be half-integer multiples of the single-base separation, and the central layer should be close to an integer multiple. Further computational and experimental studies have been conducted by the same group [122-124], but no actual DNA translocation has been demonstrated with such a structure.

Instead of placing control electrodes inside the nanopore membrane, fabricating them near the nanopore opening is another routine that researchers have demonstrated. Fischbein *et al.* have reported the capability to fabricate a sub-10-nm device with transmission electron beam ablation lithography (TEBAL), and they used this technique to fabricate a transverse electrode aligning with a drilled nanopore [125, 126]. This

fabrication unfortunately suffered from a low yield of 15%. Some of the surviving devices failed to capture translocation events based on ionic current, suggesting some blocking of the pore by the electrodes. A possible reason may be the atom migration physically blocking the pore or the surface charge repelling the DNA from threading through the pore.

In 2010, Ivanov successfully demonstrated a nanopore device with a transverse nanoelectrode, as illustrated in Figure 3.4.5 [127]. The initial device contained a 70-nm-thick SiN_x membrane with a pair of gold electrode tips with a 2-μm gap. The initial pore was fabricated via the standard FIB milling technique, resulting in a 50-nm pore on the membrane. Then, a pair of platinum (Pt) nanoelectrodes with an expected gap size around 3 nm was fabricated by electron beam-induced deposition (EBID). EBID is a common process for FIB tools to protect the sample with a Pt layer, and it is used for direct deposition of a metal structure on the sample. This hybrid device can record both ionic current and tunneling current, and it can control the translocation speed. As a result, most lambda DNA translocation events can only be seen by ionic current, and their translocation time is in the sub-millisecond time frame. Other slower events could be detected by both ionic and tunneling currents, and their translocation time was greater than 1 ms. This slowing down effect is likely due to the absorption or trapping at the tunneling junction.

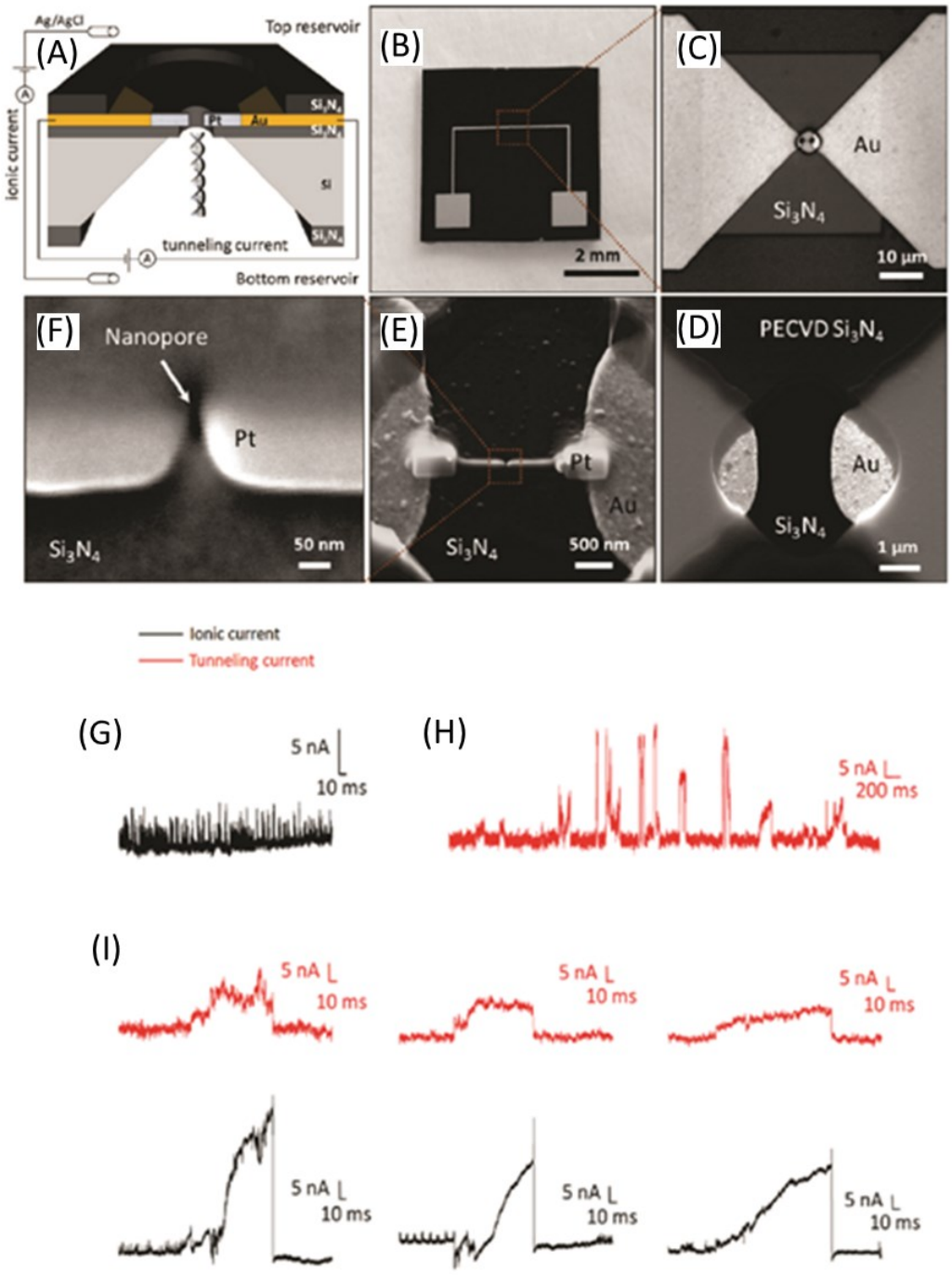

Figure 3.4.5. Nanopore device with transverse electrodes. (A) Schematic of the nanopore device with aligned embedded electrodes. (B) Optical image of the device chip. (C) The Au microelectrodes aligned on a freestanding Si3N4 membrane. (D) SEM image of the window in the PECVD Si3N4 layer opened by RIE. (E) SEM image of the Pt electrode deposited by EBID. (f) SEM image of the nanopore aligned to the Pt nanoelectrodes. (G,

H) lambda DNA translocation signal detected with the device in ionic (black) and tunneling currents (red). (I) Examples of coincidental long-lived events in both currents. From [127].

Considering the structure of conventional nanopore devices with controlling electrodes, nanogap devices become possible candidates to overcome the challenges in DNA sequencing, as illustrated in Figure 3.4.6. Liang *et al.* reported an initial nanogap system with embedded electrodes for fast, real-time, label-free DNA analysis [128]. The whole process involves a nanoimprint and standard semiconductor fabrication technique, allowing easy access for mass fabrication. The translocation events are recorded with the tunneling current through the nanoelectrodes. Although the translocation time is still hundreds of microseconds, this demonstration highlights the capability of DNA translocation in a planar nanopore or nanogap device. Moreover, in 2012, Tsutsui *et al.* showed a slowing down of DNA translocation using a transverse EF via a nanogap in a nanopore [129]. The field-retarded translocation improved the spatial resolution of nanopore detection. However, the crosstalk between the ionic current and transverse sensing current was not negligible, causing a concomitant rise in the transverse current, displaying a similar line shape to that of the ionic current. Additional effort is thus needed to minimize the ionic current contribution to the transverse tunneling current.

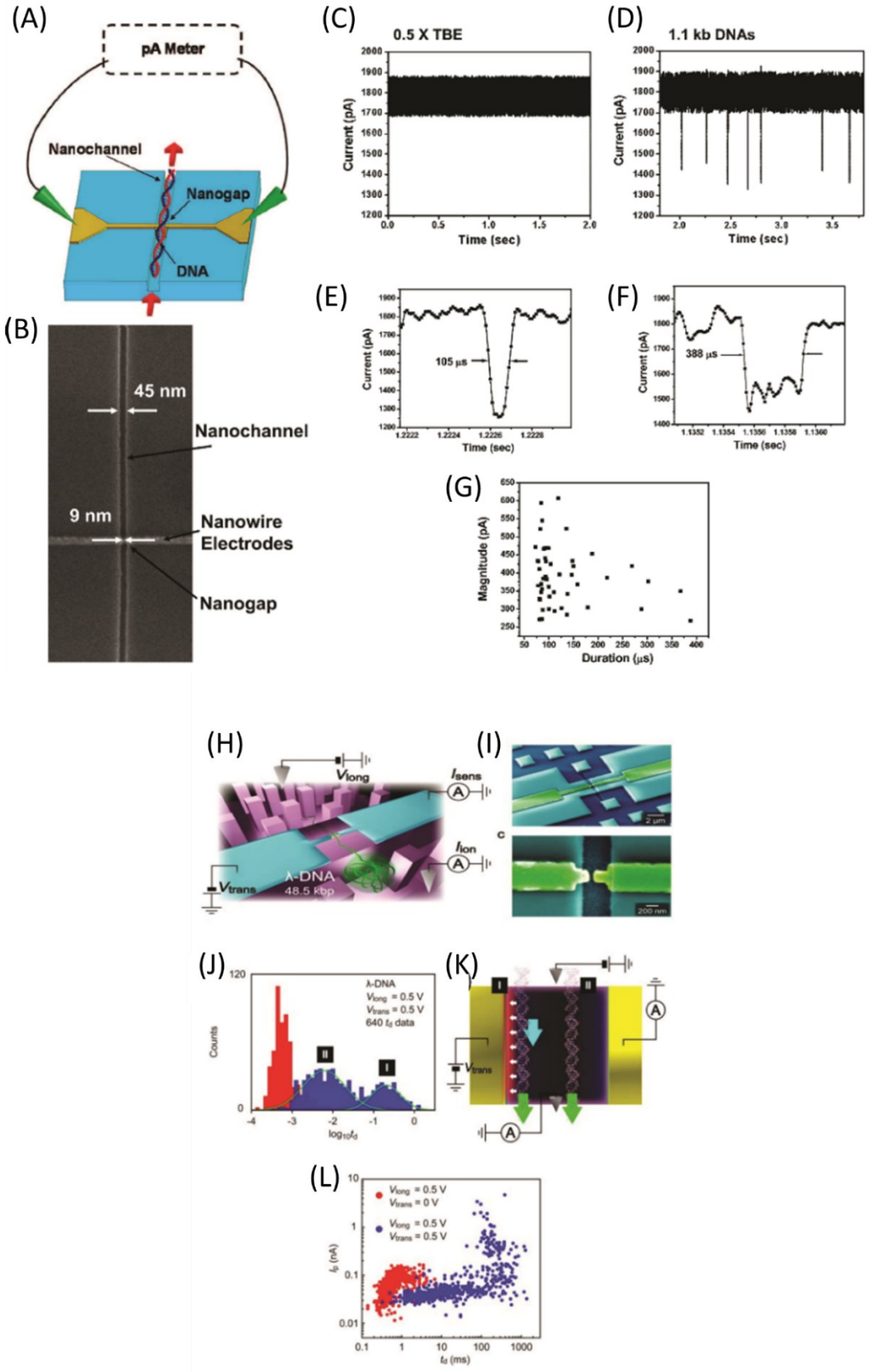
(A)
pA Meter
Nanochannel
Nanogap
DNA
(B)
45 nm
Nanochannel
9 nm
Nanowire Electrodes
Nanogap
(C)
0.5 X TBE
Current (pA)
Time (sec)
(D)
1.1 kb DNAs
Current (pA)
Time (sec)
(E)
105 μs
Current (pA)
Time (sec)
(F)
388 μs
Current (pA)
Time (sec)
(G)
Magnitude (pA)
Duration (μs)
(H)
Vlong
Isens
Ilon
Vtrans
λ-DNA
48.5 kbp
(I)
2 μm
200 nm
(J)
λ-DNA
Vlong = 0.5 V
Vtrans = 0.5 V
640 td data
Counts
log10td
(K)
Vtrans
(L)
Vlong = 0.5 V
Vtrans = 0 V
Vlong = 0.5 V
Vtrans = 0.5 V
Ip (nA)
td (ms)

Figure 3.4.6. Liang's nanogap device (A–G) [128]. (A) Schematic of the nanogap DNA detector inside a nanofluidic channel. (B) SEM image of the top view of the nanogap detector without top sealing plate. (C, D) Tunneling current recording before and after dsDNA molecules were added to the solution. Translocation events with a duration of ~100 μs (E) and ~388 μs (F). (G) Distribution of pulse duration and amplitude. Tsutsui's planar nanochannel sensor with embedded electrodes (H–L) [129]. (H) Schematic of the nanochannel sensor with embedded electrodes. (I) Pseudo color SEM images of the nanochannel device. (J) The trapping duration histogram of the current blockade event data. Red data denote the distribution under V_{trans} = 0 V, and blue data indicate the distribution under V_{trans} = 0.5 V. (K) Schematic of two types of DNA translocations. Some DNA molecules are attracted to the high potential electrode, while other DNA molecules are not affected, because of the screening effect when V_{trans} is applied. (L) The distribution of blockade current (I_p) and translocation duration (t_d), showing the slowing down of translocation duration time when V_{trans} = 0.5 V is applied, marked in blue, compared to that when V_{trans} = 0 V is applied, marked in red.

Another competitor for conventional nanopore devices is a nanopipette, depicted in Figure 3.4.7. Steinbock *et al.* demonstrated a DNA translocation experiment using a nanopipette in 2010 [130]. A quartz glass capillary was pulled on both ends in a pipette laser puller and shrunk to the desired diameter under laser illumination. Based on the parameters, the pipette tip inner diameter was controlled to be around 20 nm. This simple structure demonstrates DNA translocations with different biases, showing a similar results to those of Li [106]. Moreover, the researchers combined the nanopipette with optical tweezers, allowing for a high-resolution force measurement during a single DNA translocation inside the tip. In addition to conventional modification to testing parameters and surface coating or modification, Cadinu et al. demonstrated a double-barrel nanopipette to control single-molecule translocation [131]. Due to the novel structure, a three-terminal architecture could be achieved, and it demonstrates that a DNA molecule can be efficiently confined and trapped between two pores with the tuning of EF in both barrels.

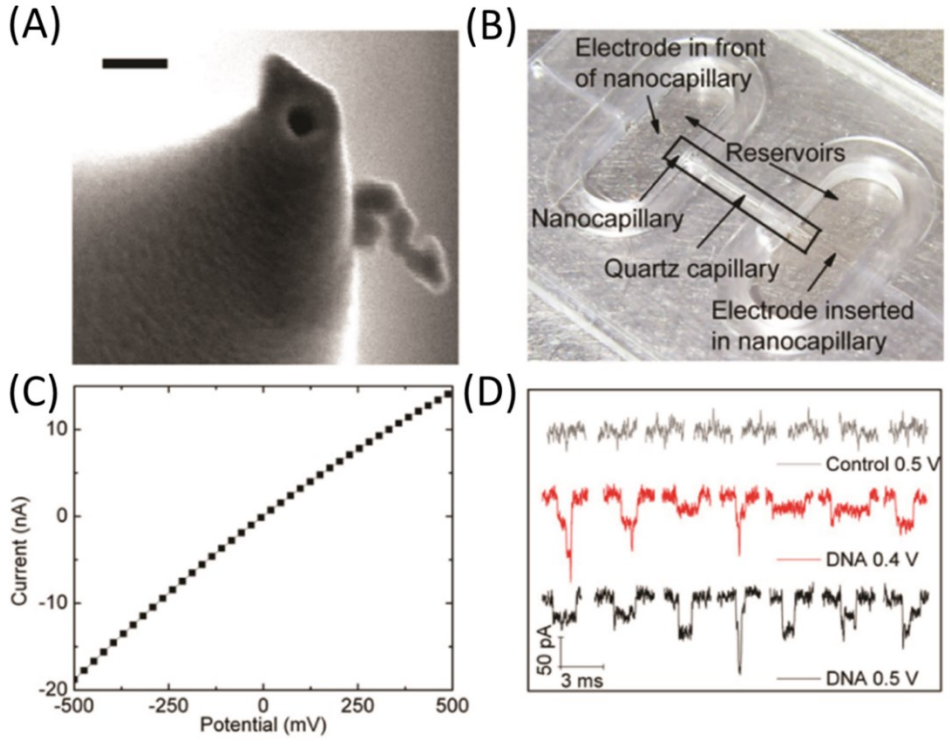
(A)
(B)
Electrode in front of nanocapillary
Reservoirs
Nanocapillary
Quartz capillary
Electrode inserted in nanocapillary
(C)
Current (nA)
Potential (mV)
(D)
Control 0.5 V
DNA 0.4 V
DNA 0.5 V
50 pA
3 ms

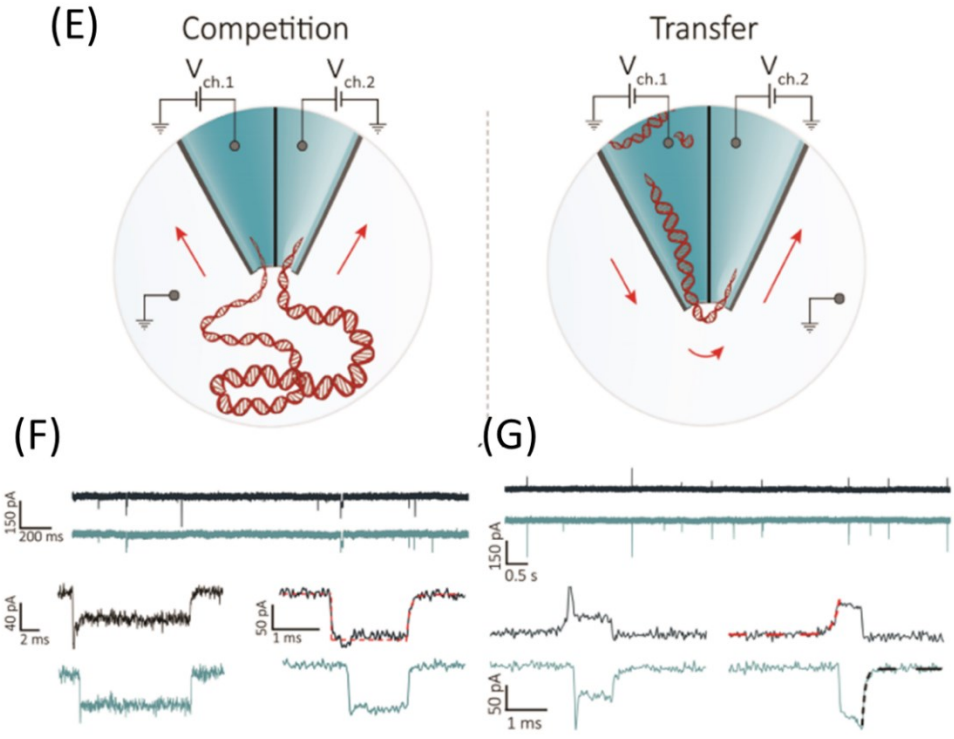
(E)
Competition
Transfer
V ch.1
V ch.2
(F)
(G)
150 pA
200 ms
40 pA
2 ms
50 pA
1 ms
150 pA
0.5 s
50 pA
1 ms

Figure 3.4.7. Steinbock's nanopipette device (A–D) [130]. (A) SEM image of a quartz glass nanocapillary after pulling with a laser-assisted pipette puller. The inner diameter of the tip is ~40 nm. Scale bar is 80 nm. (B) Assembled PDMS cell with two reservoirs connected by the nanocapillary. (C) Current-voltage curve of the nanocapillary is 0.5 M KCl. (D) Control and DNA translocation events recorded at 0.4 V and 0.5 V. The control experiment displayed no translocation events when no DNA molecule was added. Cadinu's double-barrel nanopore (e–g) [131]. (E) Schematic of the two unique operation modes. In competition mode, DNA molecules are attracted to the two pores with the same positive potential. As a result, the DNA molecules will be trapped between the two pores. In transfer mode, the two pores have opposite polarity potentials, driving DNA molecules out from one pore and threading them into the other pore. (F) Current traces of the two channels during competition mode. The top panel presents the ionic current recordings of Channel 1 (top) and Channel 2 (bottom). The bottom panel portrays two examples of the translocation events. (G) Current traces of the two channels during transfer mode. The top panel depicts the ionic current recordings of Channel 1 (top, -400 mV) and Channel 2 (bottom, 400 mV). The bottom panel display two examples of the translocation events.

3.5. Planar-Gated Nanopore Device Design and Preparation

Biological nanopore devices have demonstrated a slow translocation speed and a higher contrast of ionic current with membrane protein channels and their mutants after the release of MinION from Oxford Nanopore Technologies. However, there is still a strong interest in solid-state nanopores because the readout limit of the ionic current detection is about 3 nm [132], resulting in additional data analysis to decode the signal combination from several bases in biological nanopores. To reach single-base detection, solid-state nanopore devices have their advantages in integrating additional control and detection structure near the nanopore. Among different trials, the integration of tunneling current detection methods on solid-state nanopore devices has a great potential due to the intrinsically high spatial resolution. However, current fabrication techniques concentrate on FIB [127], EBID [133], top-down lithography and electromigration [134] and they have a low yield in production. Meanwhile, the pore size and structure alignment control

via top-down lithography methods are not ideal during the integration of tunneling detection electrodes and nanopore devices [129, 135-138].

Aiming at improving the production efficiency and the pore size control, we have designed a planar scalable nanopore device with a self-aligned transverse tunneling junction with a hybrid fabrication strategy based on photolithography and feedback-controlled electrochemical deposition [139]. This strategy consists of two steps of nanopore device fabrication, as illustrated in Figure 3.5.1. In the first step, an initial nanopore device is fabricated. This initial device has a pair of microelectrodes sandwiched between dielectric passivation layers, which will form a confined cavity after wet etching. In the second step, the final nanopore is deposited via feedback-controlled electrochemical deposition, which will narrow down the gap between the microelectrode pair, forming the tunneling junction and nanopore simultaneously. In the following section, I describe this design and fabrication flow in detail.

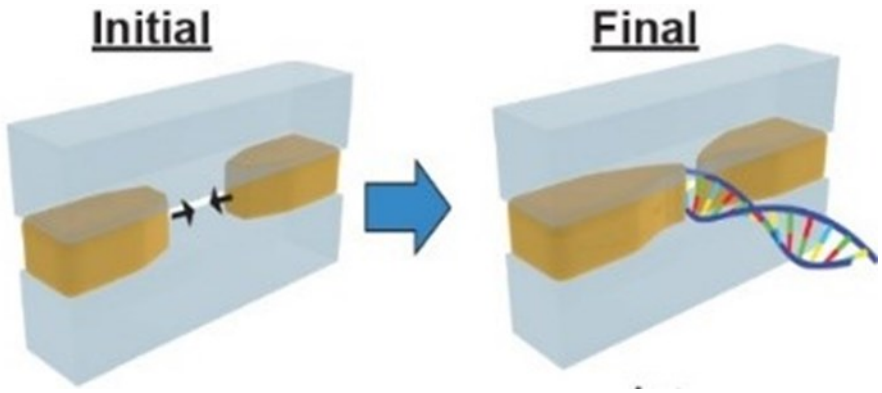

Figure 3.5.1. A schematic of the two step fabrication strategy of the planar scalable nanopore device with self-aligned transverse tunneling junction. The initial device has a pair of thin microelectrodes, with 1-μm gap, that are sandwiched between dielectric layers. The confined cavity between the microelectrode is narrowed down via electrochemical deposition, forming a tunneling junction and nanopore simultaneously.

3.5.1. Design and Fabrication of the Initial Device

The fabrication of the initial device chip is mainly based on the photolithography, which is a process to transfer desired patterns to substrates via visible or ultraviolet light in electronics manufacturing. In general, a layer of photosensitive chemical, or photoresist, is distributed on a substrate and this substrate will be exposed to light passing through a photomask. The exposed and unexposed areas will have different chemical reactions with following chemical etching treatment, leaving the desired pattern on the substrate surface. The minimum feature size of the projected pattern on the substrate is given by the following equation:

$$CD = k_1 \frac{\lambda}{NA} \tag{35}$$

where CD is the minimum feature size, or critical dimension; k_1 is a process related coefficient, typically around 0.4; λ is the wavelength of the light used; and NA is the numerical aperture of the lens as seen from the substrate. Current photolithography techniques can easily achieve micron-level accuracy, which is very helpful for our initial device chip design.

As illustrated in Figure 3.5.2, the initial device pattern is fabricated on quartz substrate due to its optimal surface roughness and material properties. In the real fabrication, both a 1 × 1 inch square, #1 thickness quartz glass slide and a 4-inch quartz wafer with 550 μm have been tested with the initial device fabrication, showing high reproducibility and device performance. Before the fabrication, the quartz substrate is cleaned with piranha—a 3:1 mixture of concentrated sulfuric acid and 30% hydrogen peroxide—to clean organic residues. There are three major steps based on the initial

device fabrication workflow, as shown in (1-4) in Figure 3.5.3. The first step is the sacrificial structure fabrication. This sacrificial structure consists of a thin central Cr layer and an overlapped thick Al layer. The Cr sacrificial layer pattern is aligned and patterned with photolithography and 20-nm-thick Cr is deposited via thermal metal evaporation. Then, a sector-shape pattern is defined via photolithography, overlapping with the edge of the Cr sacrificial layer. A 200-nm-deep SiO_2 reactive ion etching (RIE) is performed to form the guidance structure trenches in the sector-shape pattern. Then, a 240nm Al sacrificial layer is deposited in these trenches via thermal metal evaporation. To enhance the adhesion between different metal layers, a thin Cr layer—usually 1~2 nm—is applied before and after the Al sacrificial layer deposition. The second step is the transverse microelectrode fabrication. The transverse microelectrode pair is aligned with the center Cr sacrificial layer by photolithography, and 50-nm-thick Au is deposited in this patterned area via thermal metal evaporation. For the same reason, a thin Cr layer is also deposited before and after the Au deposition for a better adhesion. Third, a 100-nm-thick HfO_2 insulating layer is deposited on the surface of the substrate via ALD, covering the entire device structure. If the fabrication is done on wafers, then an additional dicing is needed to separate each device chip for the convenience of follow-up device assembly.

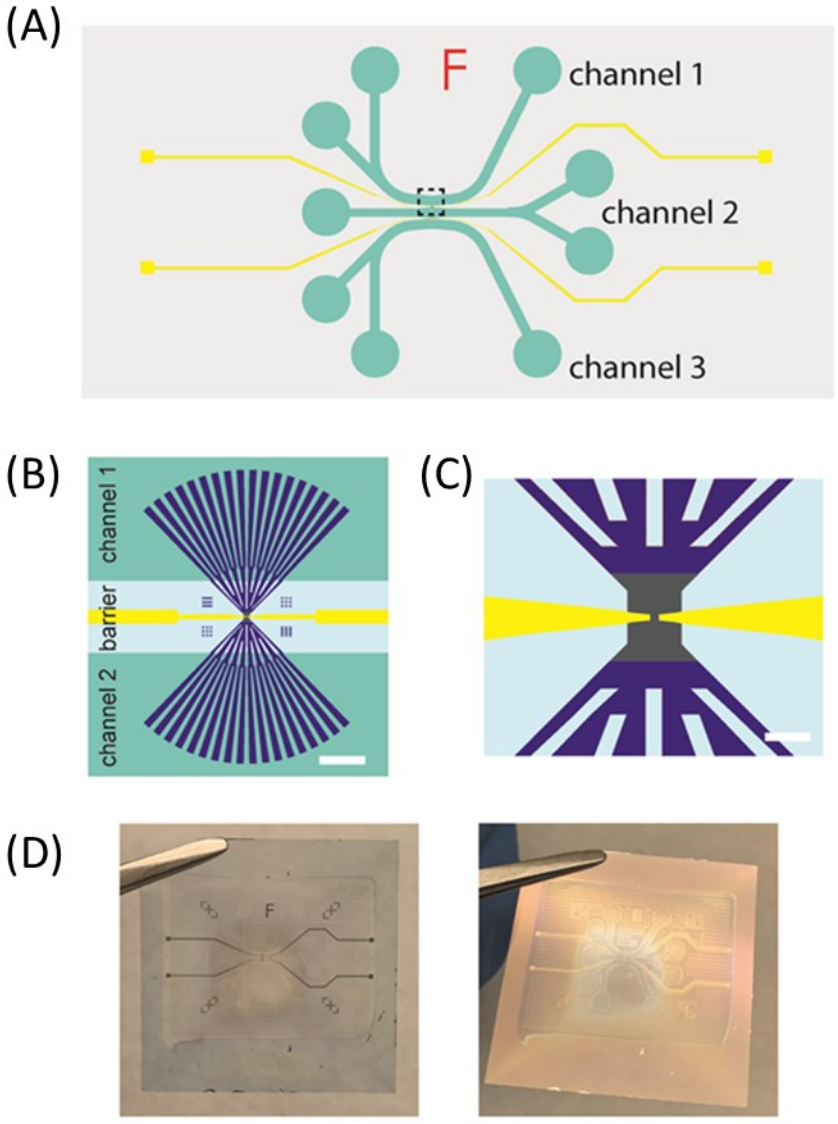

Figure 3.5.2. The design and photo of the planar nanopore device with self-aligned transverse tunneling junction. (A) A schematic of the device structure and microfluidic channels. The light green area denotes the microfluidic channel trenches defined on the initial device chip. The yellow lines represent the transverse microelectrode aligned with the center Cr sacrificial layer. (B) A close-up schematic of the sacrificial structure at the black square in (A) before wet etch. The green color is the exposed area designed for microfluidic channels shown in (A), and the light blue color is the confined area with passivation structure, which serves as a separation between two microfluidic channels. The deep blue color indicates the sector shape Al guidance structure, while the yellow lines are the transverse microelectrodes aligned with the center Cr sacrificial layer. The scale bar is 50 µm. (C) A close-up schematic of the center Cr sacrificial layer and the aligned transverse microelectrodes before wet etch. The gray color represents the center thin Cr sacrificial

layer. The blue color denotes the Al sacrificial layer. The yellow color indicates the tip of the transverse microelectrodes. The scale bar is 2 μm. (D) images of the initial device chip before PDMS sealing. Left: a top view of the chip on 1 × 1 inch square #1 thickness quartz cover slip. Right: a tilted view of the same thick under light illumination, showing the microfluidic channels trenches defined by SU8 polymer.

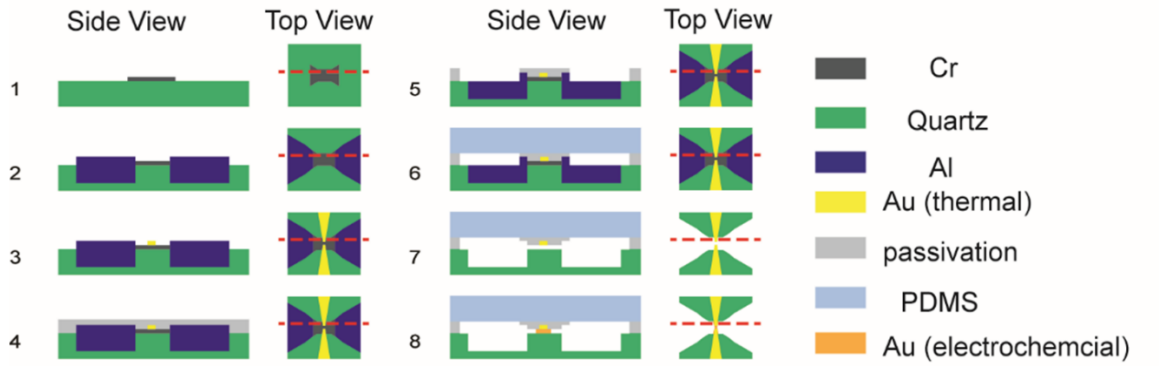

Figure 3.5.3. The schematics of the assembled device chip fabrication. (1-6) illustrate the fabrication of the initial device chip and the device assembly and (7-8) shows the final preparation of the nanopore and tunneling junction. The red dotted line marks the position of the side view. The drawing is used for structure clarification so that the geometry is not scaled. (1) The center Cr sacrificial layer with a thickness of about 10~20 nm that defines the final cavity. (2) The overlapped Al sacrificial layer with a thickness of roughly 240 nm that defines the microfluidic guidance structure connecting the planar nanopore to the *cis*- and *trans*- microfluidic channels, which are not shown here. (3) The initial Au microelectrode aligned with the center Cr sacrificial layer. The gap between their two tips is approximately 1 μm. (4) HfO_2 and SU8 passivation that seals microelectrodes and sacrificial layers. (5) Removal of the surface passivation via RIE. (6) Sealing the device chip with PDMS block to construct the *cis*- and *trans*- microfluidic channels. (7) Wet etching of Al and Cr sacrificial layers, forming the guidance structure and the center cavity. (8) Gap preparation via controlled electrochemical deposition of Au.

A major difference between our device and a conventional solid-state nanopore structure is the microfluidic guidance channel, which is the sector-shape structure in the design. A conventional solid-state nanopore consists of two separated solution reservoirs and a thin film between these two reservoirs, where the nanopore sits on the thin film and can only capture the DNA molecules close to the nanopore opening by random walking. To enhance the capture rate, straighten the long chain molecule, and enrich the molecule

density before entering the final nanopore, we designed a microfluidic guidance channel that modifies the EF profile along the nanopore. Previous experiment results have shown the stretching of DNA molecules and our recent experiment data indicates an increase in DNA molecule density before entering the final nanopore. A simulation of the EF profile is depicted in Figure 3.5.4. The fine tuning of the bias and the change of channel geometry will change the EF profile, resulting in possible interference of the molecule movement through the nanopore.

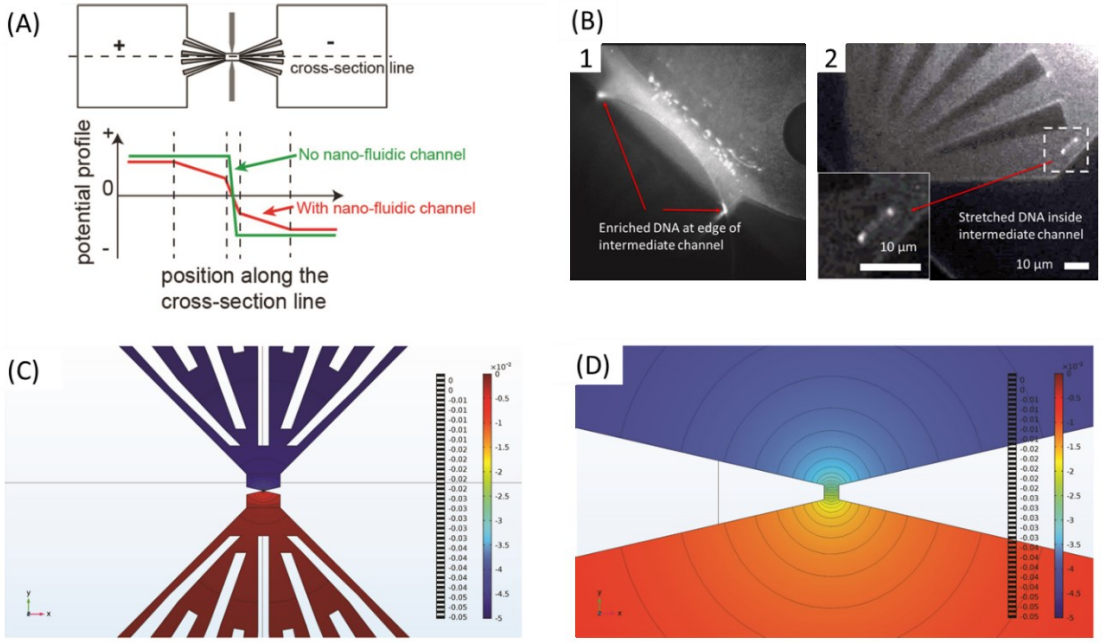

Figure 3.5.4. The electric potential profile of the planar-gated nanopore device. Based on the channel geometry design and the ionic conductivity of phosphate buffer (PB), the theoretical ionic conductance between two microfluidic chambers is 2.34 nS when channels are filled with PB. (A) A schematic of the channel design of the planar-gated nanopore device. Compared to the conventional nanopore device structure, the planar gated nanopore device embedded within microfluidic guiding channels will provide a modulated electric potential profile that stretches DNA molecules and enriches the DNA molecule concentration. (B) The fluorescence images of DNA translocation. (1) In the bulk, DNA motion is dominated by diffusion. Near the edge of the intermediate channel, the electric field (EF) becomes strong enough to significantly attract the DNA. There is an energy

penalty for the DNA to unwind and enter the height-constricted channel; therefore, DNA clusters near the edge. (2) Inside the intermediate channel, double-stranded DNA is forced to unwind and stretched. Experiment jointly conducted with Joshua Sadar. (C) Simulation of the electric potential in the microfluidic guiding channels when a constant cross-chamber voltage is applied. It shows the electric potential profile in a color scale and labels equal potential lines. The trans- chamber (the upper chamber) is grounded and the cis-chamber (the lower chamber) is at -50 mV. (D) Simulation of the electric potential profile at the nanopore (cross section of 20 nm × 20 nm). The EF increases gradually based on the microfluidic channel design. The simulation is done with COMSOL Multiphysics® version 5.3.

3.5.2. Nanopore Device Assembly

With respect to the basic structure paradigm of a nanopore device, it is usually consists of a nanopore and two reservoir chambers. For our planar nanopore device, the initial chip requires two confined microfluidic channels to construct the reservoir chambers. In our practice, a polydimethylsiloxane (PDMS) top piece with microfluidic patterns is used to constructing such reservoir chambers. Four steps are involved in the microfluidic nanopore device assembly, simplified as (5) and (6) in Figure 3.5.3. The first step is the fabrication of microfluidic channel trenches on the initial device chip. A photoresist layer is spin-coated on the surface of the initial device chip, and it is patterned with the microfluidic channel pattern aligned with the sacrificial structure, as illustrated in Figure 3.5.2A. Then a RIE process is performed to selectively remove HfO_2 through the photoresist microfluidic channel pattern. After the RIE, the 100-nm HfO_2 passivation layer is complete removed and the Al sacrificial layer is partially exposed. The second step is the fabrication of the SU8 polymer supporting structure. Due the requirement of good sealing, the SU8 polymer supporting structure is fabricated after the photoresist removal, following a modified low-stress protocol. The initial device chip is rinsed with acetone and isopropyl alcohol (IPA) and treated with a mild oxygen plasma treatment for

1~2 min to remove possible organic residues. It is then based at 180 ℃ for 30 min before SU8 coating. SU8 2025 is spin-coated for 40 s at 2000 rpm on the initial device chip and baked at 57 ℃ overnight to remove the solvent, forming a 50-μm-thick SU8 polymer layer. This SU8 layer is pattern with the same microfluidic channel pattern via photolithography, which is aligned with the microfluidic channel trenches made on the HfO_2 passivation layer. After the exposure, a post exposure bake (PEB) is performed at 57 ℃ for 1 h with a slow ramping rate. Then, the patterned SU8 polymer is developed in SU8 developer for 10 min, followed by two gentle rinses in IPA and one gentle rinse in Milli-Q water, and the initial device chip is air-dried in a clean environment. Last, to cure the SU8 polymer without creating cracks, the initial device chip is hard-baked at 180 ℃ in an oven for 1 h with a slow ramping speed. To create reliable bonding between the PDMS microfluidic top piece and the SU8 supporting layer, the initial device chip is functionalized with (3-Aminopropyl)triethoxysilane (APTES) by immersing the chip in a 5% (v/v) APTES ethanol solution for 20 min immediately after a 2 min oxygen plasma treatment, followed by a 95% ethanol rinse and a dehydration bake at 120 ℃ for 30 min. The device chip after this step is depicted in Figure 3.5.2D. The third step is the fabrication and sealing of the PDMS microfluidic top piece, which is a block of 0.5×1×1 cm^3 (H×W×L) cut from a flat PDMS sheet. This top piece is punched with nine holes according to the inlet/outlet location based on the microfluidic channels pattern. Before sealing the PDMS top piece with the SU8 polymer supporting structure, the block is sonicated in ethanol for more than 30 minutes to remove possible particle debris. The block is then aligned and placed on the SU8 polymer supporting structure on the initial device chip with liquid PDMS as sealant. This assembled device chip is then baked at

120 ℃ in an oven for 1 h with a slow ramping speed to cure the liquid PDMS, sealing the microfluidic channels without structure deformation. In the fourth step, the device chip is finally assembled. The device chip sealed with the PDMS block is fixed by Poly(methyl methacrylate) (PMMA) on the center area of a customized PCB, which has multiple outlet connections enabling easy integration with external instruments. The microelectrodes are connected with the PCB connections via wire bonding. Polyethylene (PE) tubing is connected with the punched hole on the PDMS block. After these four steps, the assembled device chip is ready for microscopy mounting and connections to pumping system and electronics, as shown in Figure 3.5.5.

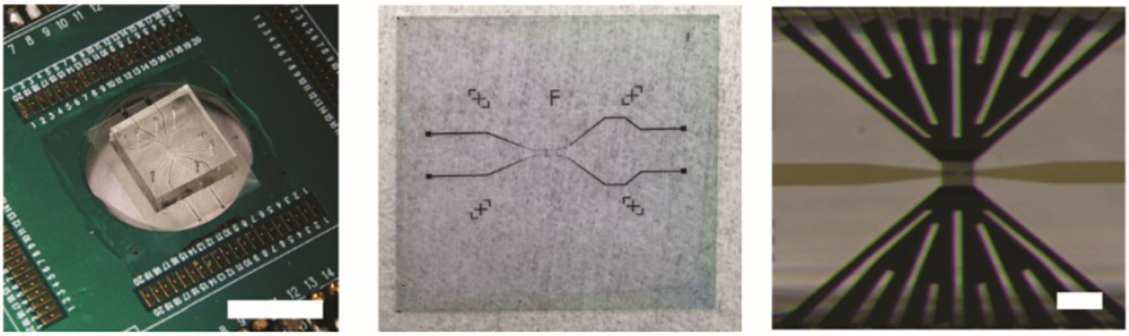

Figure 3.5.5. Images of the device assembly and device chip. Left: image of the assembled device chip fixed on the optical access of the customized PCB. The scale bar is 1 cm. Middle: image of a device chip on a tissue paper. This chip is fabricated on a 1 × 1 inch square, #1 thickness quartz cover slip. Right: a magnified image of the initial nanopore device before wet etching. The scale bar is 10 μm.

3.5.3. Initial Nanopore Device Formation via Wet Etching

As demonstrated in the previous section, the initial nanopore device is fabricated with sacrificial structure shown as the left image of Figure 3.5.5. In order to open the access to the center cavity and initial microelectrodes, a three-step wet etching process is

applied after the assembled device is connected to the syringe pump and external electronics. The first wet etching is performed to remove the Cr adhesion layer on top of the Al sacrificial structure by pumping in a commercial chromium etchant (Sigma-Aldrich, SKU 651826) for 10 min. The purpose of the second wet etching is to remove the Al sacrificial structure by pumping in a commercial aluminum etchant (Transene, Al etchant type D). The etching time varies in hours due to the very small liquid access when etching the sacrificial structure under the HfO_2 passivation. Thus, the system will be left in the etchant overnight until the Al sacrificial structure is etched completely. In the third wet etching, the center Cr sacrificial layer is removed to form the confined cavity for nanopore preparation by pumping the chromium etchant. The complete Cr etch and a disconnection between the pair of microelectrodes aligned with the center Cr layer would normally take 30 minutes to one hour. Between each step discussed in this section, a 1-h Milli-Q water flushing is applied in order to remove etchant residue, avoiding the precipitation when different etchants are mixed.

To better understand the performance of the sealing and etching, the ionic conductance is measured before and after the wet etching. A phosphate buffer (PB) consisting of 5 mM KH_2PO_4 and 5 mM Na_2HPO_4 is pumped into the channels as the electrolyte for the ionic conductance measurement. A source measurement unit (Keithley, Model #: 2636B) is connected to two microfluidic channels of the target device via agar gel Ag/AgCl salt bridge reference electrodes. The ionic conductance is usually silent at tens of pS before wet etching, and it increases to 2~6 nS when the wet etching finishes. Figure 3.5.6 presents a typical scan of ionic current vs applied voltage before and after the wet etching.

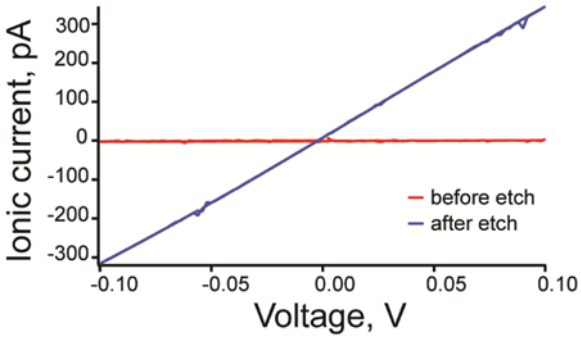

Figure 3.5.6. IV scan in PB between two microfluidic channels before and after the sacrificial structure wet etching. The ionic conductance in PB is 28 pS and 3.3 nS before and after the wet etching, respectively.

At the same time, an estimation calculation of the total resistance of ionic channels is also demonstrated. The PB solution conductivity is given by:

$$\kappa = \sum \Lambda_i \cdot C_i = 0.162\ S/m \tag{36}$$

where Λ_i and C_i are the molar conductivity and the concentration of ion i in the solution, respectively.

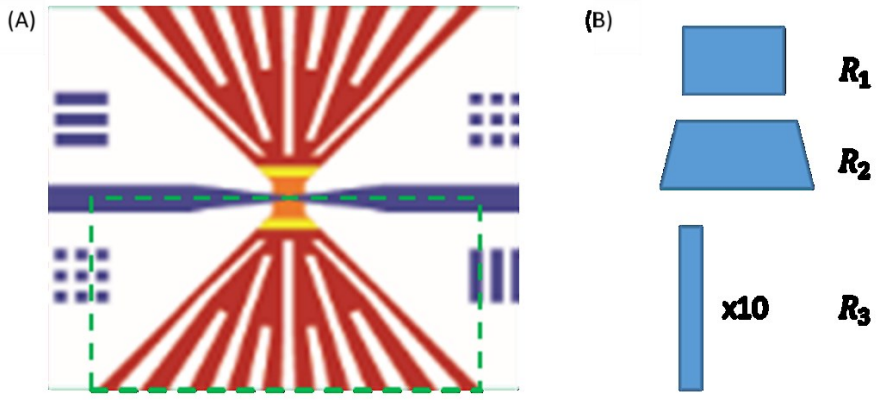

Figure 3.5.7. A simplified model for ionic current estimation. (A) A top view of the nanopore device channel confined by a HfO_2 passivation layer. The green dashed rectangle

shows the guidance structure at one side of the nanopore. (B) The simplified resistors in the green dash rectangle in (A) before electrochemical deposition. It is simplified as three series connected resistors. R_1: a cuboid of 6 μm × 3 μm × 20 nm (W×L×H). R_2: a trapezoidal body with a constant cross section height H of 240 nm, a length L of 5 μm, a starting width W_1 of 16 μm and a final width W_2 of 6 μm. R_3: 10 parallel connected cuboids of 3 μm × 32 μm × 240 nm (W×L×H).

Regarding its geometry before electrochemical deposition, the resistance of the guidance structure at one side can be simplified as series resistors, depicted in Figure 3.5.7. $R_1$is a cuboid of 6 μm × 3 μm × 20 nm (W×L×H). R_2 is a trapezoidal body with a constant cross section height H of 240 nm, a length L of 5 μm, a starting width W_1 of 16 μm and a final width W_2 of 6 μm. R_3 consists of 10 parallel connected cuboids of 3 μm × 32 μm × 240 nm (W×L×H). Thus, the total resistance of one side's guidance structure is given by

$$R_{g1} = \sum \frac{L_j}{W_j H_j} \cdot \frac{1}{\kappa} = 206.9\ M\Omega \tag{37}$$

where j denotes different components of the guidance channel structure. The total conductance between two microfluidic channels before electrodeposition is therefore

$$G_{before} = \frac{1}{2R_{g1}} = 2.42\ \text{nS} \tag{38}$$

Comparing the experiment results and the estimation, our structure sealing and wet etching demonstrate high performance and consistency in experiments.

3.5.4. Feedback-Controlled Electrochemical Deposition of the Final Nanopore

Unlike other solid-state nanopores based on FIB, EBID, and electromigration, our design uses a feedback-controlled electrochemical deposition to narrow down the initial gap, forming the nanopore and the tunneling junction simultaneously. An electrochemical

process is a process caused or accompanied by an electric current and involving an electron transfer process at the interface between a solid and a liquid. This electron transfer process could change the oxidation state of the atoms, ions, and molecules involved in the electrochemical reaction, and reactions occurring at the interface can be tuned via the change in applied potential. For a given electrochemical system, the equilibrium state of the reaction can be calculated based on the Nernst equation, which is given as:

$$E = E^0 - \frac{RT}{nF}\ln(\frac{C_r}{C_o}) \tag{39}$$

where E is the system potential under certain concentration, E^0 is the potential when the concentrations of oxidized and reduced species are equal, R is the gas constant, T is the absolute temperature, n is the number of moles of electrons exchanged in the reaction, F is Faraday's constant, C_o is the concentration of oxidized species, and C_r is the concentration of reduced species.

In our experiment, CV is an important method to determine the potentials required for oxidation and redox reactions. To conduct a CV scan, the potential of one electrode sweeps in a given range and the current collected by the other electrode is measured. By plotting the current vs the potential, the curve will show peaks when the active species are oxidized or reduced at certain potentials. These potentials actually offer guidance to set the potential range that can be used for controlling the deposition and removal of the metal at the microelectrodes. Before starting the electrochemical deposition, a series of CV scans are demonstrated to understand the correct potential range. As illustrated in Figure 3.5.8, after demonstrating that the measurement is working

properly in a standard CV system, ferrocyanide/ferricyanide, the CV scan between a gold electrode and a gold deposition solution is demonstrated. The utilized gold deposition solution used consists of 18 mM $KAu(CN)_2$ and 180 mM K_3Citrate and the CV scan suggests a redox peak of Au ranging from 600 mV to 700 mV and an oxidation peak of Au between 800 mV to 900 mV.

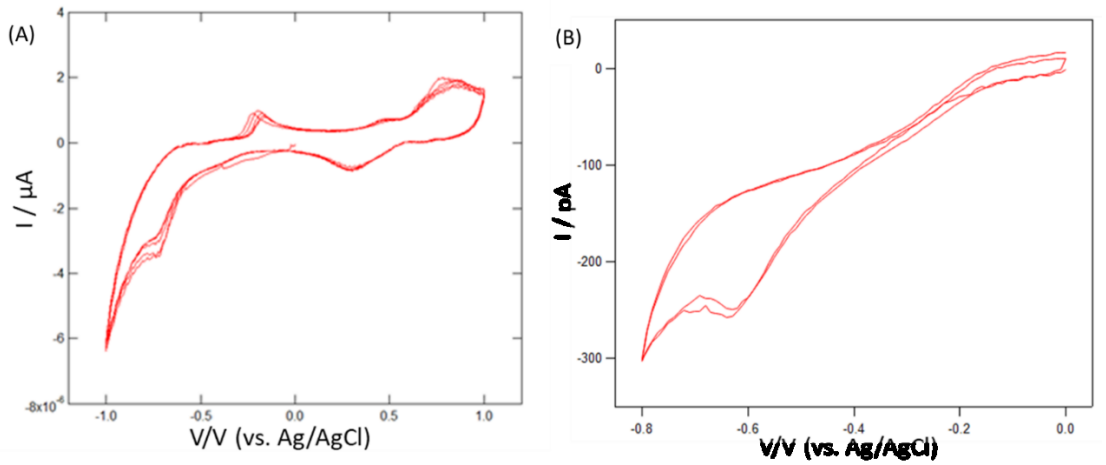

Figure 3.5.8. Cyclic voltammetry (CV) scan of deposition solution and Au electrodes. (A) The CV scan of the deposition solution and electrodes with a large surface area. (B) The CV of deposition solution and microelectrodes. Experiment conducted by Joshua Sadar.

Once the correct potential is found for the metal deposition. The next step is to setup the circuit for electrochemical deposition. In our design, both ionic current and tunneling current are measured to understand the real-time deposition status in the center cavity. Thus, two complete circuits are defined to monitor these two currents simultaneously.

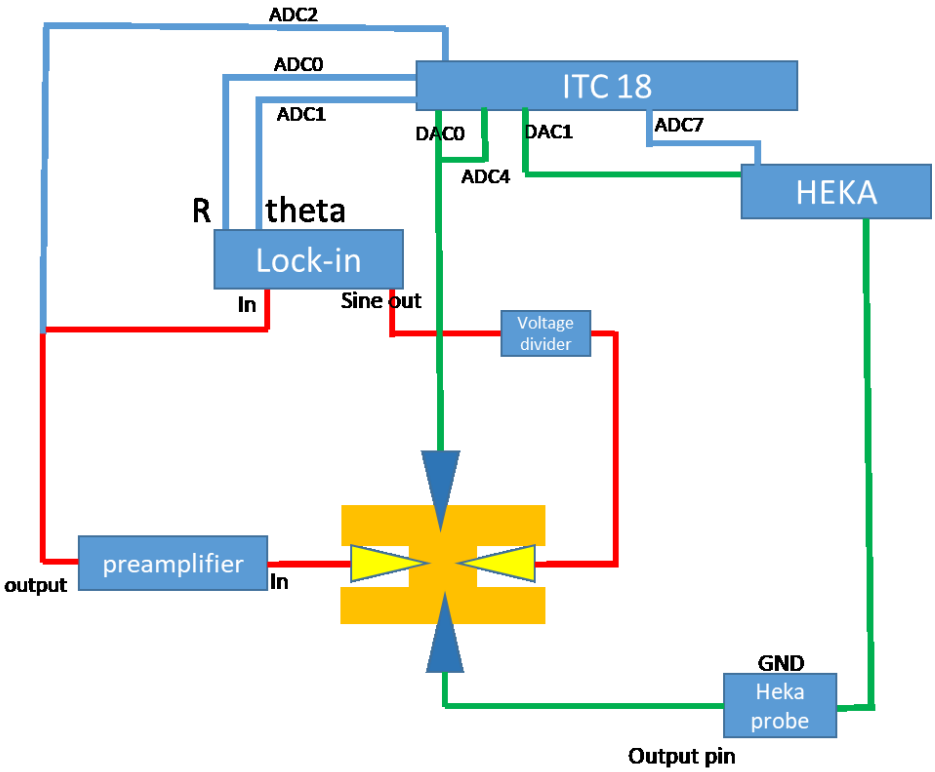

Figure 3.5.9. The schematic circuit for the feedback controlled electrochemical deposition of the final nanopore. The red line denotes the tunneling current monitoring circuit. The green line denotes the ionic current monitoring circuit. The blue line denotes the data collection circuit. The orange area denotes the initial center cavity and two microfluidic channels. The tunneling current is measured by the preamplifier connected with the microelectrode, labeled as yellow triangles. The ionic current is measured by HEKA patch clamp amplifier, which connects to the microfluidic channel via an agar gel Ag/AgCl reference electrode. Deposition pulses in two microfluidic channels are applied by ITC18 data acquisition interface. The raw data, amplitude, and phase of the tunneling current and the raw data of the ionic current are collected by ITC 18 data acquisition interface.

The schematic of the electrochemical deposition circuit is presented in Figure 3.5.9. In general, the entire metal deposition circuit consists of two components. The first is the tunneling current monitoring circuit, indicated in red. An AC reference signal is applied to one transverse microelectrode through a voltage divider from a lock-in amplifier. The other microelectrode is connected to the preamplifier, which outputs a

tunneling current signal to the lock-in amplifier input. Then the amplitude and phase information of the tunneling current will be calculated by the lock-in amplifier and collected by the ITC 18 data acquisition interface. The second component is the ionic current monitoring circuit, labeled in green. In this circuit, the two microfluidic channels are connected to the ITC 18 data acquisition interface and HEKA patch clamp amplifier via two agar gel Ag/AgCl salt bridge reference electrodes. The ionic current is measured by the patch clamp amplifier when a bias is applied between the two microfluidic channels via the reference electrodes. The raw data of the ionic current are also collected by the ITC 18 data acquisition interface. During the deposition, the gold deposition solution is slowly pumped through the two microfluidic channels connecting the initial nanopore device, which is marked in orange. An AC bias with a low amplitude is applied between the transverse microelectrode pair, and the tunneling current in between is monitored as a parameter symbolizing how close the deposited gap is. The deposition pulses encouraging the redox reaction of Au on the microelectrode surface are applied to one of the microfluidic channel via the signal output on the ITC 18 data acquisition interface. Meanwhile, another pulse signal, which has a 50-mV difference from the deposition pulse, is applied in the other microfluidic channel via the patch clamp amplifier probe. The ionic current measured by the patch clamp amplifier is thus used as a parameter symbolizing the narrowing down of the center cavity cross section.

The deposition process is controlled by a customized Igor program, which changes the deposition pulse according to the change in the tunneling current amplitude or tunneling conductance. When the tunneling conductance increases to a certain threshold, typically one tenth of the quantum conductance $G_0 = \frac{2e^2}{h} = 77.5\ \mu S$, the

program will change the deposition pulse width to slow down the deposition. When the tunneling conductance increases to this threshold, the deposited gap normally has a trend to close up and the tunneling conductance would reach one or multiple times of G_0 in several deposition cycles. The program will change the deposition pulse to an oxidation pulse to remove the newly deposited gold on the microelectrode tips and open the gap. At present, the program will decrease the tunneling conductance to a stable value, typically below half G_0. The tunneling conductance is then tuned to around 1 nS by manually applying oxidation pulses in order to reach the readout level of typical scanning tunneling microscopy (STM).

With this feedback-controlled deposition method, the nanopore size and the microelectrode gap size can be reversibly controlled. During the electrochemical deposition process, the ionic current between two microfluidic channels slowly decreases, while the tunneling conductance between the transverse microelectrodes remains at a low level and will increase sharply when the deposited gap is close enough. Figure 3.5.10 depicts a close-up of the ionic channel close up and the narrowing down of the tunneling gap. In some experiments, the center cavity can be closed completely, giving an ionic conductance around 10 pS in the deposition solution. Therefore, based on the control program it is possible to perform multiple closing and opening of the deposited gap between the transverse microelectrodes (Figure 3.5.10D).

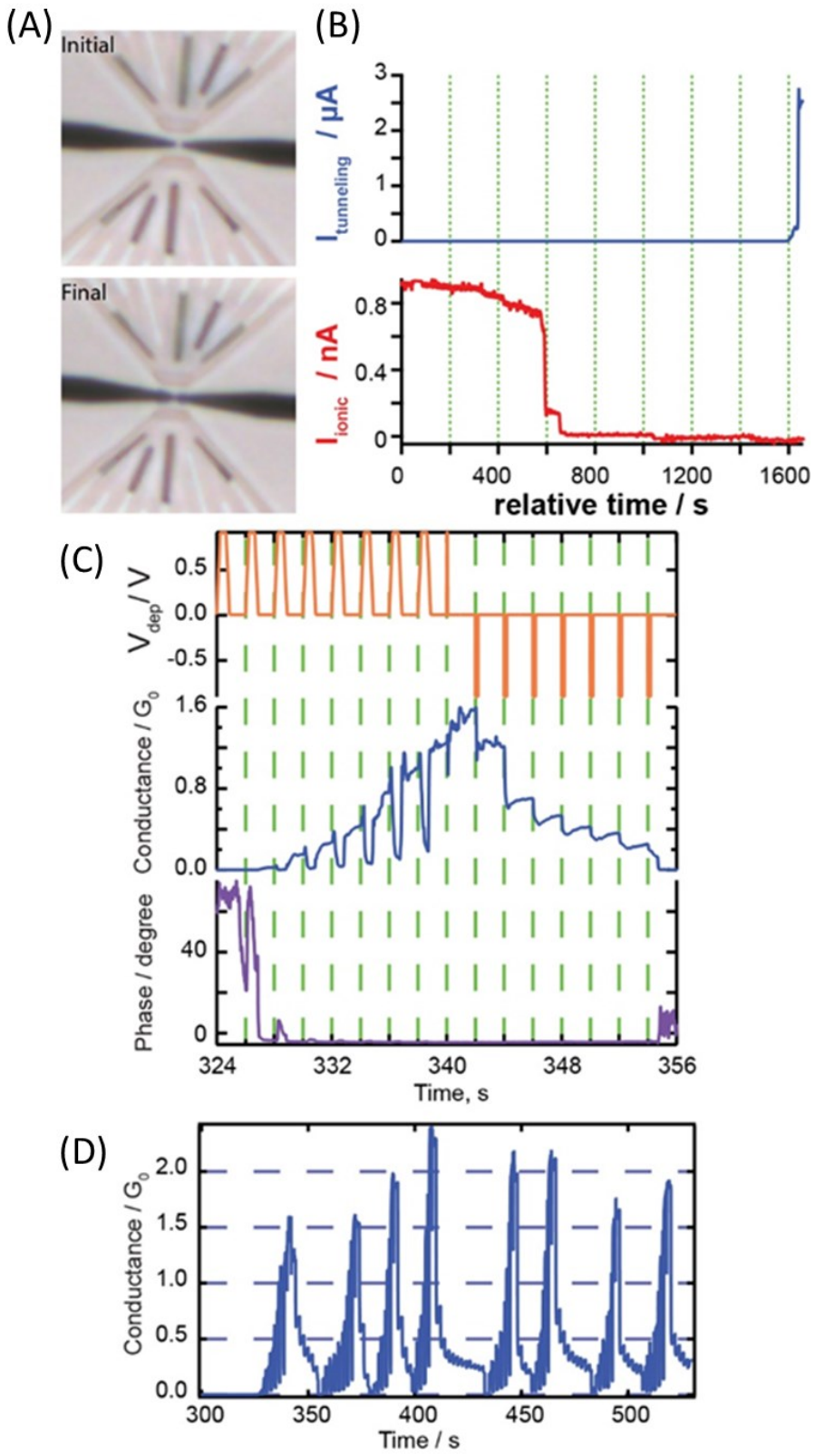
(A)
Initial
Final
(B)
$I_{tunneling}$ / μA
I_{ionic} / nA
relative time / s
(C)
V_{dep} / V
Conductance / G_0
Phase / degree
Time, s
(D)
Conductance / G_0
Time / s

Figure 3.5.10. Nanopore and tunneling junction size control via feedback controlled electrochemical deposition. (A) Optical images of the initial transverse microelectrodes (top) before and (bottom) after the electrochemical deposition when the gap is closed. (B) Simultaneous recordings of ionic and tunneling currents as the quantum contract occurs. The tunneling current $I_{tunneling}$ is measured between the transverse microelectrodes under an AC bias of 1.45 mV and a frequency of 10.13 kHz. The ionic current I_{ionic} is measured between the two microfluidic channels under a DC bias of 50 mV. Note that the ionic current drops first, and the tunneling current increase later, creating a short between the transverse microelectrodes. (C) The controlled deposition control via the customized program. The amplitude and phase of the tunneling conductance between the transverse microelectrode recorded at 10.13 kHz change when the Ag/AgCl reference electrodes apply pulses encouraging Au deposition (V_{dep} = 950 mV) and dissolution (V_{dep} = -1 V). When the tunneling conductance reaches a threshold above 1 G_0, the program will switch the pulse shape to remove Au from the microelectrode. (D) Tunneling conductance between transverse electrodes during the controlled reversible closing and opening of the tunneling junction for multiple times.

In addition to the potential applied in the microfluidic channels would encourage Au deposition and dissolution differently, the wave form will affect the growth of deposited Au on the transverse microelectrodes (Figure 3.5.11). In our experiment, a constant deposition bias will cause a serious side growth of the transverse microelectrodes, resulting in a very slow deposition on forming the quantum contact between the transverse microelectrodes. This is because of the rapid exhaust of $Au(CN)_2^-$ ions near the tips of the transverse microelectrodes in the confined center cavity. When a constant deposition voltage is applied, the deposition occurs mostly on the outer edge of the microelectrodes that are exposed to fresh ion supply due to diffusion and electrophoresis, resulting in less deposition taking place at the microelectrode tips. Thus, a deposition potential is applied in a pulsed form to attain an effective deposition for closing the gap between the transverse microelectrodes. In the experiments, the deposition potential is only applied for a short period of time, and the system then applies

a “rest” potential, which generates no redox reaction, to allow for the restoration of ion concentration between the transverse microelectrodes. The optimal pulse wave form is defined as a combination of a deposition potential which lasts for 2 to 50 ms and a rest potential period around 2 s after a systematic deposition tests with various wave form.

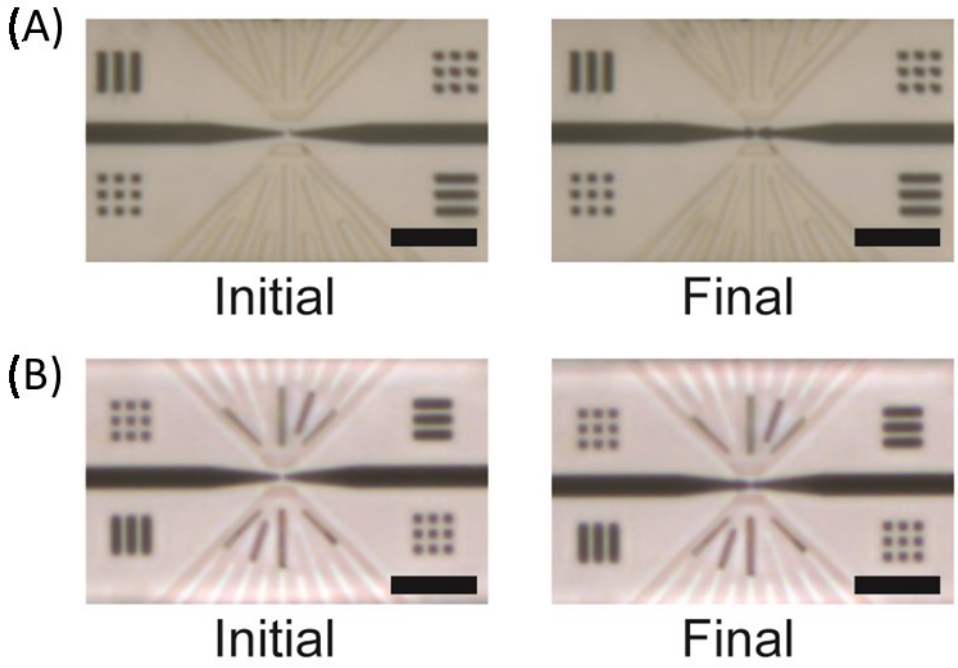

Figure 3.5.11. Key frames of time lapse recording during electrochemical depositions with different deposition pulse wave forms. (A) The optical images of the transverse microelectrodes before and after the metal deposition with the deposition pulse consisting of a 400 ms 950 mV square wave followed by a 1.6 s 0 V rest potential. (B) The optical images of the transverse microelectrodes before and after the metal deposition with the deposition pulse consisting of a 2 ms 950mV square wave followed by a 1.998 s 500 mV rest potential. The final deposited tip exhibits less side growth and fast tip deposition when a short deposition pulse width and a higher rest potential exist. The scale bar is 20 μm.

The feedback control signal applied between the transverse microelectrodes is used for the monitoring of the tunneling conductance to track the gap development of the

tunneling junction. In our experiments, AC signal frequencies ranging from 1 Hz to 10 kHz were tested. When a higher frequency is used, the tunneling conductance starts to display clear phase changes at a large gap size around tens of nm due to the capacitive component of the tunneling current [139, 140]. A higher frequency offeres a wider range for controlling the tunneling junction distance. As illustrated in Figure 3.5.10C, the phase of the tunneling conductance changes from capacitive-dominated to resistive-dominated before the significant increase in the tunneling conductance. In our practice, the high frequency feedback control signal is used for the initial electrochemical deposition. However, to reach the diameter of DNA molecules, a low frequency AC feedback control signal at 5 Hz is used during the manual tuning to monitor and control the junction size which is sensitive in the tunneling region. As mentioned previously, the tunneling conductance at the deposited junction is stabilized at around 1 nS.

3.5.5. Deposited Nanopore and Tunneling Junction Size Estimation

Since it is difficult to take a transmission electron microscopy (TEM) directly after the formation of the tunneling junction, a gap size estimation is helpful for us to understand the deposition.

For the nanopore size, its height is confined by the device structure and its width can be estimated using a similar model discussed in the estimation of ionic conductance after wet etching. After the deposition, the resistance of the guidance structure at one side can be simplified as he following series resistors (Figure 3.5.12): first, R_1', which is a trapezoidal body with a constant cross section height H_0 of 20 nm, a length L_0 of 1 μm, a starting width d and a final width W_0 of 6 μm; R_2', which is a cuboid of 6 μm × 2 μm × 20 nm (W×L×H); third, R_3', which is a trapezoidal body with a constant cross section

height H of 240 nm, a length L of 5 μm, a starting width W_1 of 16 μm, and a final width W_2 of 6 μm; and fourth, R_4', consisting of 10 parallel connected cuboids of 3 μm × 32 μm × 240 nm (W×L×H). Thus, the total resistance of one side's guidance structure is the sum of the resistance of different components:

$$R_{g2} = \sum_k R_k' \tag{40}$$

where *k* is the labeling of the different resistor components. Based on the calculation, the final resistance after deposition is related to the resistance of the resistor R_1'. Consider the geometry of R_1' and assume that *d* is small compared to W_0, the R_1' resistance is the given by

$$R_1' = \frac{1}{6H_0\kappa} ln\left|\frac{6L_0}{d} + 1\right| \tag{41}$$

The R_1' resistance is thus related to the value of *d,* and the total conductance in PB after deposition is given by:

$$G_{after} = \frac{1}{2(R_{g2} + R_1')} \tag{42}$$

A plot of the total conductance in PB after deposition and different gap size is illustrated in Figure 3.5.13. Assuming that *d* = 1 nm, 10 nm, and 100nm, the total conductance between two microfluidic channels after deposition G_{after} is 0.83 nS, 1.03 nS and 1.36 nS, respectively. This simplified model still requires additional information to yield a better estimation; nevertheless, it provides an indication of the how the ionic current changes when the final nanopore gap size varies.

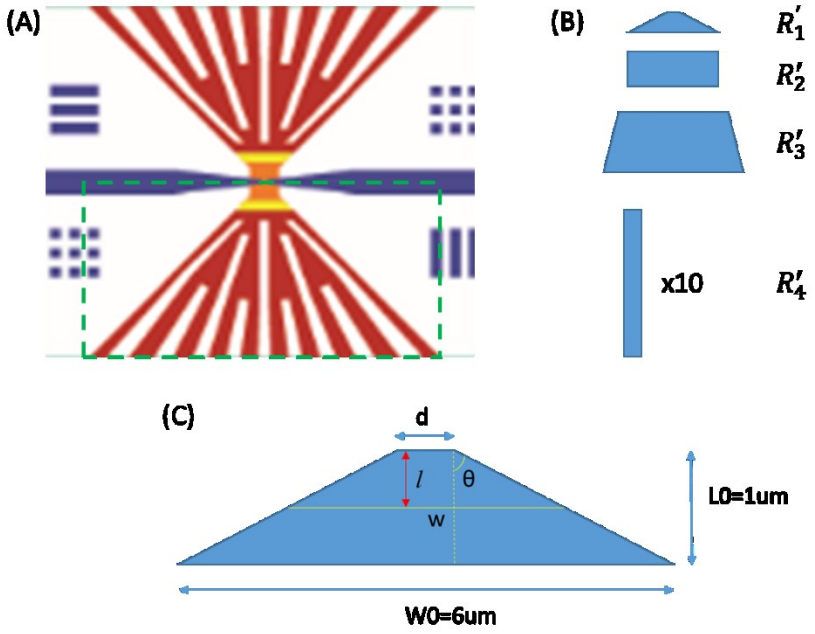

Figure 3.5.12. A simplified model for ionic current estimation after deposition. (A) A top view of the nanopore device channel confined by HfO_2 passivation layer. The green dashed rectangle indicates the guidance structure at one side of the nanopore. (B) The simplified resistors in the green dashed rectangle in (A) after electrochemical deposition. The total resistance is simplified as four series connected resistors. R_1': A trapezoidal body with a constant cross section height H_0 of 20 μm, a length L_0 of 1 μm, a starting width *d* and a final width W_0 of 6 μm. R_2': a cuboid of 6 μm × 2 μm × 20 nm (W×L×H). R_3': a trapezoidal body with a constant cross section height H of 240 nm, a length L of 5 μm, a starting width W_1 of 16 μm and a final width W_2 of 6 μm. R_4': 10 parallel connected cuboids of 3 μm × 32 μm × 240 nm (W×L×H). (C) The geometry for the integral of R_1'. The resistance of a thin slice with a length *dl* is $dR = \frac{1}{\kappa}\frac{dl}{H*w}$. Assuming the start width d for the integral is small compared to the end width W_0, the width of the thin slice *w* is *d*+6*l*. The integral starts from 0 to L_0 and the final equation of R_1' is $\frac{1}{6H_0\kappa} ln\left|\frac{6L_0}{d}+1\right|$.

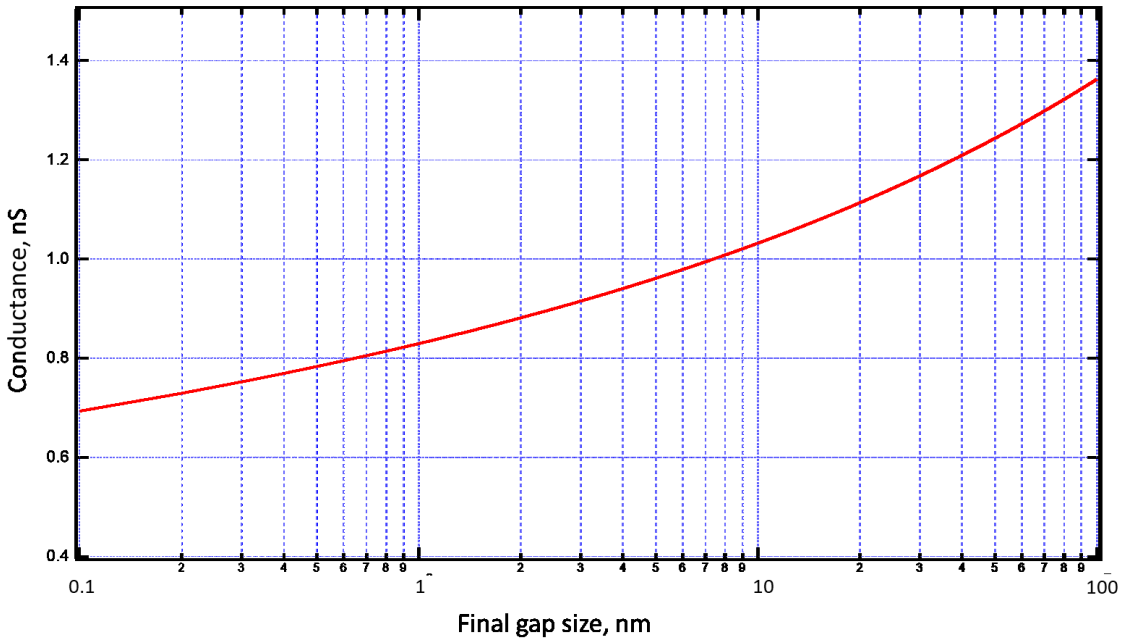

Figure 3.5.13. The total ionic conductance between two fluidic chambers in PB of the deposited nanopore with different gap size.

For the tunneling junction gap size, our transverse microelectrode pair can be simplified as a typical scanning tunneling microscope. The tunneling current $I_{tunneling}$ is given by the equation

$$I_{tunneling}(d) = Cq_eVe^{-2\frac{\sqrt{2m_e\phi}}{h}d} \tag{43}$$

where d is the gap distance, C is constant, q_e is the electron charge, V is the applied voltage, m_e is the electron mass, ϕ is the work function of gold, and h is the Planck constant. Thus, the tunneling conductance is

$$G_{tunneling} = Cq_e e^{-2\frac{\sqrt{2m_e\phi}}{h}d} \tag{44}$$

Since the quantum contact occurs when the gap is 2 Å based on Smith's experiment in 1995 [141] and the quantum conductance is 77.5 μS. the nanogap distance can be calculated by the following relation

$$G(d) = G_0 \exp[-3.57 \times 10^9 (d - d_0)] \quad (45)$$

where G_0 is the quantum conductance, and d_0 is the distance when Au-Au quantum conductance takes place. Based on our measurement, the tunneling conductance of the final nanogap G_{gap} is approximately 1nS at 5 Hz. Thus the gap distance is therefore

$$d_{gap} = d_0 + \frac{ln(G_{gap}/G_0)}{-3.57} = 3.4\ nm \quad (46)$$

This value is close to the DNA molecule diameter of 2 nm, demonstrating that the tunneling junction preparation method is capable of controlling the gap size for the subsequent DNA translocation experiments.

3.6. DNA Translocation with Planar Nanopore Device

After the nanopore and tunneling junctions are prepared simultaneously, a PB solution is pumped through the microfluidic channels to remove the residue of the deposition solution. The surface of the transverse microelectrodes are modified with poly(ethylene glycol) methylether thiol (PEG thiol, Sigma-Aldrich) overnight by flowing 50 μM PEG thiol aqueous solution with a 500-mV bias applied between two microfluidic channels. The tunneling conductance before and after the PEG thiol surface modification remains at a similar level, demonstrating that there is no significant degradation of the newly deposited tunneling junction (Figure 3.6.1).

The circuit for the DNA translocation test is illustrated as Figure 3.6.2. The entire circuit consists of two components. The first component is the ionic current measurement circuit. Two agar gel Ag/AgCl salt bridge reference electrodes are connected to the *cis*- and *trans*- chambers on the two sides of the nanopore. The *cis*- chamber is connected to negative bias and the *trans*- chamber is grounded by the HEKA patch clamp amplifier via

reference electrodes. DNA molecules are thus driven from the *cis*- chamber to the *trans*- chamber because DNA molecules are negatively charged. The ionic current is recorded by the patch clamp amplifier. The second component is the tunneling current measurement circuit. The two sides of the newly deposited tunneling junction are connected to a lock-in amplifier, and a preamplifier. A low frequency small bias is applied to one side of the tunneling junction via the lock-in amplifier and the preamplifier records the tunneling current across the tunneling junction. The raw data, amplitude, and phase of the tunneling current and the raw data of the ionic current are recorded by the ITC 18 data acquisition interface. During the DNA translocation, the syringe pump is turned off to avoid interference on the signal via mechanical vibration. The entire measurement system is also properly shielded with copper mesh to prevent electromagnetic interference from the environment.

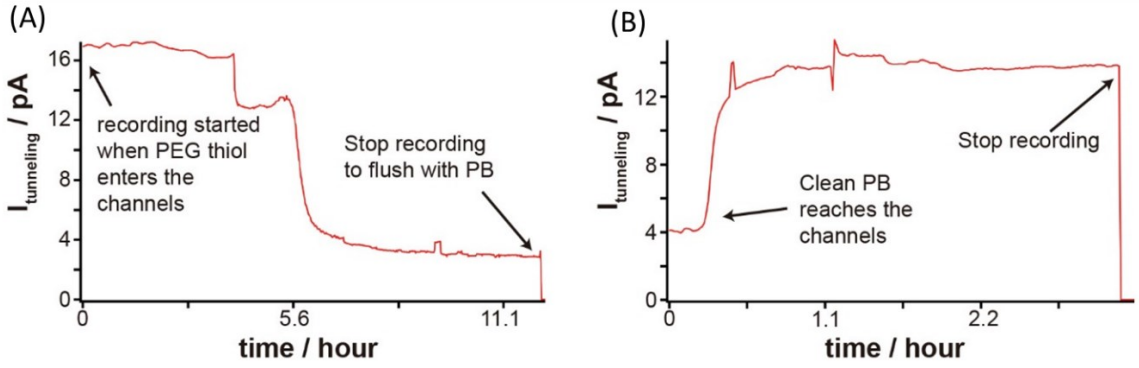

Figure 3.6.1. The amplitude and phase monitoring traces of the tunneling current during (A) the PEG thiol surface modification and (B) PB flushing after PEG thiol surface modification. During the PEG thiol surface modification, both channels are filled with PEG thiol, and a 500 mV bias is applied between two microfluidic channels to encourage the flow through the nanopore.

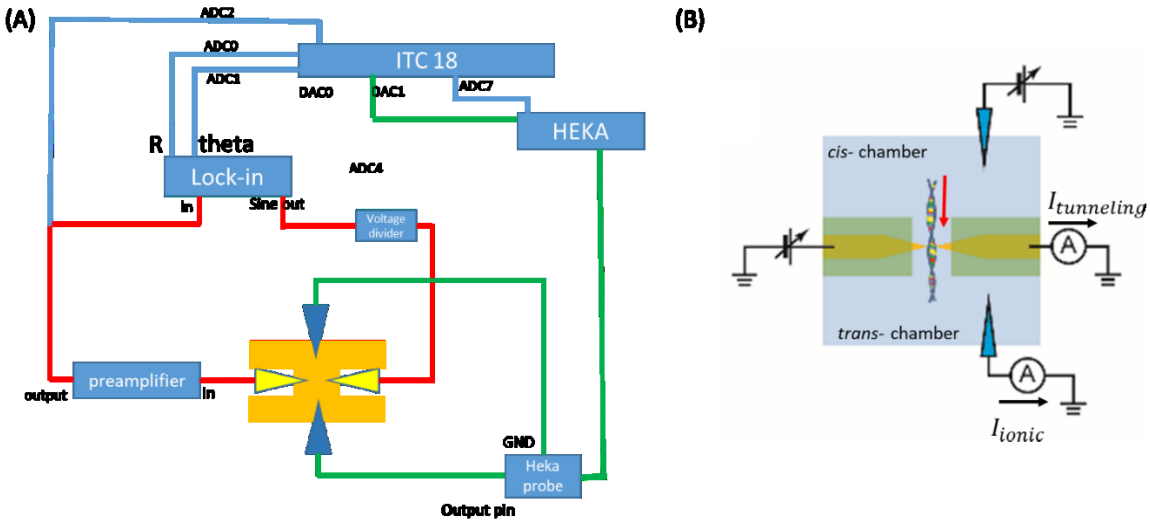

Figure 3.6.2. (A) The circuit for DNA translocation. The red line denotes the tunneling current monitoring circuit. The green line denotes the ionic current monitoring circuit. The blue line denotes the data collection circuit. The orange area denotes the nanopore and two microfluidic channels. The tunneling current is measured by the preamplifier connected with the microelectrode, labeled as yellow triangles. The ionic current is measured by HEKA patch clamp amplifier, which connects to *cis*- and *trans*- chambers via an agar gel Ag/AgCl reference electrode. The raw data, amplitude and phase of tunneling current and the raw data of the ionic current are recorded by ITC 18 data acquisition interface. (B) A schematic of the DNA translocation at the nanopore device. DNA molecules are driven from the *cis*- chamber to the *trans*- chamber by a cross-chamber bias. A small bias is simultaneously applied at the deposited tunneling junction.

To perform the DNA translocation, the *cis*- chamber of the nanopore device is filled with lambda DNA solution, which is prepared from commercial products (Sigma-Aldrich) with filtered PB, and the *trans*- chamber is filled with pure PB solution. Figure 3.6.3 depicts a simultaneous ionic and tunneling current recording under a 50 mV bias across two chambers, where a negative 50 mV is applied in the *cis*- chamber, and 0 V is applied in the *trans*- chamber. In this test, the concentration of the lambda DNA solution is 0.8 nM, and the ionic currents show characteristic spikes corresponding to the DNA translocation from the *cis*- to *trans*- chamber. The polarity of the ionic spikes is negative, which indicates an increase in the ionic current magnitude and is consistent with the

DNA translocation result using low concentration electrolyte [142]. For ionic events, corresponding current spikes with consistent polarity are observed from the tunneling current measured between the transverse electrodes.

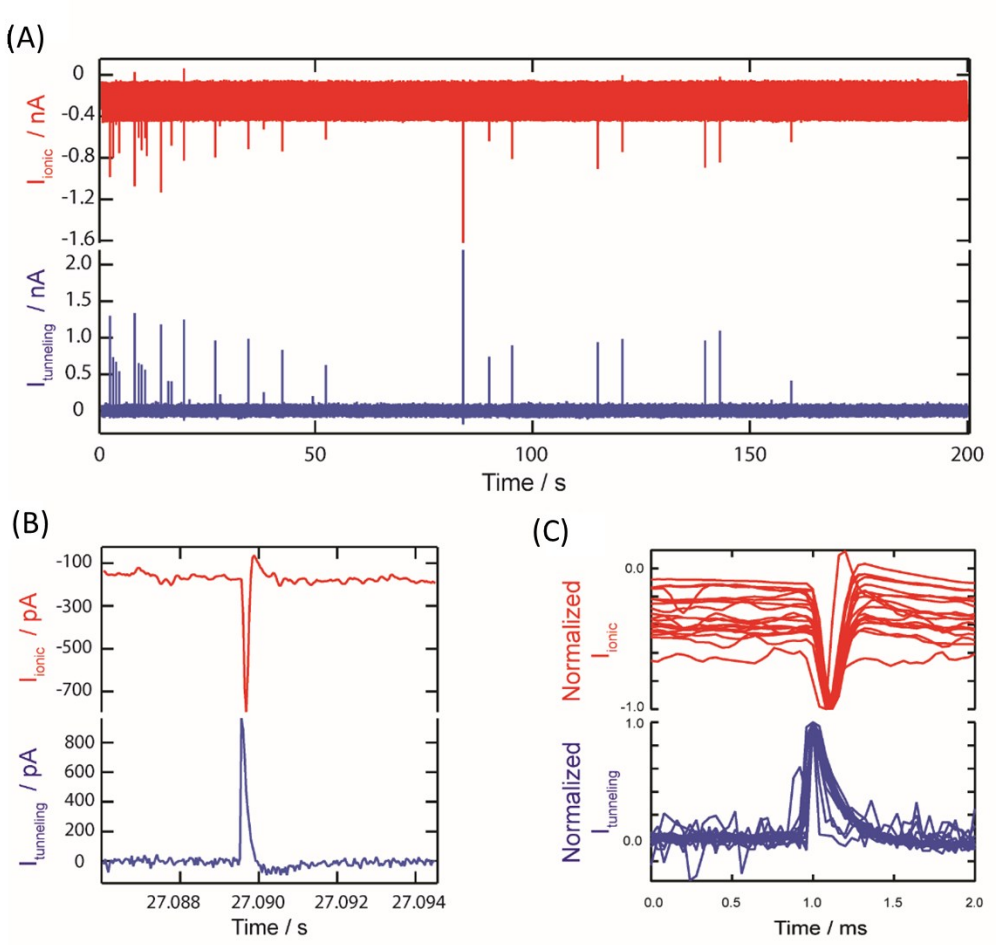

Figure 3.6.3. The simultaneous recording of the ionic and tunneling currents during the DNA translocation. The red line denotes the ionic current and the blue line denotes the "tunneling" current between transverse electrodes. (A) Correlated current spikes on the ionic and tunneling current with consistent polarities during DNA translocations. The lambda DNA solution concentration is 0.8 nM. The *cis*- chamber is -50 mV and the *trans*-chamber is grounded. The bias between the transverse electrodes is 30 mV at 5 Hz. (B) A typical translocation event. (C) An overlapped curve of all normalized translocation events. The ionic and tunneling currents are normalized by their magnitude and all traces are aligned by the peak time of the tunneling spikes.

The simultaneous recording shows three interesting facts. First, the polarity of the tunneling current has a relation with that of the ionic current. Consider a DNA translocation from the *cis*- to the *trans*- chamber, the ionic current spike is negative, and the corresponding tunneling current spike is positive. This opposite relation is also followed if DNA molecules are translocating from the *trans*- to the *cis*- chamber. Second, the shape and timing of the ionic and tunneling currents are not the same. The ionic spikes demonstrate a slight biphasic tail, while the tunneling has a wider peak width and a long tail. Comparing the time of these current events, there is a time offset between the ionic current spikes and their corresponding tunneling spikes. Third, the magnitude of the tunneling spike is high and not dependent on the bias used between the transverse electrodes. A series test result with a 0-30 mV DC and a 0-30 mV AC bias at 5 Hz demonstrate no change in the high spike amplitude. This may indicated that the tunneling signal detected between the transverse electrodes may be caused by the transient movement of the surface charge between the transverse electrodes instead of a tunneling process across the molecule. The high "tunneling" signal hence forms when the DNA molecule comes to contact with one of the transverse electrodes and then moves across the electric double layer to the opposite electrode during DNA translocation. The high spike is related to the fast transition time and the net charge transferred. For convenience, we will use the "tunneling" current to refer to the current monitored between the transverse electrodes.

During the DNA translocation, the EF will affect the molecule movement via electrophoresis and electroosmosis. Based on this, we investigated DNA translocation

with different driving biases across two chambers. Figure 3.6.4 illustrates that as the driving voltage increases, the number of translocation events detected decreases. This might be a consequence of the competition between electrophoretic force, electroosmotic force and entropic forces. As is evident based on the bias applied, the electrophoretic force drive the molecule from the *cis*- to the *trans*- chamber, while the electroosmotic force will push it from the high potential to the low potential. Additional information and control experiments are needed for a better understanding of this phenomenon.

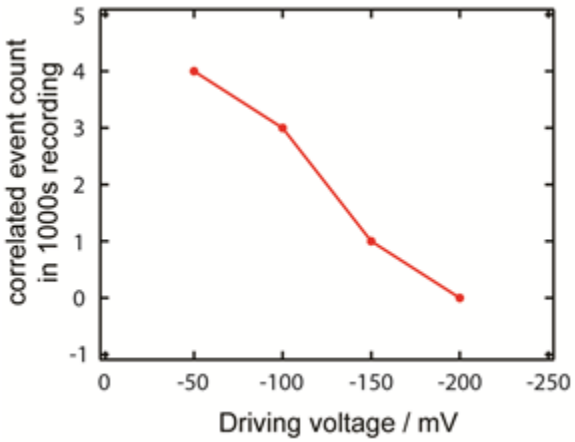

Figure 3.6.4. The number of simultaneous events recorded during DNA translocation with a varying driving bias and a fixed tunneling junction bias. The number of events detected during a 1000-s recording decreases when the driving bias increases from -50-mV to -200-mV. The tunneling junction bias is a 10-mV 5-Hz AC signal with a 10-mV DC offset.

On the other hand, the -200 mV driving bias seems to bring DNA molecules into the microfluidic guidance structure at the *cis*- side and prevent them from translocating to the *trans*- side. A 0 V translocation test is demonstrated after applying a -200 mV driving bias for about 50 mV, as shown in Figure 3.6.5. After 50 min -200 mV driving bias, the driving bias is switched to 0 V, and the current monitoring signal immediately exhibit

long bursts of events with both polarities, indicating DNA translocations from *cis*- to *trans*- and from *trans*- to *cis*-.chambers The density of this translocation is 10 times higher than that observed for the same concentration of DNA solution. Therefore, we believe that the high driving bias accumulates the DNA molecules in the microfluidic structure on the *cis*- side. Once the high driving bias is removed, a high concentration of DNA molecule can pass through the nanopore according to the concentration gradient on different sides of the nanopore. Meanwhile, the reduced electroosmotic force due to the small potential difference between salt bridge reference electrodes may drive the DNA molecule from the *trans*- to the *cis*- chamber. A translocation in both directions is thus recorded with an increasing event density. This may be a possible method to enrich the density of DNA molecules for a low copy number detection.

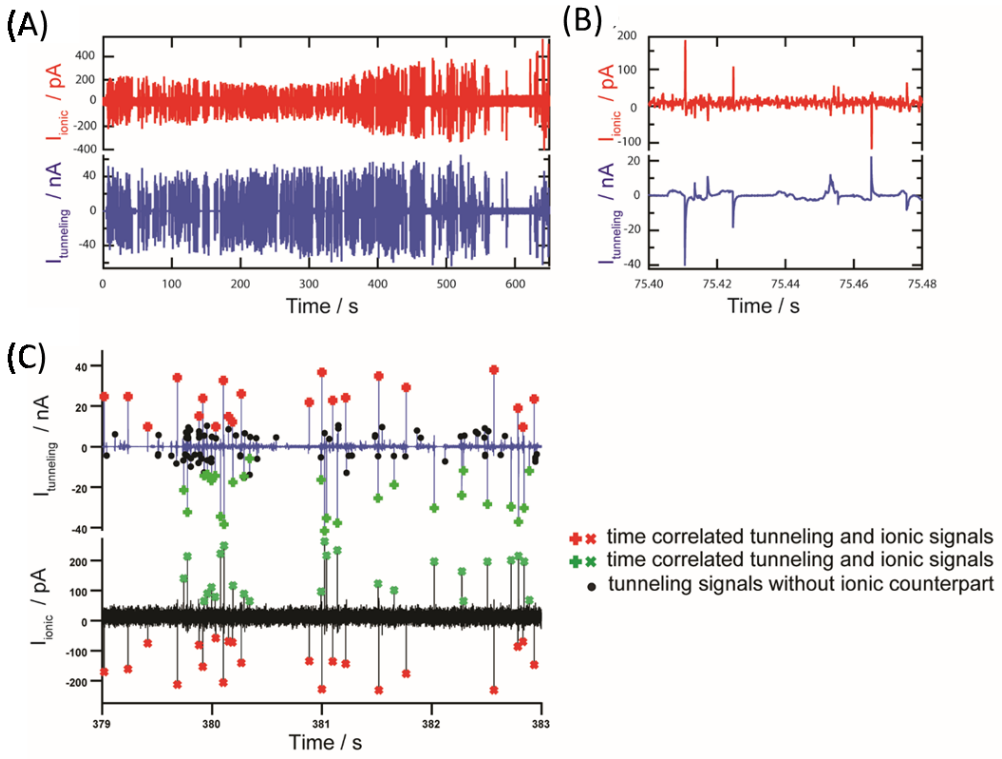

Figure 3.6.5. DNA translocation recording after DNA molecule accumulation in the guidance area after applying a -200-mV driving bias for about 50 min. The initial concentration of DNA solution is 8 nM. (A) DNA translocation with a 5-Hz, 10-mV gap bias and 0-V driving voltage. The potential differences between agar gel salt bridge reference electrodes provide a driving force for DNA translocation. (B) A detail look of several events occurring during the recording. In most cases, the ionic current peak has an opposite polarity to the tunneling peak. Occasionally, the tunneling current shows slower fluctuation with wider and irregular peaks ahead of or during ionic current peak. (C) A detailed view of the result of the peak-finding program labeling the tunneling peaks with and without correlated ionic peaks respectively. The correlated events from *cis*- to *trans*- are denoted by red crosses, while the correlated events from *trans*- to *cis*- are indicated by green crosses, and uncorrelated events are labeled with black dots.

3.7. Statistics of Correlated and Uncorrelated DNA Translocation Events

Taking the advantage of the bi-directional recording in Figure 3.6.5A, a statistic study of the translocation behavior in our device can be conducted. In this study, we define the events occuring in the ionic current and tunneling current within twice of the peak width as “correlated” events. In Figure 3.6.5C, the red crosses denote the downward

ionic spikes and correlated upward tunneling spikes, while the green crosses denote the upward ionic spikes and correlated downward tunneling spikes. Comparing these correlated events, more than 93% of ionic events have correlated tunneling events, and only less than 35% of tunneling events are correlated with ionic events.

By studying the data based on the peak time position, peak height and peak width (full width at half maximum, [FWHM]), some interesting facts emerge about these events, as shown Figure 3.7.1. First, the total numbers of the correlated translocations from *cis*- to *trans*- and from *trans*- to *cis*- are similar, and their distributions in peak height and peak width are also symmetrical due to the polarity. This is consistent with our devices, where the concentration gradient between two sides of the nanopore and a weak electroosmotic force are believed to be the driving forces for translocations in different directions. Second, the tunneling peaks occur before their correlated ionic peaks in both directions. The leading time of tunneling peaks are 35 μs, 50 μs, and 65 μs compared to the ionic peaks, suggesting that this distribution is not a result of an offset in the filter or a time delay in the electronic instruments. The interactions between the geometry of the deposited tunneling junction and the translocating molecule may be related to this peak time delay. Third, the peak width of the tunneling peaks in both directions is approximately 0.2 ms, which is wider than that of their correlated ionic peaks. For the ionic peaks, the translocation time from the *cis*- to *trans*- chamber is shorter than that from the *trans*- to *cis*- chamber. The enriched molecule concentration at the *cis*- side may result in a faster translocation compared to the weak electroosmotic force. Fourth, comparing the correlated and uncorrelated events, more than 93% of ionic events have a correlated tunneling speak, suggesting that our preparation of nanopore and tunneling

junction is successful in dimension control and alignment. Most molecules passing through the nanopore will interact with the deposited tunneling junction and generate a signal. However, only one third of the tunneling peaks have corresponding ionic peaks. Interestingly, there are some differences between these correlated and uncorrelated tunneling peaks. The peak width distribution of correlated tunneling events demonstrates a narrow peak between 0.2 ms and 0.4 ms, while the uncorrelated tunneling events have a broad distribution between 0.2 ms and 1.4 ms. Moreover, the peak height of the correlated events has a broad distribution between 10 nA and 40 nA, while that of the uncorrelated events has a narrow distribution between 5 nA and 20 nA. This may be caused by the random contact between the DNA molecule and the surface of the transverse electrode instead of DNA translocation. The wider peak width may also suggest stronger interactions and the smaller peak height may be the result of a longer section bridging the electrodes.

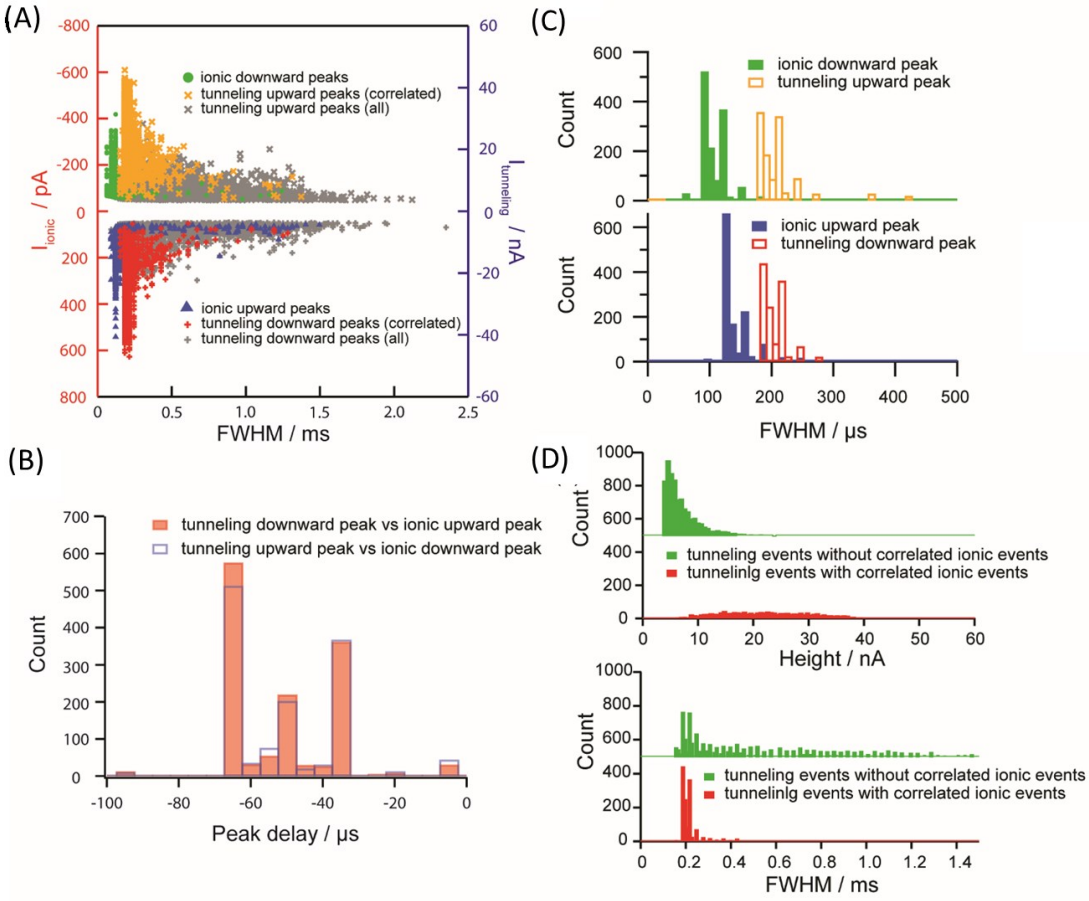

Figure 3.7.1. Statistics of the DNA translocation events with enriched concentration. The gap bias is a 10-mV, 5-Hz AC signal, and the driving voltage is a 0-V DC. (A) The histogram of peak height and the full width at half maximum (FWHM) of translocation events in tunneling and ionic currents. (B) The histogram of FWHM of correlated translocation events. Top: FWHMs of tunneling upward peak and correlated ionic downward peak. Bottom: FWHMs of tunneling downward peak and correlated ionic upward peak. (C) The peak delay between correlated peaks. A negative peak delay value indicates that the tunneling peak occurs before the ionic peak. (D) The histogram comparison between tunneling events with correlated ionic events and tunneling events without correlated ionic events. Top: the histogram of peak height. Tunneling events with correlated ionic events show a broader distribution of peaks compared to those events without correlated ionic events. Bottom: the histogram of FWHM. Tunneling events with correlated ionic events exhibit similar FWHM near 0.2ms, while those without correlated ionic events have a broad distribution of FWHMs.

3.8. Discussion and Conclusion

As a promising candidate for the next generation technique for molecule sensing, solid-state nanopore device demonstrates a great potential for single molecule level sensing. Many works have been done to apply active control methods to slow down the translocation speed. Meanwhile, tunneling current sensing as a new paradigm for molecule sensing is now becoming increasingly interesting and feasible for applications. Current drawbacks of solid-state nanopore or related structure pertain to scalable fabrication and pore size control. To solve these issues, we developed a new fabrication strategy for solid-state nanopores and integrated a tunneling junction with a nanopore via electrochemical deposition.

In this project, we initially designed and fabricated a planar nanopore device with a self-aligned tunneling junction. The fabrication protocol consisted of standard lithography techniques and feedback-controlled electrochemical deposition. The journey begins with an electrochemical deposition on bare electrode tips, with gradual testing in confined structures with different material combinations, and we finally determined the current structure and materials. Then, for the integration of our device chip with a microfluidic system, a series of tests were performed concerning fabrication and characterizations. The final device has proven to be reproducible and reliable in terms of fabrication. With a robust fabrication method, we have demonstrated a control of nanopore and tunneling junction gap size. Furthermore, DNA translocation tests were conducted with the fabricated nanopore, and we observed the correlated translocation events recorded in both ionic and tunneling currents for the first time. Although our result suggests that the tunneling signal collected via the tunneling junction is still dominate by

the transient current due to static charge movement instead of the actual tunneling process, this device proves to be a new test platform for related experiments due to its flexibility and reproducibility.

3.9. Future Works

The first few trials of current planar nanopore devices involving DNA translocation have only recently been completed, therefore the future experiments related to this platform consist of the following three aspects: The first aspect is to distinguish the real tunneling current signal from the transient current, the second aspect is to achieve active translocation control via highly localized EF through our transverse electrodes, and the third aspect is to make our device a multipurpose platform for related or similar experiments.

First, as we previously mentioned, the "tunneling" current recorded is dominated by the transient current based on static charge movement, not the tunneling process. Thus, distinguishing the real tunneling current signal from the transient current is an important goal before utilizing our device platform. Although this is an open question to us now, but several approaches are considered to solve this transient current issue, including tuning the Debye length in solution and surface charges in nanopores, redesigning the guidance structure, and developing new automatic deposition control protocol or system for better reliability and fine-tuning of the final nanopore and tunneling junctions instead of sending corresponding pulses manually. Moreover, recognition molecule surface modification on the deposited tunneling junction may improve the tunneling current detection and gives a better understanding of single-base detection. We current planning to modify the tunneling junction with recognition

molecule, 4(5)-(2-mercaptoethyl)-1H-imidazole-2-carboxamide (ICA) and detect the tunneling signals of different amino acids and short peptide sequences via the formation of specific hydrogen bonds. This experiment would afford us a better understanding of the single-level sensing of DNA and proteins.

Second, the tunneling junction and the guidance structure are designed to control DNA translocation behaviors during the experiments. As we have shown in previous sections, the guidance structure enhances the DNA concentration and stretches the molecules before entering the center nanopore. In the follow-up experiments, we would like to have a series of tests to obtain quantitative results of the enrichment and shaping of DNA molecules by electrostatic and electroosmotic force inside the guidance structure, and the active control of DNA translocation with transverse EFs via the embedded electrodes. Therefore, quantification of characteristics of the ionic and tunneling events in terms of peak width and height under different EF conditions and demonstration of stepwise DNA translocations by proper transverse EF and surface modification are the next goals.

Third, we would like to develop our chip design to be a multipurpose platform. For example, it can also be integrated with biological nanopores/readers inside the tunneling junction, forming a hybrid sequencing device instead of using the deposited nanopore directly. In addition, by changing the metal and deposition method of the tunneling junction, it is possible to make our devices to be spin-dependent. Instead of the symmetric deposition of gold on the transverse electrodes, deposition of Ni on the tunneling junction may enable us to inject spin-polarized current through bio-molecules

and detect its chirality. It would be interesting to develop novel spintronic platforms based on our designs.

In summary, this novel planar nanopore device with self-aligned tunneling junction is just making its first step. The follow up experiment about this device would focus on the improvement of tunneling current measurement accuracy, the active control of the tunneling junction, and the additional integration of new functions.

CHAPTER 4. CONCLUSION

This dissertation focuses on the modulation and sensation of cells and biomolecules using spatiotemporally encoded EF. At the cellular level, I worked on AC EF modulation of the ERK signaling pathway in epithelial cells, where my main contribution was the design and fabrication of a new microelectrode array chip. At the molecular level, I developed a new planar nanopore chip integrated with transverse tunneling junctions for DNA detection and sequencing, and demonstrated for the first time real-time simultaneous detection of DNA molecules from both the ionic current and the tunneling current.

In Chapter 2, I introduce our microelectrode platform that enable the AC EF modulation of live cells at a finer spatial and temporal resolution. Conventional experiment setups for EF modulations and stimulations focus on DC voltage and suffers from both possible EF-induced environmental changes and the averaging effect of the long experiment and analysis time. To overcome these issues, a paradigm shift in the EF signal delivery system is necessary to provide an improved temporal and spatial resolution. After researching and reviewing the theoretical modeling and previous experiment results in a broader frequency range, we decided to fabricate a microelectrode array chip that would apply EF stimulations in localized areas at the hundreds-of-microns level and select an intermediate range frequency AC signal to interact with the membrane protein directly, making a possible experimental proof of those theoretical models about the membrane potential. Compared to a conventional experiment setup, our device eliminates Faradaic processes and avoids possible biochemical changes such as pH, ROS and Ca2+ changes induced by DC or asymmetric EF signals. Combined with the

genetically modified MCF10A epithelial cells, our experiment setup enables a real-time quantitative analysis of the ERK signaling pathway activation. As a result, our new device chip could modulate the ERK activation precisely in both a spatial and a temporal manner. To better understand the underlying mechanism of the interaction between signaling pathways and AC EF stimulation, a series inhibitor tests were performed and suggest that AC EF stimulation can directly trigger ERK phosphorylation without EGF binding possibly due to conformational changes of membrane proteins under EF stimulation. This project provides a new platform for accurate EF stimulation delivery and new insights for unveiling the interaction mechanism between cells and EF stimulation.

In Chapter 3, I introduced the new planar nanopore chip integrated with self-aligned transverse tunneling junctions. Nanopore devices are promising techniques for the next generation DNA sequencing and molecule detection. Although biological nanopores have proven their capability for DNA sequencing and are already commercialized, solid-state nanopore devices are possible platforms for the single-molecule-level detection due to their capability of pore size control and integration with extra translocation control and detection structures. However, the solid-state nanopore devices currently have poor scalability and pore size control. To solve these issues, we developed a new fabrication strategy consisting of photolithography techniques and feedback-controlled electrochemical deposition. Our experiments highlight the feasibility and reproducibility of this fabrication strategy. We have also demonstrated DNA translocation with our new device, showing the correlated translocation events recorded in both ionic and tunneling currents for the first time. Although our results suggest that

this tunneling signal, collected via the deposited tunneling junction, is still dominated by the transient current due to static charge movement instead of the actual tunneling process, our device could be used as a new platform for DNA translocation and other related experiments. Further studies are needed to understand this preliminary result and the entire experiment setup could be improved by integrating an automatic feedback control circuit, aiming for a better nanopore and tunneling junction size control.

In summary, my research focuses on the EF and biomolecule interactions at different levels. With spatiotemporally encoded EF enabled by novel micro/nanofabrication strategies, the activities of biomolecules and cells could be precisely modulated and detected. Our results can provide a new biophysical approach for interacting with living systems.

REFERENCES

1. McCaig, C.D., et al., *Controlling cell behavior electrically: Current views and future potential.* Physiological Reviews, 2005. **85**(3): p. 943-978.

2. Geddes, L.A., *The Beginnings of Electromedicine.* Ieee Engineering in Medicine and Biology Magazine, 1984. **3**(4): p. 8-23.

3. Funk, R.H.W., T. Monsees, and N. Ozkucur, *Electromagnetic effects - From cell biology to medicine.* Progress in Histochemistry and Cytochemistry, 2009. **43**(4): p. 177-264.

4. Bean, B.P., *The action potential in mammalian central neurons.* Nature Reviews Neuroscience, 2007. **8**(6): p. 451-465.

5. Reid, B. and M. Zhao, *The Electrical Response to Injury: Molecular Mechanisms and Wound Healing.* Adv Wound Care (New Rochelle), 2014. **3**(2): p. 184-201.

6. Nuccitelli, R., *Endogenous electric fields in embryos during development, regeneration and wound healing.* Radiat Prot Dosimetry, 2003. **106**(4): p. 375-83.

7. Jenkins, L.S., B.S. Duerstock, and R.B. Borgens, *Reduction of the current of injury leaving the amputation inhibits limb regeneration in the red spotted newt.* Dev Biol, 1996. **178**(2): p. 251-62.

8. Du, J., et al., *Optimal electrical stimulation boosts stem cell therapy in nerve regeneration.* Biomaterials, 2018. **181**: p. 347-359.

9. Borgens, R.B., E. Roederer, and M.J. Cohen, *Enhanced Spinal-Cord Regeneration in Lamprey by Applied Electric-Fields.* Science, 1981. **213**(4508): p. 611-617.

10. Zhao, S., A.S. Mehta, and M. Zhao, *Biomedical applications of electrical stimulation.* Cell Mol Life Sci, 2020.

11. Thakral, G., et al., *Electrical stimulation to accelerate wound healing.* Diabet Foot Ankle, 2013. **4**.

12. Morris, C., *Bio-electrical stimulation therapy using POSiFECT®RD.* Wounds UK, 2006. **2**(4): p. 112-116.

13. Banerjee, J., et al., *Improvement of human keratinocyte migration by a redox active bioelectric dressing.* PLoS One, 2014. **9**(3): p. e89239.

14. Cohen, A.E., et al., *Evaluation of dexamethasone phosphate delivered by ocular iontophoresis for treating noninfectious anterior uveitis.* Ophthalmology, 2012. **119**(1): p. 66-73.

15. Fan, D.L., et al., *Electric tweezers.* Nano Today, 2011. **6**(4): p. 339-354.

16. Shen, Y.J., et al., *Optical vortices 30 years on: OAM manipulation from topological charge to multiple singularities.* Light-Science & Applications, 2019. **8**.

17. Grier, D.G., *A revolution in optical manipulation.* Nature, 2003. **424**(6950): p. 810-816.

18. Ashkin, A., *History of optical trapping and manipulation of small-neutral particle, atoms, and molecules.* Ieee Journal of Selected Topics in Quantum Electronics, 2000. **6**(6): p. 841-856.

19. Madariaga-Marcos, J., et al., *Lateral Magnetic Tweezers to Study DNA: Protein Interactions.* Biophysical Journal, 2018. **114**(3): p. 91a-91a.

20. Meng, L., et al., *Acoustic tweezers.* Journal of Physics D-Applied Physics, 2019. **52**(27).

21. Wang, H., L.G. Chen, and L.N. Sun, *Digital microfluidics: A promising technique for biochemical applications.* Frontiers of Mechanical Engineering, 2017. **12**(4): p. 510-525.

22. Sanger, F., S. Nicklen, and A.R. Coulson, *DNA Sequencing with Chain-Terminating Inhibitors.* Proceedings of the National Academy of Sciences of the United States of America, 1977. **74**(12): p. 5463-5467.

23. Ronaghi, M., M. Uhlen, and P. Nyren, *A sequencing method based on real-time pyrophosphate.* Science, 1998. **281**(5375): p. 363-+.

24. Strick, T.R., et al., *The elasticity of a single supercoiled DNA molecule.* Science, 1996. **271**(5257): p. 1835-1837.

25. Magde, D., W.W. Webb, and E. Elson, *Thermodynamic Fluctuations in a Reacting System - Measurement by Fluorescence Correlation Spectroscopy.* Physical Review Letters, 1972. **29**(11): p. 705-&.

26. Ha, T., et al., *Probing the interaction between two single molecules: Fluorescence resonance energy transfer between a single donor and a single acceptor.*

Proceedings of the National Academy of Sciences of the United States of America, 1996. **93**(13): p. 6264-6268.

27. Binnig, G., C.F. Quate, and C. Gerber, *Atomic Force Microscope.* Physical Review Letters, 1986. **56**(9): p. 930-933.

28. Don, M., *The Coulter Principle: Foundation of an Industry.* JALA: Journal of the Association for Laboratory Automation, 2003. **8**(6): p. 72-81.

29. Shi, W.Q., A.K. Friedman, and L.A. Baker, *Nanopore Sensing.* Analytical Chemistry, 2017. **89**(1): p. 157-188.

30. Albrecht, T., *Progress in single-biomolecule analysis with solid-state nanopores.* Current Opinion in Electrochemistry, 2017. **4**(1): p. 159-165.

31. Cournia, Z., et al., *Membrane Protein Structure, Function, and Dynamics: a Perspective from Experiments and Theory.* Journal of Membrane Biology, 2015. **248**(4): p. 611-640.

32. Zhao, M., *Electrical fields in wound healing—An overriding signal that directs cell migration.* Seminars in Cell & Developmental Biology, 2009. **20**(6): p. 674-682.

33. Liu, Q. and B. Song, *Electric field regulated signaling pathways.* The International Journal of Biochemistry & Cell Biology, 2014. **55**: p. 264-268.

34. Nuccitelli, R., *Application of Pulsed Electric Fields to Cancer Therapy.* Bioelectricity, 2019. **1**(1): p. 30-34.

35. Payne, S.L., M. Levin, and M.J. Oudin, *Bioelectric Control of Metastasis in Solid Tumors.* Bioelectricity, 2019. **1**(3): p. 114-130.

36. Pless, M. and U. Weinberg, *Tumor treating fields: concept, evidence and future.* Expert Opinion on Investigational Drugs, 2011. **20**(8): p. 1099-1106.

37. Davies, A.M., U. Weinberg, and Y. Palti, *Tumor treating fields: a new frontier in cancer therapy.* Annals of the New York Academy of Sciences, 2013. **1291**(1): p. 86-95.

38. Jaffe, L.F. and J.W. Vanable, *Electric fields and wound healing.* Clinics in Dermatology, 1984. **2**(3): p. 34-44.

39. Weaver, J.C. and Y.A. Chizmadzhev, *Theory of electroporation: A review.* Bioelectrochemistry and Bioenergetics, 1996. **41**(2): p. 135-160.

40. Kirson, E.D., et al., *Disruption of cancer cell replication by alternating electric fields.* Cancer Research, 2004. **64**(9): p. 3288-3295.

41. Stork, P.J., *ERK signaling: duration, duration, duration.* Cell Cycle, 2002. **1**(5): p. 315-7.

42. Murphy, L.O., et al., *Molecular interpretation of ERK signal duration by immediate early gene products.* Nat Cell Biol, 2002. **4**(8): p. 556-64.

43. Kress, G.J. and S. Mennerick, *Action potential initiation and propagation: upstream influences on neurotransmission.* Neuroscience, 2009. **158**(1): p. 211-22.

44. Hodgkin, A.L. and A.F. Huxley, *A Quantitative Description of Membrane Current and Its Application to Conduction and Excitation in Nerve.* Journal of Physiology-London, 1952. **117**(4): p. 500-544.

45. Zhao, M., *Electrical fields in wound healing-An overriding signal that directs cell migration.* Seminars in Cell & Developmental Biology, 2009. **20**(6): p. 674-682.

46. Song, B., et al., *Nerve regeneration and wound healing are stimulated and directed by an endogenous electrical field in vivo.* J Cell Sci, 2004. **117**(Pt 20): p. 4681-90.

47. Song, B., et al., *Electrical cues regulate the orientation and frequency of cell division and the rate of wound healing in vivo.* Proceedings of the National Academy of Sciences of the United States of America, 2002. **99**(21): p. 13577-13582.

48. Borgens, R.B., J.W. Vanable, Jr., and L.F. Jaffe, *Bioelectricity and regeneration: large currents leave the stumps of regenerating newt limbs.* Proc Natl Acad Sci U S A, 1977. **74**(10): p. 4528-32.

49. Borgens, R.B., L.F. Jaffe, and M.J. Cohen, *Large and Persistent Electrical Currents Enter the Transected Lamprey Spinal-Cord.* Proceedings of the National Academy of Sciences of the United States of America-Biological Sciences, 1980. **77**(2): p. 1209-1213.

50. Creed, M.C., et al., *Contribution of decreased serotonin release to the antidyskinetic effects of deep brain stimulation in a rodent model of tardive dyskinesia: comparison of the subthalamic and entopeduncular nuclei.* J Neurosci, 2012. **32**(28): p. 9574-81.

51. Jahanshahi, A., et al., *In vitro and in vivo neuronal electrotaxis: a potential mechanism for restoration?* Mol Neurobiol, 2014. **49**(2): p. 1005-16.

52. Zhao, M., J. Penninger, and R.R. Isseroff, *Electrical Activation of Wound-Healing Pathways.* Adv Skin Wound Care, 2010. **1**: p. 567-573.

53. Borgens, R.B., E. Roederer, and M.J. Cohen, *Enhanced spinal cord regeneration in lamprey by applied electric fields.* Science, 1981. **213**(4508): p. 611-7.

54. Pollack, G.H. and F.B. Reitz, *Phase transitions and molecular motion in the cell.* Cell Mol Biol (Noisy-le-grand), 2001. **47**(5): p. 885-900.

55. Huang, L., et al., *The involvement of Ca2+ and integrins in directional responses of zebrafish keratocytes to electric fields.* J Cell Physiol, 2009. **219**(1): p. 162-72.

56. Rico-Varela, J., D. Ho, and L.Q. Wan, *In Vitro Microscale Models for Embryogenesis.* Advanced Biosystems, 2018. **2**(6).

57. Schwartz, L., J.D. Moreira, and M. Jolicoeur, *Physical forces modulate cell differentiation and proliferation processes.* Journal of Cellular and Molecular Medicine, 2018. **22**(2): p. 738-745.

58. Gao, R.C., et al., *Different Roles of Membrane Potentials in Electrotaxis and Chemotaxis of Dictyostelium Cells.* Eukaryotic Cell, 2011. **10**(9): p. 1251-1256.

59. Nakajima, K., et al., *KCNJ15/Kir4.2 couples with polyamines to sense weak extracellular electric fields in galvanotaxis.* Nature Communications, 2015. **6**.

60. Humphrey, J.D., E.R. Dufresne, and M.A. Schwartz, *Mechanotransduction and extracellular matrix homeostasis.* Nat Rev Mol Cell Biol, 2014. **15**(12): p. 802-12.

61. Finkelstein, E.I., et al., *Electric field-induced polarization of charged cell surface proteins does not determine the direction of galvanotaxis.* Cell Motility and the Cytoskeleton, 2007. **64**(11): p. 833-846.

62. Lin, B.J., et al., *Lipid rafts sense and direct electric field-induced migration.* Proceedings of the National Academy of Sciences of the United States of America, 2017. **114**(32): p. 8568-8573.

63. Meng, X.T., et al., *PI3K mediated electrotaxis of embryonic and adult neural progenitor cells in the presence of growth factors.* Experimental Neurology, 2011. **227**(1): p. 210-217.

64. Sato, M.J., et al., *Switching direction in electric-signal-induced cell migration by cyclic guanosine monophosphate and phosphatidylinositol signaling.* Proceedings

of the National Academy of Sciences of the United States of America, 2009. **106**(16): p. 6667-6672.

65. Zhao, M., et al., *Electrical signals control wound healing through phosphatidylinositol-3-OH kinase-gamma and PTEN.* Nature, 2006. **442**(7101): p. 457-460.

66. Li, F., et al., *Superoxide plays critical roles in electrotaxis of fibrosarcoma cells via activation of ERK and reorganization of the cytoskeleton.* Free Radic Biol Med, 2012. **52**(9): p. 1888-96.

67. Li, F., et al., *Superoxide mediates direct current electric field-induced directional migration of glioma cells through the activation of AKT and ERK.* PLoS One, 2013. **8**(4): p. e61195.

68. Sheikh, A.Q., et al., *Regulation of endothelial MAPK/ERK signalling and capillary morphogenesis by low-amplitude electric field.* Journal of the Royal Society Interface, 2013. **10**(78).

69. Astumian, R.D., et al., *Effects of Oscillations and Energy-Driven Fluctuations on the Dynamics of Enzyme Catalysis and Free-Energy Transduction.* Physical Review A, 1989. **39**(12): p. 6416-6435.

70. Astumian, R.D. and B. Robertson, *Nonlinear Effect of an Oscillating Electric-Field on Membrane-Proteins.* Journal of Chemical Physics, 1989. **91**(8): p. 4891-4901.

71. Fricke, H., *The Electric Permittivity of a Dilute Suspension of Membrane-Covered Ellipsoids.* Journal of Applied Physics, 1953. **24**(5): p. 644-646.

72. Schwan, H.P., *Electrical properties of tissue and cell suspensions.* Adv Biol Med Phys, 1957. **5**: p. 147-209.

73. Grosse, C. and H.P. Schwan, *Cellular Membrane-Potentials Induced by Alternating-Fields.* Biophysical Journal, 1992. **63**(6): p. 1632-1642.

74. Weaver, J.C. and R.D. Astumian, *The Response of Living Cells to Very Weak Electric-Fields - the Thermal Noise Limit.* Science, 1990. **247**(4941): p. 459-462.

75. Kotnik, T. and D. Miklavcic, *Theoretical evaluation of the distributed power dissipation in biological cells exposed to electric fields.* Bioelectromagnetics, 2000. **21**(5): p. 385-394.

76. Chen, W., *Synchronization of ion exchangers by an oscillating electric field: Theory.* Journal of Physical Chemistry B, 2008. **112**(32): p. 10064-10070.

77. Zhao, M., et al., *Electric field-directed cell motility involves up-regulated expression and asymmetric redistribution of the epidermal growth factor receptors and is enhanced by fibronectin and laminin.* Mol Biol Cell, 1999. **10**(4): p. 1259-76.

78. Harvey, C.D., et al., *A genetically encoded fluorescent sensor of ERK activity.* Proceedings of the National Academy of Sciences of the United States of America, 2008. **105**(49): p. 19264-19269.

79. Sparta, B., et al., *Receptor Level Mechanisms Are Required for Epidermal Growth Factor (EGF)-stimulated Extracellular Signal-regulated Kinase (ERK) Activity Pulses.* Journal of Biological Chemistry, 2015. **290**(41): p. 24784-24792.

80. Regot, S., et al., *High-Sensitivity Measurements of Multiple Kinase Activities in Live Single Cells.* Cell, 2014. **157**(7): p. 1724-1734.

81. de la Cova, C., et al., *A Real-Time Biosensor for ERK Activity Reveals Signaling Dynamics during C. elegans Cell Fate Specification.* Developmental Cell, 2017. **42**(5): p. 542-+.

82. Yao, J., B.Y. Liu, and F. Qin, *Rapid Temperature Jump by Infrared Diode Laser Irradiation for Patch-Clamp Studies.* Biophysical Journal, 2009. **96**(9): p. 3611-3619.

83. Wilkins, M.H.F., A.R. Stokes, and H.R. Wilson, *Molecular Structure of Deoxypentose Nucleic Acids.* Nature, 1953. **171**(4356): p. 738-740.

84. Sinden, R.R., *CHAPTER 1 - Introduction to the Structure, Properties, and Reactions of DNA*, in *DNA Structure and Function*, R.R. Sinden, Editor. 1994, Academic Press: San Diego. p. 1-57.

85. Tanaka, H. and T. Kawai, *Partial sequencing of a single DNA molecule with a scanning tunnelling microscope.* Nature Nanotechnology, 2009. **4**(8): p. 518-522.

86. Lagerqvist, J., M. Zwolak, and M. Di Ventra, *Fast DNA sequencing via transverse electronic transport.* Nano Letters, 2006. **6**(4): p. 779-782.

87. Zwolak, M. and M. Di Ventra, *Electronic signature of DNA nucleotides via transverse transport.* Nano Letters, 2005. **5**(3): p. 421-424.

88. Di Ventra, M. and M. Taniguchi, *Decoding DNA, RNA and peptides with quantum tunnelling.* Nature Nanotechnology, 2016. **11**(2): p. 117-126.

89. Deng, T., et al., *Development of solid-state nanopore fabrication technologies.* Science Bulletin, 2015. **60**(3): p. 304-319.

90. Long, Z., et al., *Recent Advances in Solid Nanopore/Channel Analysis.* Analytical Chemistry, 2018. **90**(1): p. 577-588.

91. Stoloff, D.H. and M. Wanunu, *Recent trends in nanopores for biotechnology.* Current Opinion in Biotechnology, 2013. **24**(4): p. 699-704.

92. Lindsay, S., *The promises and challenges of solid-state sequencing.* Nature Nanotechnology, 2016. **11**(2): p. 109-111.

93. Kasianowicz, J.J., et al., *Characterization of individual polynucleotide molecules using a membrane channel.* Proceedings of the National Academy of Sciences of the United States of America, 1996. **93**(24): p. 13770-13773.

94. Haque, F., et al., *Solid-state and biological nanopore for real-time sensing of single chemical and sequencing of DNA.* Nano Today, 2013. **8**(1): p. 56-74.

95. Akeson, M., et al., *Microsecond time-scale discrimination among polycytidylic acid, polyadenylic acid, and polyuridylic acid as homopolymers or as segments within single RNA molecules.* Biophysical Journal, 1999. **77**(6): p. 3227-3233.

96. Manrao, E.A., et al., *Reading DNA at single-nucleotide resolution with a mutant MspA nanopore and phi29 DNA polymerase.* Nature Biotechnology, 2012. **30**(4): p. 349-U174.

97. Cherf, G.M., et al., *Automated forward and reverse ratcheting of DNA in a nanopore at 5-angstrom precision.* Nature Biotechnology, 2012. **30**(4): p. 344-348.

98. Soskine, M., A. Biesemans, and G. Maglia, *Single-Molecule Analyte Recognition with ClyA Nanopores Equipped with Internal Protein Adaptors.* Journal of the American Chemical Society, 2015. **137**(17): p. 5793-5797.

99. Wang, S.Y., et al., *Channel of viral DNA packaging motor for real time kinetic analysis of peptide oxidation states.* Biomaterials, 2017. **126**: p. 10-17.

100. Fahie, M.A., et al., *Tuning the Selectivity and Sensitivity of an OmpG Nanopore Sensor by Adjusting Ligand Tether Length.* Acs Sensors, 2016. **1**(5): p. 614-622.

101. Cao, C., et al., *Driven Translocation of Polynucleotides Through an Aerolysin Nanopore.* Analytical Chemistry, 2016. **88**(10): p. 5046-5049.

102. Jain, M., et al., *Improved data analysis for the MinION nanopore sequencer.* Nature Methods, 2015. **12**(4): p. 351-U115.

103. Mikheyev, A.S. and M.M.Y. Tin, *A first look at the Oxford Nanopore MinION sequencer.* Molecular Ecology Resources, 2014. **14**(6): p. 1097-1102.

104. Jain, M., et al., *The Oxford Nanopore MinION: delivery of nanopore sequencing to the genomics community.* Genome Biology, 2016. **17**.

105. Li, J., et al., *Ion-beam sculpting at nanometre length scales.* Nature, 2001. **412**(6843): p. 166-169.

106. Li, J.L., et al., *DNA molecules and configurations in a solid-state nanopore microscope.* Nature Materials, 2003. **2**(9): p. 611-615.

107. Storm, A.J., et al., *Fabrication of solid-state nanopores with single-nanometre precision.* Nature Materials, 2003. **2**(8): p. 537-540.

108. Storm, A.J., et al., *Fast DNA translocation through a solid-state nanopore.* Nano Letters, 2005. **5**(7): p. 1193-1197.

109. Heng, J.B., et al., *The electromechanics of DNA in a synthetic nanopore.* Biophysical Journal, 2006. **90**(3): p. 1098-1106.

110. Wanunu, M., et al., *DNA Translocation Governed by Interactions with Solid-State Nanopores.* Biophysical Journal, 2008. **95**(10): p. 4716-4725.

111. Li, J. and D.S. Talaga, *The distribution of DNA translocation times in solid-state nanopores.* J Phys Condens Matter, 2010. **22**(45): p. 454129.

112. Fologea, D., et al., *Slowing DNA translocation in a solid-state nanopore.* Nano Letters, 2005. **5**(9): p. 1734-1737.

113. Kowalczyk, S.W., et al., *Slowing down DNA Translocation through a Nanopore in Lithium Chloride.* Nano Letters, 2012. **12**(2): p. 1038-1044.

114. Keyser, U.F., *Optical tweezers for mechanical control over DNA in a nanopore.* Methods Mol Biol, 2012. **870**: p. 115-34.

115. Peng, H.B. and X.S.S. Ling, *Reverse DNA translocation through a solid-state nanopore by magnetic tweezers.* Nanotechnology, 2009. **20**(18).

116. Venkatesan, B.M., et al., *DNA Sensing Using Nanocrystalline Surface-Enhanced Al2O3 Nanopore Sensors.* Advanced Functional Materials, 2010. **20**(8): p. 1266-1275.

117. Merchant, C.A., et al., *DNA Translocation through Graphene Nanopores.* Nano Letters, 2010. **10**(8): p. 2915-2921.

118. Liu, S., et al., *Boron Nitride Nanopores: Highly Sensitive DNA Single-Molecule Detectors.* Advanced Materials, 2013. **25**(33): p. 4549-4554.

119. Wei, R., et al., *DNA origami gatekeepers for solid-state nanopores.* Angew Chem Int Ed Engl, 2012. **51**(20): p. 4864-7.

120. Larkin, J., et al., *Slow DNA Transport through Nanopores in Hafnium Oxide Membranes.* Acs Nano, 2013. **7**(11): p. 10121-10128.

121. Polonsky, S., S. Rossnagel, and G. Stolovitzky, *Nanopore in metal-dielectric sandwich for DNA position control.* Applied Physics Letters, 2007. **91**(15).

122. Harrer, S., et al., *Electrochemical protection of thin film electrodes in solid state nanopores.* Nanotechnology, 2011. **22**(27).

123. Luan, B.Q., et al., *Base-By-Base Ratcheting of Single Stranded DNA through a Solid-State Nanopore.* Physical Review Letters, 2010. **104**(23).

124. Harrer, S., et al., *Electrochemical Characterization of Thin Film Electrodes Toward Developing a DNA Transistor.* Langmuir, 2010. **26**(24): p. 19191-19198.

125. Healy, K., et al., *Fabrication and characterization of nanopores with insulated transverse nanoelectrodes for DNA sensing in salt solution.* Electrophoresis, 2012. **33**(23): p. 3488-3496.

126. Fischbein, M.D. and M. Drndic, *Sub-10 nm device fabrication in a transmission electron microscope.* Nano Letters, 2007. **7**(5): p. 1329-1337.

127. Ivanov, A.P., et al., *DNA Tunneling Detector Embedded in a Nanopore.* Nano Letters, 2011. **11**(1): p. 279-285.

128. Liang, X.G. and S.Y. Chou, *Nanogap detector inside nanofluidic channel for fast real-time label-free DNA analysis.* Nano Letters, 2008. **8**(5): p. 1472-1476.

129. Tsutsui, M., et al., *Transverse electric field dragging of DNA in a nanochannel.* Sci Rep, 2012. **2**: p. 394.

130. Steinbock, L.J., et al., *Probing DNA with micro- and nanocapillaries and optical tweezers.* Journal of Physics-Condensed Matter, 2010. **22**(45).

131. Cadinu, P., et al., *Double Barrel Nanopores as a New Tool for Controlling Single-Molecule Transport.* Nano Letters, 2018. **18**(4): p. 2738-2745.

132. Branton, D., et al., *The potential and challenges of nanopore sequencing.* Nature Biotechnology, 2008. **26**(10): p. 1146-1153.

133. Ivanov, A.R., et al., *High Precision Fabrication and Positioning of Nanoelectrodes in a Nanopore.* Acs Nano, 2014. **8**(2): p. 1940-1948.

134. Tsutsui, M., et al., *Single-molecule sensing electrode embedded in-plane nanopore.* Scientific Reports, 2011. **1**.

135. Nam, S.W., et al., *Ionic field effect transistors with sub-10 nm multiple nanopores.* Nano Lett, 2009. **9**(5): p. 2044-8.

136. Taniguchi, M., et al., *Fabrication of the gating nanopore device.* Applied Physics Letters, 2009. **95**(12).

137. Healy, K., et al., *Fabrication and characterization of nanopores with insulated transverse nanoelectrodes for DNA sensing in salt solution.* Electrophoresis, 2012. **33**(23): p. 3488-96.

138. Liang, X. and S.Y. Chou, *Nanogap detector inside nanofluidic channel for fast real-time label-free DNA analysis.* Nano Lett, 2008. **8**(5): p. 1472-6.

139. Sadar, J., Y. Wang, and Q. Qing, *Confined Electrochemical Deposition in Sub-15 nm Space for Preparing Nanogap Electrodes.* ECS Trans, 2017. **77**(7): p. 65-72.

140. Qing, Q., et al., *Finely tuning metallic nanogap size with electrodeposition by utilizing high-frequency impedance in feedback.* Angew Chem Int Ed Engl, 2005. **44**(47): p. 7771-5.

141. Smith, D.P.E., *Quantum Point-Contact Switches.* Science, 1995. **269**(5222): p. 371-373.

142. Chen, K., et al., *Direction- and Salt-Dependent Ionic Current Signatures for DNA Sensing with Asymmetric Nanopores.* Biophys J, 2017. **112**(4): p. 674-682.

APPENDIX A

CO-AUTHORS AGREEMENT ON USING PUBLISHED WORK

Part of Chapter 2 in this dissertation was published as “Controlling ERK Activation Dynamics in Mammary Epithelial Cells with Alternating Electric Fields through Microelectrodes.” in NanoLetters (Guo, L et al, 2019). All co-authors have granted their permission to use the published article in this dissertation.